SYNCHROTRON-BASED FE K-EDGE MICRO-XAS AND MICRO-XRF SPECTROSCOPY INVESTIGATION OF ZONED AQUAMARINE AND EMERALD CRYSTALS

By

Patrick F. Tomasic

May, 2024

Director of Thesis: Adriana Heimann Rios, PhD

Major Department: Geological Sciences

Although the generalities on the origin of the green color of beryl and emerald and the blue color of aquamarine are known, the role of Fe in causing and influencing them and the relationship between the relative Fe valence state and coordination geometry with intra-crystal color variations are highly unknown. Green and blue colors and their variations in beryl are variably attributed to combinations of Fe^{3+} and Fe^{2+} in octahedral, tetrahedral, channel, and/or 6g interstitial sites. Here, the first combined synchrotron-based Fe K-edge micro X-ray absorption spectroscopy (XAS) and micro-XRF spectroscopy study of a green color-zoned emerald crystal and a blue zoned aquamarine crystal is presented. Characteristic parameters of XAS pre-edge and extended X-ray absorption fine structure (EXAFS) were determined to identify possible relationships between the relative valence state and coordination environment of Fe, abundance chromophore elements, and intra-crystal color differences. High-resolution micro-XRF elemental mapping of the zoned emerald crystal evidences marked zoning in Fe and Cr contents in bands down to 0.05 mm thick parallel to {0001} and a strong positive correlation between them that decrease from the darker green bottom to the very light green upper zone. Higher Fe contents in the green color compared to the very light green zone darken the color generated by chromophore Cr and in less degree V. Fit centroid energy, integrated intensity, and peak ratios of two pre-edge peaks correlate with Fe intensity and color variation. Centroid energy and integrated intensity relations suggest the

occurrence of Fe^{2+} and Fe^{3+} mostly in octahedral coordination in both green color zones, with minor Fe^{3+} in the very light green zone likely located in a tetrahedral site. Increasing centroid, integrated intensity, and pre-edge P2/P1 ratios in the order darker green → very light green → red beryl suggest a higher average Fe valence state (Fe^{3+}/Fe_{Tot}) in the very light green than in the green area. EXAFS analysis shows dominance of octahedral Fe, shorter modeled Fe-O distances (avg. 1.94 Å) for the zoned emerald than the red beryl crystal (avg. 1.98 Å), and similar Fe-O bond lengths in the two green zones. Modeled Fe-Fe bond distances representing Fe pairs in Al-6g sites are slightly shorter for the green than the very light green zone. Detailed synchrotron micro-XRF chemical maps of the zoned aquamarine crystal reveal delicate (1 mm) zoning in Fe contents that match visible color changes from colorless to pale blue, medium blue, and darker blue. A strong correlation between darkening of the blue color and Fe intensity not seen for Cr, Mn, and V indicates that Fe is the main chromophore. Pre-edge fit centroid energy and integrated intensity indicate the presence of octahedral Fe^{2+} and Fe^{3+} in all color zones. Iron contents, centroid energy, integrated intensity, and peak height increase in the order colorless → light blue → medium blue → darker blue zones reflecting higher $Fe^{3+}/\sum Fe$ in the darker blue color zones. EXAFS modeling confirms mostly octahedral Fe and minor Fe pairs in octahedral and 6g interstitial sites in all color zones. The Fe-Fe bond distance (2.151 Å) is the longest in the clear zone, whereas the blue zones yield shorter Fe-Fe bond lengths (2.066-2.112 Å), consistent with closer Fe-Fe pairs generating and darkening the blue color by IVCT. This study provides a new quantitative way to distinguish light from darker green and blue colors in beryl using combined synchrotron micro-XRF and Fe-K pre-edge and EXAFS parameters. The relationships found between redox state and coordination environment of Fe and elemental abundances with color variations in emerald and aquamarine need to be verified for other crystals and applied to investigate other colors.

SYNCHROTRON-BASED FE K-EDGE MICRO-XAS AND MICRO-XRF SPECTROSCOPY INVESTIGATION OF ZONED AQUAMARINE AND EMERALD CRYSTALS

A Thesis

Presented to the Faculty of the Department of Geological Sciences

East Carolina University

In Partial Fulfillment of the Requirements for the Degree

Master of Science in Geology

By

Patrick Francis Tomasic

May, 2024

Director of Thesis: Adriana Heimann Rios, PhD
Thesis Committee Members:
Raquel Alonso Perez, PhD
Regina DeWitt, PhD
David Farris, PhD
Eric Horsman, PhD

DEDICATIONS

This thesis is dedicated to my parents, Chris and Marilyn, and my grandparents who have been my strongest support team from the very beginning. To also my brothers, Tyler, Robbie, and Wade, who have shown me how to persevere and adapt to life's many challenges. To my girlfriend, Ann Marie, for her unwavering support and love. Lastly to my cats, Momo, Marvin, and Marceline, who have kept me companionship during stressful times. Words truly cannot describe the gratitude and appreciation that I have for your love and support.

ACKNOWLEDGEMENTS

I am grateful for the support of various people who have helped me in recent years as I worked on my thesis. I would like to express my gratitude to the Department of Geological Sciences at East Carolina University for providing me with the incredible opportunity to complete my studies here. I would like to acknowledge Dr. Adriana Heimann Rios, my research advisor, for her patience, guidance, and understanding, without which I would not have achieved this great milestone. I am also thankful to Dr. Raquel Alonso Perez for providing the samples, serving on my committee, and supporting me throughout the process. Dr. Darby Dyar is thanked for her initial consultation and input for XANES/XAS analysis and for providing access to the DEVAS software. Dr Yuanming Pan is thanked for checking EXAFS data for control. I am grateful to Drs. Tony Lanzirotti and Matt Newville for providing training at the Advanced Photon Source Sector and for their support and guidance during experiments at the Advanced Photon Source and in part of the data analysis. In addition, I would like to thank Dr. Regina DeWitt, Dr. David Farris, and Dr. Eric Horsman for serving on my committee. This work was funded by a Research Initiation Grant from East Carolina University Harriot College of Arts and Sciences and the Department of Geological Sciences. Harvard Mineralogical and Geological Museum provided samples 86394, 97019.2, and 131716 on loan for this study. This research used resources of the Advanced Photon Source (APS), a U.S. Department of Energy (DOE) Office of Science User Facility operated for the DOE Office of Science by Argonne National Laboratory (ANL) under Contract No. DE-AC02-06CH11357. This work was performed at GeoSoilEnviroCARS (GSECARS), Sector 13 of the APS, The University of Chicago and ANL, IL, under User Proposal 75486.

TABLE OF CONTENTS

LIST OF TABLES

CHAPTER 1

CHAPTER 2

LIST OF FIGURES

CHAPTER 1

and the red beryl from Utah, USA. **b.** Centroid *vs.* Fe-Fe distance (Å) fitting for the zoned emerald crystal from Chivor, Colombia.

CHAPTER 2

Figure 1. Atomic structure of beryl looking down: **a.** the c axis of the basal plane and showing the 6-membered silicate rings forming channels. **b.** the b axis illustrating the 6g interstitial position between two octahedral Al sites along the c axis. Be (green) and Si (light tan) are shown in their tetrahedral site and Al (brown) in its octahedral coordination. Water (W) molecules (blue) and Na (purple) are shown in the channels. Images generated in Mindat.org.

Figure 2. Zoned aquamarine crystal used for the synchrotron-based Fe K-edge XAS and XRF study showing color zoning from right to left from clear to light blue, darker blue, and medium blue. Sample 86394, Minas Gerais, Brazil, Geological and Mineralogical Museum, Harvard University.

Figure 3. Sample stage setup with crystals oriented horizontally with their c axis at 45° to the direction of the incident X-ray beam. Advanced Photon Source synchrotron facility, Argonne National Lab, IL, where micro-XAS and XRF experiments were conducted.

Figure 4. Graph of normalized absorption μ(E) (arbitrary units) *vs.* Energy (eV) with background subtracted for the nine XAS analyses of the zoned aquamarine crystal showing: **a.** The full energy range of the raw data spectra with analyses offset for visualization. **b.** Zoomed in view of the pre-edge area of the normalized spectrum.

Figure 5. Graph of first derivative of the normalized absorption dμ(E)/dE (arbitrary units) *vs.* Energy (eV) for the Fe XAS analyses of the zoned aquamarine crystal showing the spectra of the XANES area at an energy range of 30 eV below the edge (E_0) and 30 eV above the edge. Note the major feature before the edge has two components (peaks) for all analyses, with the low energy peak considerably higher for the clear zone of the crystal (spot 1) compared to the darker blue zones (spots 2-10).

Figure 6. Graphs of normalized μ(E) with baseline subtracted *vs.* Energy (eV) for Fe K-edge XAS pre-edge analyses of the zoned aquamarine crystal deconvoluted by two Voigt components. Numbers shown correspond to spot analyses. P1 (Voigt1) and P2 (Voigt2) are the two pre-edge peaks observed in the spectrum.

Figure 7. Results of synchrotron micro-XRF spectroscopy of the zoned aquamarine crystal showing: **a.** Fe chemical map of studied area. **b.** X-slice of Fe intensity (counts) ***vs.*** distance (mm). **c.** Zoned Aquamarine crystal with 6 x 1 mm rectangle of studied area. **d.** Cr chemical map. **e.** V chemical map. **f.** Mn chemical map. The bars to the right represent the intensity scale from low (black, dark) to high (bright, light). Numbered spots within the crystal correspond to XAS analyses.

Figure 8. Binary plots showing the relationship between elemental intensities (counts) derived from micro-XRF chemical maps in the zoned aquamarine crystal. **a.** Fe *vs.* Cr intensity. **b.** Fe *vs.* Mn intensity. **c.** Fe *vs.* V intensity. The vertical lines separate the crystal's different blue color zones, which are defined by Fe intensity variations.

Figure 9. Binary plots of pre-edge fit parameters *vs.* Fe intensity. **a.** Fit Centroid *vs.* Fe Intensity. **b.** Pre-edge integrated intensity *vs.* Fe intensity. **c.** Integrated peak height *vs.* Fe intensity. Pre-edge peak parameters obtained by fitting all spots together. Energy unshifted to that of Wilke et al. (2001).

Figure 10. Representative FEFF fitting for Fe K-edge in R-space (Å) *vs.* the Fourier transform of the XAFS equation, $|\chi(R)|\left(\text{Å}^{-3}\right)$ for: **a.** Light blue/colorless zone in the zoned aquamarine crystal. **b.** Dark blue zone in the zoned aquamarine crystal. **c.** Red beryl crystal from the Wah Wah Mountains, Utah, sample 131716. **d.** Green zone of a zoned emerald crystal from Colombia, sample 97019.2. Numbers on the graph refer to peak numbers discussed in the text and reported in Table 2. Crystals from the Geological and Mineralogical Museum, Harvard University.

Figure 11. Pre-edge fit centroid (eV) position *vs.* integrated intensity for: **a.** Different color zones of the zoned aquamarine crystal from Minas Gerais, Brazil. **b.** Different color zones of the zoned aquamarine crystal and the red beryl crystal from Wah Wah Mountains, Utah. After Wilke et al. (2001). Inset shows the same graph with the end members of Wilke et al. (2001; not re-calibrated based on $E_{0;}$ energies not directly comparable).

Figure 12. Graphs of modeled Fe-O bond distance (1.94 Å) obtained by FEFF EXAFS fitting for the zoned aquamarine crystal *vs.*: **a.** Fit centroid (eV). **b.** Fe intensity. **c.** Integrated intensity.

Figure 13. Graphs of modeled Fe-Fe bond distance (Å) obtained by EXAFS fitting for the zoned aquamarine crystal *vs.*: **a.** Integrated intensity. **b.** Fe intensity. **c.** Fit centroid (eV).

LIST OF APPENDIX FIGURES

CHAPTER 1

CHAPTER 2

LIST OF APPENDIX TABLES

CHAPTER 2

CHAPTER 1: SYNCHROTRON FE K-EDGE MICRO-XAS (XANES AND EXAFS) AND MICRO-XRF SPECTROSCOPY REVEALS SUB-MM-SCALE VARIATIONS IN ELEMENTAL CONTENT, FE VALENCE STATE, AND COORDINATION GEOMETRY WITH GREEN COLOR DIFFERENCES IN A ZONED EMERALD CRYSTAL

ABSTRACT

Although the generalities of the origin of the green color in emeralds and green beryl have been revealed by spectroscopic techniques, the role of Fe in causing variations in the shade of green is little known. For emerald, its vivid green color is due primarily to small amounts of Cr^{3+} and/or V^{3+} ions substituting into the Al octahedral site and minor Fe ions. The green color of Fe-bearing light green beryl has been variably attributed to: a mixture of yellow resulting from ultra-violet charge transfer (UVCT) of O^{2-} to Fe^{3+} in the Al octahedral site and blue due to UVCT by Fe^{2+} in a channel; inter-valence charge transfer (IVCT) between octahedral Fe^{3+} and Fe^{2+} in an octahedral, tetrahedral, or channel site, and in combination with UVCT of octahedral Fe^{3+}, and located secondarily in a channel or interstitial site. However, details regarding the relation between relative Fe valence state and atomic environment with green color variations in beryl is highly unknown. In this study, combined synchrotron-based high-resolution Fe K-edge micro-X-ray absorption (XAS) and micro-XRF spectroscopy of a green color-zoned emerald crystal (Chivor, Colombia) was used, for the first time, to identify characteristic parameters of the pre-edge and extended X-ray absorption fine structure (EXAFS) areas and detailed X-ray elemental maps to determine possible relationships between relative valence state and coordination environment of Fe, abundance of Fe and other chromophore atoms (Cr, V), and differences in very light green and green zones within the crystal.

Results of synchrotron micro-XRF mapping show that the Fe and Cr contents are positively correlated, but although Fe contents are higher in all darker green spots than in the very light green zone, Cr contents in some darker green spots are only slightly higher. Vanadium contents overlap in all spots analyzed and are low. High-resolution micro-XRF mapping evidences zoning defined by changes in Fe and Cr contents corresponding with growth bands

down to 0.05 mm in width. Chemical variations reflect an abrupt compositional change in the source hydrothermal fluid at the two-color boundary from the green bottom transitioning to the very light green top, with further fluctuations associated with decreasing Fe and Cr contents and, to a lesser extent, Mn and V. The origin of the darker green color in the zoned emerald is due to higher Fe contents, compared to the very light green zone, that darken the color generated by chromophore Cr, and in less degree V.

Comparison of Fe K-edge pre-edge XAS spectral parameters of the zoned emerald with a red beryl, which is known to contain only $^{VI}Fe^{3+}$, shows lower fit centroid energy (avg. 7112.71 eV) and integrated intensity for the zoned emerald. Centroid energy and integrated intensity are the lowest in the green zone, intermediate in the very light green zone, and the highest in the red beryl (centroid energy avg. 7112.82 eV). Centroid energies and integrated intensity suggest the occurrence of Fe^{2+} and Fe^{3+} mostly in octahedral coordination in both color zones of the zoned emerald. A lower-energy (P1) pre-edge peak larger than the higher-energy (P2) peak results in P2/P1 (height and amplitude) ratios < 1 for both color zones that positively correlate with Fe intensity and centroid energy and are higher for the very light green zone. Increasing centroid, integrated intensity, and P2/P1 ratios in the order green → very light green → red beryl suggest a higher average Fe valence state (Fe^{3+}/Fe_{Tot}) in the very light green than in the green area reflecting oxidation of the evolving fluid during crystal growth. In the very light green zone, some Fe^{3+} could be in the tetrahedral site or in the channel, thus diminishing the darker green color compared to the earlier darker green part of the crystal.

EXAFS analysis shows that the zoned emerald crystal has shorter modeled Fe-O R-space distances (avg. 1.94 Å) compared to the red beryl crystal (avg. 1.98 Å), whereas Fe-O bond lengths are similar in the green and very light green zones. Shorter Fe-O distances in the zoned

emerald than in the red beryl reflect less distortion of the octahedra due to less Fe^{3+} in the former. Modeled Fe-Fe bond distances representing a small probability of Fe-Fe pairs substituting in Al-6g sites positively correlate with centroid energy and are overall slightly shorter for the green than the very light green zone, suggesting that they may be responsible for darkening the green color of beryl. Considering XAS pre-edge parameters, bond probabilities, and similar modeled Fe-O distances in the zoned emerald crystal whose average fall between those of octahedral Fe^{3+} and tetrahedral Fe^{2+} and Fe^{3+}, Fe occurs as Fe^{2+} and Fe^{3+} in dominantly octahedral coordination replacing Al, with likely additional Fe^{2+} and Fe^{3+} in tetrahedral coordination and/or channels.

These results provide a new quantitative way to distinguish light from darker green colors in beryl using combined synchrotron micro-XRF, Fe K-edge pre-edge, and EXAFS, which enable to identify relationships between relative oxidation state and coordination environment of Fe and elemental abundances with green color variations in beryl and emeralds that can be applied to investigate other colors.

INTRODUCTION

Beryl, a mineral with the ideal chemical formula $Be_3Al_2Si_6O_{18}$, is a relatively uncommon mineral primarily found in granitic pegmatites and hydrothermal veins in specific geological contexts (e.g., Barton & Young, 2002). Its atomic crystalline structure consists of layers of cyclic silicate (SiO^{4-}) rings (Si_6O_{18}) intertwined with twisted beryllium tetrahedral units (Be^{2+} or $[BeO_4]^{6-}$) and octahedral aluminum units (Al^{3+} or $[AlO_6]^{9-}$) (Fig. 1a; Brag & West, 1926; Gibbs et al., 1968; Morosin, 1972; Hazen et al., 1986; Artioli et al., 1993). These layers of silicate rings are systematically arranged along the c-axis, forming open channels capable of incorporating alkalis

like Na^{2+}, K^{+}, Cs^{+}, transition metal cations such as Fe^{2+} and Fe^{3+}, and large molecules including water (H_2O) and carbon dioxide (CO_2) (Wood & Nassau, 1968; Goldman et al., 1978; Viana et al., 2002; Andersson, 2006; Bunnag et al., 2020; Shang et al., 2022). Transition metal cations, particularly chromium (Cr) and iron (Fe), can be located within 6g interstitial sites (voids between two Al octahedral sites) and 4d interstitial sites (voids between Be tetrahedral sites) along the c axis, as well as substituting Al in octahedral coordination (Fig. 1b; Dvir & Low, 1960; Wood & Nassau 1968; Aurisicchio et al., 1988; Fritsch & Rossman 1988; Aurisicchio et al., 1994; Mathew et al., 2000; Viana et al., 2002; Lin et al., 2013; Shang et al., 2022). Iron has been demonstrated to occur as Fe^{2+} and Fe^{3+} ions in predominantly 6-fold coordinated sites within the mineral structure (Wood & Nassau, 1968; Goldman et al., 1978; Fritsch & Rossman, 1988; Mathew et al., 2000; Taran & Rossman, 2001; Spinolo et al., 2007; Groat et al., 2010; Lin et al., 2013; Andersson, 2019; Bunnag et al., 2020). Not only does the incorporation of Fe and other chromophores in beryl have significant implications for understanding the causes of color in the mineral, but it also indicates how the crystal formed in its specific geologic setting.

Gemstones, such as those that can form as beryl crystals, are natural inorganic minerals with physical features such as luster and color that add aesthetic value and have practical use in jewelry as ornamental pieces. Because of various elemental substitutions in its structure and coordination geometries of these elements, the color of beryl can vary considerably, resulting in semi-precious, gem-quality, often euhedral hexagonal crystals. Pure beryl, without elemental substitutions in its crystalline structure or those that do not produce color, is clear and colorless, and when it is also transparent and gem-quality, it is referred to as goshenite (Wood & Nassau, 1968; Mathew et al., 2000; Shang et al., 2022). The highest demand and commercial value among gem-quality beryl is for the green-colored variety, emerald, which are highly sought after

and traded worldwide in a multibillion-dollar market. The deeper the green color of the emerald, the rarer and more valuable it is. However, although the general aspects of the origin of the green color in emeralds are known, details regarding color variations in green beryl remain to be fully explained and investigated by spectroscopic means. Its green vivid color is due primarily to small amounts of Cr^{3+} and/or V^{3+} substituting into the octahedral Al site (Wood and Nassau, 1968; Fritsch & Rossman, 1988; Gaudry et al., 2007; Bai et al., 2019). The green color of Fe-bearing green beryl has been variably attributed to: a mixture of yellow resulting from ultra-violet charge transfer (UVCT) of O^{2-} to Fe^{3+} in the octahedral site and blue originated by UVCT by Fe^{2+} in a channel (Fritsch & Rossman, 1988; Viana et al., 2002); inter-valence charge transfer (IVCT) between octahedral Fe^{3+} and Fe^{2+} in an octahedral, tetrahedral, channel, or interstitial site, in combination with UVCT of octahedral Fe^{3+} or secondarily in a channel or interstitial site (Wood & Nassau, 1968; Mathew et al., 2000; Platonov et al., 2016). Red beryl, on the other hand, owes its color to octahedral Mn^{3+}, but it also contains trivalent iron in octahedral coordination substituting for Al (Wood & Nassau, 1968; Wood & Nassau 1968; Fridrichová et al., 2017; Andersson, 2019; Gatta et al., 2022). Some studies on color zoned emeralds reported concentrations and elemental maps obtained by traditional techniques (e.g., Curado et al., 2014; Hu and Lu, 2019; Cui et al., 2022). For example, studied emeralds from Davdar, China (Cui et al., 2022) and Malipo, China (Hu and Lu, 2019) reveal concentric color zoning accompanied by elemental variations in V and Cr, which were considered responsible for the green color. Curado et al. (2014) utilized synchrotron radiation to characterize emeralds from Brazil and distinguish elemental fingerprints among different mines. However, Fe and its valence state or coordination geometry were not studied in detail or related to color variations in these investigations.

Synchrotron radiation techniques have been successfully employed to investigate the atomic state of elements in some minerals and silicate glasses (e.g., Bajt et al., 1994; Wilke et al., 2001; Dyar et al., 2002a, 2016; Berry et al., 2003; Villain et al., 2007; Ingall et al., 2010; Evans et al., 2014; Feige et al., 2017; Rehman et al., 2020). In particular, synchrotron-based micro-X-ray absorption spectroscopy (XAS) is a well-established, non-destructive, and powerful analytical technique used extensively to understand the local atomic structure and oxidation state of transition metals, including specifically the determination of neighboring environments such as coordination numbers and bond distances of the studied element (Bajt et al., 1984; Westre et al., 1997; Wilke et al., 2001; Dyar et al., 2002; Lin et al., 2013; Bunnag et al., 2020). The K-edge X-ray absorption spectra of Fe can be divided into two regions: the X-ray absorption near-edge structure (XANES) and the extended X-ray absorption fine structure (EXAFS). The XANES region, known as the pre-edge, begins approximately 10 eV below the absorption edge and changes with the oxidation state of the absorbing atom (Penner-Hahn, 2003; Newville, 2004). Every first-row transition metal with an open 3d shell has a K-edge and a K-shell since they have 1s core electrons that can be excited by X-rays with energies in the range of 4088 to 9659 eV (K-shell) (Penner-Hahn, 2003). Pre-edge peaks' shapes, positions, and intensities are related to the oxidation state and coordination geometry, and specifically, the pre-edges and edges of minerals are shifted to higher energy as the $Fe^{3+}/\Sigma Fe$ ratio increases (e.g., Bajt et al., 1994; Berry et al., 2003; Newville, 2004).

The EXAFS (extended X-ray absorption fine-structure) region is located approximately 20-30 eV away from the absorption edge in a K-edge X-ray absorption spectrum. It is characterized by modulations that arise from the interference effects of scattered electron waves with neighboring atoms. Synchrotron X-rays, which can obtain the EXAFS spectrum with

tunable energy, are typically used to interpret the pattern, and provide a radial distribution function (Wenk & Bulakh, 2004). The curve produced by this function gives the probability of finding the nearest neighbor at a certain distance from the absorbing atom, and this distance in Å is derived from a theoretical EXAFS equation. This technique is often used to determine the coordination geometry of the absorbing atom and what elements may be substituted in the crystal structure. Furthermore, EXAFS spectroscopy can provide information on the local structure of elements, such as the coordination numbers, bond distances, and even structural distortions in the crystal lattice (Wenk & Bulakh, 2004). Overall, EXAFS spectroscopy is a powerful tool for investigating the local atomic environment of elements in materials science and is widely used in fields such as chemistry, physics, and geology.

Only two studies investigated Fe and the causes of color and color variation in green beryl using synchrotron-based Fe K-edge XAS spectroscopy, and none have studied color-zoning or green color variation in emeralds. Eeckhout et al. (2005) reported the first XAS study of Fe in two green (and yellow) beryl crystals from Brazil. Comparing the absorption edge of the XANES spectra of Fe with Fe^{2+} and Fe^{3+} reference samples they showed that the edge characteristics of beryl are a combination of those in the two reference samples, indicating the presence of both Fe^{2+} and Fe^{3+}. Pre-edge characteristics of beryl compared with the reference samples confirmed the presence of octahedrally coordinated Fe^{3+}, but could not confirm the presence of Fe^{2+} due to the small pre-edge features for octahedral Fe^{2+}. In a second study of 35 green beryl crystals from Madagascar by Chankhantha et al. (2016), Fe K-edge XAS coupled with ultraviolet-visible (UV-Vis) near-infrared (NIR) spectroscopy were used to determine the oxidation state of Fe. The cause of a light to medium green color was suggested to be the occurrence of octahedral V^{3+} or Fe^{3+}. So far, although it is known that iron tends to generally

darken mineral colors, the relationship between Fe, Cr, V, and Mn contents, the magnitude of characteristic synchrotron XAS parameters reflecting structural environments and relative valence state of Fe and green color variations in emerald crystals has not been investigated, but it can offer new quantitative information.

In this contribution, a thorough investigation was carried out on a color-zoned emerald crystal from Chivor, Colombia, exhibiting very light green and green zones. The goal was to uncover potential causal connections between intra-crystal color differences, elemental abundances of Fe, Cr, Mn, and V obtained through detailed synchrotron micro-XRF spectroscopy mapping analysis, and variations in Fe K-edge XANES pre-edge and EXAFS quantitative parameters used as proxies to determine the relative average oxidation state of Fe, coordination geometry, and bond distances to nearest neighbors. Further, comparisons are made with the same analysis of a red beryl crystal from Utah. Identified relationships between local atomic structure of Fe, elemental abundances, and green color differences in the zoned emerald crystal provide a new way of understanding the role that chromophore elements play in generating the green color in beryl as a defining property distinguishing gem-quality emerald. Because the study revealed insights into the distribution and arrangement of impurities of Fe, Cr, Mn, and V within beryl, this knowledge can prove instrumental in extracting the "critical mineral" Be from beryl. Furthermore, the findings on the atomic environment of Fe and elemental zoning in the zoned emerald from Colombia can be utilized to differentiating it from those from other sources, and can also prove helpful in the color treatment and enhancement processes of emeralds.

SAMPLING AND ANALYTICAL METHODS

Sample description, geologic setting, and emerald formation

In this study, we investigated a 6 mm long by 3 mm wide zoned emerald crystal (sample 97019.2) from Chivor, Colombia, housed in the Geological and Mineralogical Museum at Harvard University. The crystal is euhedral with a hexagonal prismatic habit and flat basal plane terminations. The crystal exhibits a color-zoned structure along the c axis characterized by two different zones perpendicular to its length: a very light green to clear zone on one end (2.5 mm thick) and a green zone on the other end (3.5 mm thick), with a sharp transition between the two zones in the center of the crystal. The green zone of the crystal has some localized mineral coverings on the base. In addition, very thin (size 0.001 mm) green planar growth bands are observed in the very light green to colorless color zone. From here on, the very light green to colorless zone will be referred to as very light green. The overall shade of green of sample 97019.2 is a lighter shade of green than other emerald samples from Chivor, Colombia.

The zoned emerald crystal is derived from the Chivor municipality in the Guavió-Guatéque mining district of the Boyacá department in Colombia. Emeralds in this region are hosted in a sedimentary sequence of sandstone, limestone, black shale, and evaporite (Cheilletz & Giuliani, 1996; Groat et al., 2005). According to various studies, emeralds from Colombia are formed by hydrothermal brines and sulfate reduction in combination with organic-rich Cretaceous black shales (e.g., Cheilletz & Giuliani, 1996; Giuliani et al., 2005; Groat et al., 2008; Rondeau et al., 2008; Fortaleche et al., 2017). These studies suggest that the environment of formation for emeralds represents low-grade metamorphism at a temperature range of 290-360 °C and a pressure of 100 bars (Ottaway et al., 1994). Additionally, age dating by muscovite

$^{40}Ar/^{39}Ar$ used to determine the age of the emerald deposit in Chivor yield a formation age of 61-65 Ma (Zimmermann et al., 1997; Branquet et al., 1999; Nicklas et al., 2022).

In more detail, Branquet et al. (1999) proposed a refined model for emerald genesis based on studies of Colombian sediment-hosted deposits. The authors concluded that the deposits formed from the interaction of evaporitic brines and organic-rich black shale, as also described in Ottaway et al. (1994) and Giuliani et al. (2000). During the thermal reduction process, sulfate reacts with brine at temperatures ranging from 300-330 °C. This process occurs in the presence of organic matter in the black shale, leading to albitization. As a result, pyrite (FeS_2) and Be-bearing mineralization are formed, creating emeralds that have low Fe content but rich in V and Cr (Ottaway et al., 1994). Furthermore, despite the sedimentary origin of the deposits, Copper et al. (1995) proposed that the Colombian emerald deposits were ultimately related to subduction and orogeny, with the formation of a sedimentary back-arc basin and the sourcing of sediments from the Jurassic and Cretaceous Andean Arc.

The Chivor deposit boasts a variety of mineralized structures, including centimeter- to decameter-scale listric faults, meter-wide extensional fractures injected with hydrothermal breccia that form chimneys, and a well-developed set of extensional fractures mainly filled with carbonate and pyrite (Branquet et al., 1999). These mineralized structures formed simultaneously with hydrothermal fluid circulation and emerald deposition. In addition, the structures are extensional and point to a relative movement of the hanging wall of the brecciated level, which moved only slightly towards the southeast and was a normal downdip slip on the brecciated level, which functioned as a local detachment. The deformation during mineralization corresponds to a thin-skinned, limited-extent extensional tectonic event at the time of the

Cretaceous-Tertiary boundary, influenced by evaporite dissolution and gravity-driven movement (Branquet et al., 1999).

A red beryl crystal from the Wah Wah Mountains in Utah housed in the Geological and Mineralogical Museum at Harvard University (sample #131716) was used for comparison with the zoned emerald crystal. The red beryl represents a very rare geological occurrence. Red beryl originated along fractures in a topaz rhyolite as a vapor-phase mineral resulting from a chemical reaction between magma-derived gases, groundwater, and preexisting minerals and volcanic glass (Shigley et al., 2003). The only known source of quality red beryl in the world is the Ruby Violet mine situated in the Wah Wah Mountains.

Synchrotron micro-XAS and micro-XRF analysis

Synchrotron-based XAS and micro-XRF analyses were conducted at the Advanced Photon Source (APS), Argonne National Laboratory, IL, using beamline 13-ID-E, chosen for its high X-ray brilliance and spatial resolution (Fig. 2). The emerald crystal was placed on a sample holder with its c axis oriented horizontally and at a 45° angle from the direction of the incident X-ray beam (Fig. 3). The red beryl was visually oriented in the same direction. The XAS analyses were recorded in fluorescence mode, with the crystal probed for Fe at the K edge (7112 eV), as well as for Cr. A Si (111) monochromator was used under an undulator-based (high flux) beamline of 2 μm in size, and silicon mirror stripes were used to obtain an appropriate energy resolution.

Micro-XRF data were collected from the emerald crystal at the same beamline using a Canberra SXD-7 XRF detector with an experimental distance of 81 mm. The X-ray energy used

to generate XRF elemental maps was set to 10 keV, with an X-ray intensity (I0) flux of 8.83959×10^{11} Hz and incident and exit angles of 45 degrees relative to the c axis of the crystal. The crystal was positioned 50 mm away from the detector, which had a detector area of 50 mm^2 used to create the map. A set of points located near the crystal center were chosen for XRF elemental mapping using a FLIR optical microscope capable of zooming to the micrometer scale. The XY coordinate system of the *GSE MapViewer* program (Newville, 2013) was used to input the position of the selected points. Within the zoned emerald crystal, spots were selected for XAS analysis to obtain the Fe Kα XAS spectrum in fluorescence mode based on specific zones within the crystal visualized in detailed micro-XRF elemental maps of individual elements and combined. XANES mapping was recorded across the sample by collecting the Fe K-edge signal on the green and very light green zones.

For XAS analysis of spots within the zoned emerald crystal at X-ray energies for a particular element, the Epics Scans script was coded to move the energy of the X-ray beam to match the binding-core energy of the innermost electron shell (i.e., “move_to_Fe(), move_to_Cr(), or move_to_Mn()”, where () refers to the coding input into the program to move the energy of the X-ray to the binding core energy of the particular element. To perform the XAS scan, the Epics Scans script was programmed to specify the crystal position and the number of scans to be performed for the selected element. This was done by coding the script as "pos_scan('97019_spot4), 'Fe_XANES', number=1", where "pos_scan('97019_spot4)" denotes the position of the sample using XY coordinates, "Fe_XANES" is the chosen element and spectroscopy technique, and "number=1" indicates the number of scans to be performed at that spot. After collecting the absorption energy, μ(E), data, the analysis was performed with the assistance of the XAS Viewer software program (Newville, 2013). X-ray Larch software was

used to perform normalization, pre-edge peak fitting, and FEFF analysis (Newville, 2013). The spectra of the seven spot analyses were examined both individually and as a group.

The Epics Scans script (Newville, 2013) was used to obtain XRF maps for all elements at an optimal energy range for elemental intensities within the samples by executing "move_to_mapkev()". The chemical maps were generated and viewed using the GSE XRM MapViewer application in the X-ray Larch XAS analysis package (Newville, 2013). To create the XRF map, a center point was selected using an optical microscope. The size of the map was set to 4 mm long parallel to the crystal's c axis, and 1 mm wide perpendicular to the crystal's c axis, which was mounted on the sample stage. A total of 1201 and 201 pixels were recorded parallel and perpendicular to the crystal's c-axis, respectively. For each direction, the scanning step was set to 0.0050 mm, and the dwell time per pixel was 10.0 ms. After generating the XRF map, seven spots were selected for XAS analysis based on the intensity of their Fe kα region of interest (ROI) using the multi-channel analyzer sum (mcasum) detector and the scalars normalization with I0 (incident X-ray intensity). These spots were selected at a single pixel within the GSE Map Viewer application. The location of seven spots within the crystal was recorded to later obtain XAS data. Among the seven spots analyzed, three were located in the high Fe intensity zone, whereas the remaining four were from the lower Fe intensity zone. The Fe XAS spectra of the seven spot analyses were examined individually and as a group. For Cr, only one pre-edge peak was visualized in the spectra of all spots analyzed within the zoned emerald crystal, and the results were not explored further for this study.

TREATMENT OF XAS FE AND CR K-EDGE DATA

XAS full spectrum data normalization and fitting

The raw Fe XAS spectra were processed using a background subtraction technique to analyze the seven spot analyses (Fig. 3a). To achieve this, the pre-edge region from 7050 to 7090 eV was fitted using a Victoreen order of 0, and the resulting curve was subtracted from the absorption spectrum. The methodology described by Wilke et al. (2001) was followed for the background subtraction. Next, the spectra were normalized for atomic absorption using the average absorption coefficient of the spectral region from 150 eV to 300 eV above the edge, as per the method suggested by Giuli et al. (2002) (Fig. 3b). A constant polynomial type was used for all XAS analyses for polynomial normalization. The spectra were energy calibrated using Fe foil as a reference, and the position of the first inflection point was determined to be at 7110.913 eV. For Cr, the XAS spectra were processed similarly to that of the Fe XAS analysis. The pre-edge background was subtracted by employing a Victoreen order of 0, with the resulting curve subtracted from the absorption spectrum. Polynomial normalization of all Cr XAS analysis was undertaken using a constant polynomial type. The spectra were energy calibrated using a Cr foil as a reference, and the position of the first inflection point was determined to be 5988.51 eV.

XAS Fe K-edge pre-edge fitting

Smoothing of the (pre-edge) spectra was done before fitting the pre-edge peaks to a model using the program *XAS Viewer*. To enhance the accuracy of the analysis, each data point was subjected to a smoothing process using the Savitzky-Golay method. This method employs a convolution form with Lorentzian distribution to remove noise and fluctuations in the data, resulting in a smoother curve that better represents the underlying trend. This approach is

particularly useful when dealing with noisy or erratic data sets, as it can help to uncover meaningful patterns and relationships that might otherwise be obscured.

The Fe K-edge pre-edge peaks of the zoned emerald crystal were modeled using a baseline model fitted to the pre-edge region to extract the pre-edge features of each XAS spectrum. This analysis method is similar to the one described by Wilke et al. (2001). To obtain the fitted deconvoluted peaks in *XAS Viewer*, a prompt allows one to select the baseline skip range, and the two endpoints to the low and high energy side of the visible center of each peak are selected by clicking on each point. The fitting process involved fitting and deconvolution of the peaks by a model using different energy windows and baseline skip ranges in multiple iterations to obtain the best fit, including observing the residual of each fitting and selecting the one with the lowest residual. Fitting also ensured only features representing the 1s --> 3d electron transition were included in the energy range fitting (Fig. 3). Additional small features were observed at the low energy side of the first clear pre-edge peak, at energies of ~ 7110 eV. Because this feature has been considered to represent an electronic transition different than the 1s --> 3d transition, it was not included in the energy range selected for pre-edge peak analysis (Bajt et al., 1994; Wilke et al., 2001; Berry et al., 2003). Similarly, additional features on the high energy side of the energy selected for the study were not included because they have been assigned to a different electron transition or process (Wilke et al., 2001).

Small variations in the baseline skip ranges yielded differences in centroid position energy and integrated intensity. This analysis highlights the sensitivity of XAS data analysis, where the selected energy fit range and baseline skip range can significantly impact the fitting results and the parameters obtained, and this is explored in the discussion. Two specific pre-edge fitting models were determined to produce the most accurate results (i.e., yield the lowest

residuals): fit energy ranges of 7109.5 to 7115.8 eV and 7109.0 to 7116.0 eV and using linear and Lorentzian baseline skip ranges of 7110.0 to 7115.2 eV and 7110.2 to 7115.2 eV. The fitting model selected used a fit energy range of 7109.5 to 7115.8 eV and a baseline skip range of 7110.0 to 7115.2 eV, and this fit was used to obtain and calculate pre-edge parameters.

The resulting pre-edge peaks were deconvoluted using a Voigt distribution function into two component peaks named P1 and P2 and the parameters of each peak, including normalized height, amplitude (area), center position energy (eV), and full-width half-maximum (FWHM), in addition to sigma (σ), and gamma (γ), were obtained using the XAS Viewer program (Table 2). The pre-edge information was then averaged for the pre-edge for each of the seven Fe XAS spot analyses by calculating the fit centroid, integrated intensity, and peak height. The pre-edge fit centroid is an area-weighted average of the energy positions of the peak components, calculated by adding each pre-edge component area multiplied by its center energy position and dividing by the sum of the areas [(P1 center * P1 area) + (P2 center * P2 area)] / (P1 area + P2 area). The integrated intensity is calculated by adding the area of each pre-edge component peak (P1 area + P2 area). In contrast, the integrated peak height is calculated by adding the heights of the pre-edge peak components (P1 h + P2 h).

Fe EXAFS data FEFF fitting

To analyze the EXAFS region of the full XAS spectrum collected from the zoned emerald crystal, the XAS Viewer program heavily relies on theoretical EXAFS spectra generated using FEFF software (Newville, 2013). The first step in this process was to choose a crystallographic information file (CIF) containing the known bond distances for beryl with Fe located at the octahedral site, replacing Al. Theoretical calculations were performed to determine the scattering

amplitude and phase shifts of Fe in different coordination sites. The results were then stored, including the scattering factors and mean-free path for each coordination site. After obtaining the theoretical scattering factors, the program refined the structural parameters using the EXAFS data from the zoned emerald. The EXAFS equation was used to derive the functions f(k), δ(k) and λ(k), which were then utilized to predict and adjust the structural parameters R (distance to the nearest neighbor, measured in Å), N (coordination number), and σ^2 (sigma square, mean square relative displacement). To best fit the χ(k) of the data, the absorption threshold E_0 was allowed to change. The average coordination number and distance were obtained by fitting the radial structure function χ using the Fourier transform of the experimental data.

EXAFS analysis of the zoned emerald was performed in R-space because it selectively ignores higher coordination shells. Therefore, when analyzing the data using R-space, the entire complex EXAFS χ(R), not just the magnitude |χ(R)|, was used (Newville, 2004). The CIF structure used to fit the zoned emerald was derived from a structure of beryl by Groat et al. (2010) for blue beryl from the True Blue showing, Yukon Territory, Canada, in which they identified the presence of Fe in an octahedral position. This structure was partly selected due to software limitations, as some CIF structures were either unavailable or did not contain Fe in the CIF structure.

RESULTS

Synchrotron micro-XRF elemental mapping and intra-crystal variations

Continuous micro-XRF spectra were gathered from the zoned emerald crystal exhibiting two main color zones to assess its overall chemical composition. Further, μ-XRF elemental

mapping was obtained on a 4 mm x 1 mm area of the crystal's zoned part, particularly on the section where a very light green zone and green zone meet (Fig. 5a). Micro-XRF elemental maps revealed Fe intensity variations perpendicular to the crystal's c axis (Fig. 5 b-e). In the low Fe intensity portion of the Fe XRF chemical map, a low Fe intensity zone (2 mm wide) is observed within the very light green zone of the crystal, where XAS spot analyses 7, 8, 9, and 10 were chosen (Fig. 5b). The XRF Fe chemical map of the crystal shows a distinct change into a different region (0.05 mm wide) marked by a sharp increase in Fe intensity where the color changes to the green zone, where spot analyses 4, 5, and 6 were selected for XAS analysis. Visually, in the Fe and Cr maps, Fe and Cr intensity variations generally coincide and correlate with the two main color zones and smaller-scale zoning planes within the zoned emerald crystal (Fig. 5 b,c). In contrast, the V and Mn XRF maps display less intensity distribution variability than the Fe and Cr chemical maps, and particularly V has very small compositional variation (Fig. 5 d,e). The V and Mn XRF maps reveal an absence and weaker, respectively, abrupt change in intensity where the color transition occurs within the crystal. The V and Mn maps mostly evidence variation only within the very light green portion of the zoned emerald.

Synchrotron-based micro-XRF chemical maps of the zoned emerald crystal revealed further, fine-scale zoning in Fe, Cr, V, and Mn intensity. These bands exhibit internal zoning as narrow as 0.05 mm in width, a level of detail that has not been observed before. The micro-zoning of Fe and Cr corresponds to variations in visible color from green to very light green from left to right in the chemical maps or from bottom to top. Additionally, a correlation was observed between the darkening of the green color and increasing Fe and Cr contents, as expected. These findings suggest that synchrotron chemical maps can provide valuable insights into emeralds' composition, color, and characteristics.

Further analysis using cross-sections of elemental intensity *vs.* distance within the crystal derived from Fe and Cr XRF chemical maps substantiate the visual observations and evidence an abrupt variation in elemental abundance throughout the zoned emerald (Fig. 5f, g). In both cross-sections, a decrease in the elemental intensities of Fe and Cr can be observed correlated with color zonation of the crystal from green to very light green from top to bottom (left to right) of the crystal. Further, a highly significant positive correlation exists between the color within the emerald crystal and Fe and Cr intensity, with Fe and Cr being higher in the green part than in the very light green zone (Fig. 6a; $R^2 = 0.8408$). This suggests that the color of emerald is strongly influenced by the intensity of Fe and Cr, implying that the presence and amount of these substituting elements contribute to its distinct coloration. In addition, V and Mn contents are an order of magnitude lower than Fe and Cr contents, V contents do not correlate with Fe contents, but Mn contents are positively correlated with Fe contents (Fig. 6 b,c). Based on available publications to date, no study has reported XRF elemental abundance maps for an emerald crystal with the level of resolution (0.05 mm) presented here obtained by synchrotron analysis.

General characteristics of micro-XAS Fe K-edge spectra of the zoned emerald

The full Fe K-edge XANES spectra for the seven spots from the zoned emerald crystal from Chivor, Colombia, analyzed for XAS are shown in Figure 3. Differences in the intensity of the absorption edge in the Fe XAS raw μ(E) spectra were observed for different spots, with the absorption edge of the very light green spot analyses having a lower raw μ(E) intensity than the spot analyses located in the green zone of the crystal (Fig. 3a). The normalized μ(E) Fe K-edge XAS spectra show no large visually observable differences in the absorption edge between the seven spot analyses within the zoned emerald crystal (Fig. 3b). However, analysis of the XANES

pre-edge region in the normalized μ(E) spectra confirm slight variations in the energy position of the two observable peaks among different spots. Pre-edge peak fitting analysis shows that although the deconvoluted spectra are similar, slight variations in the normalized μ(E) - baseline intensity and the width of the pre-edge peaks in the baseline subtracted spectrum exist among different spot analyses (Fig. 3b).

Characteristics of XAS Fe K-edge pre-edge peak parameters

Characteristics of Fe K-edge pre-edge peak spectral features are reported in Table 2, including the values for peak center position energy for the two peaks, fit centroid position energy, peak area, peak height, and integrated intensity for the spots within the green and very light green zones and sub-zones visible on XRF elemental maps. The unsmoothed Fe pre-edge fitted and deconvoluted spectra and their best fit, along with their residuals, obtained using XAS Viewer are shown in Figure 4, whereas the pre-edge spectra fitted with prior smoothing of the data are included in the Appendix (Fig. A2). Analysis of results from pre-edge deconvolution revealed variations in the centroid position energy for the two peaks among different spots within the zoned emerald crystal. At lower energy, the center energy of the first pre-edge peak ranges from 7112.4853 eV in a green spot to 7112.5380 eV in a very light green spot. At higher energy, the center energy of the second pre-edge peak ranges from 7114.0069 eV to 7114.1711 eV, both in very light green spots. In general, peak 1 has a center energy at ~7112 eV, whereas peak 2 has a center energy at ~7114 eV, consistent with previous Fe K-edge studies of beryl and other minerals and glasses (Wilke et al., 2001; Berry et al., 2003; Bunnag et al., 2020). The lowest centroid position was measured at 7112.6499 eV in a green spot, whereas the highest was found at 7112.7727 eV in a very light green spot.

Differences in the amplitude (area) of the individual pre-edge peaks cannot be visually distinguished among the various analyses from spectral observations alone. However, in all the analyses, both visual observations and quantitative analysis show that the first pre-edge peak located at lower energy has a larger amplitude than the second pre-edge peak at a higher energy center position (Figs. 3, 4; Table 2). For example, the amplitude of the first pre-edge peak ranges from 0.0383 in a green spot to 0.0431 in a very light green spot analysis. In contrast, for the second pre-edge peak, the amplitude ranges from 0.0041 in a green spot to 0.0091 in a very light green spot. In addition, the height of the two pre-edge peaks at lower and higher energy, respectively, recorded in normalized intensity (a.u.), varies. The intensities of the first pre-edge peak range from 0.01831 in a green spot to 0.0195 in a very light green spot analysis. At higher energy, the intensities of the second pre-edge peak range from 0.0034 in a green spot to 0.0050 in a very light green spot. Data show that the amplitude and intensity (height) of the pre-edge peaks differ within the zoned emerald crystal between the very light green and green zones.

Relations between Fe intensity, pre-edge centroid, integrated intensity, and color variation

Iron intensity obtained by micro-XRF in the seven spots analyzed in the two color zones of the emerald crystal plotted against pre-edge fit centroid energy shows a weak negative correlation (Fig. 7a; $R^2 = 0.3286$). However, the pre-edge fit centroid energy is clearly lower for the green spot analyses than for the very light green spot analyses. The spots within the very light green zone are characterized by a higher energy pre-edge fit centroid, ranging from 7112.7174 to 7112.7727 eV, and lower Fe intensity than the green spots. On the other hand, three green spots have higher Fe intensity and a lower energy pre-edge fit centroid ranging from 7112.6499 to 7112.7046 eV. A low but noticeable negative correlation is also observed between pre-edge

integrated intensity, Fe intensity, and color within the zoned emerald crystal (Fig. 7b; R^2 = 0.363). The integrated intensity is higher in the very light green spots, which have lower Fe intensity, than in the green spots, which have a higher Fe intensity. This suggests that Fe intensity is correlated with Fe's coordination environment represented by the integrated intensity (Wilke et al., 2001) and the color of the zoned emerald. Analysis of the zoned emerald shows that the Fe K-edge pre-edge peak centroid and integrated intensity are significantly higher in the very light green spots compared to the green spot analyses (Figs. 7a, b; Table 2). Overall, the correlation between the Fe pre-edge peak parameters and Fe content for the spots analyzed is distinct, and clear differences exist between the two color zones.

EXAFS FEFF R-space fitting

The Fe K-edge EXAFS data of the zoned emerald crystal analyzed modeled using FEFF8 in the software program XAS Viewer show four R-space peaks in the graph of R (Å) *vs.* $|\chi(R)|(A^{-3})$ (Fig. 8; Newville, 2013). The model was created with Fe substituting for Al^{3+} in the octahedral site, with the first shell scattering paths from the six nearest neighbor oxygen atoms having identical Fe-O distances and the second nearest neighbor paths from six silicon atoms also having the exact Fe-Si lengths (Lin et al., 2013). Four major peaks are present in all spots analyzed in the graph of R (Å) *vs.* $|\chi(R)|(A^{-3})$ (Fig. 8; Table 3). The R distances for the four peaks were derived from a FEFF model using a CIF structure from Groat et al. (2010) with reference distances for the Fe-O path of 1.9416 Å (peak 1), the Fe-Fe path equal to 2.300 Å (peak 2), the Fe-Si path of 3.2979 Å (peak 3), and the Fe-O path at a further distance of 3.7836 Å (peak 4). Despite multiple attempts, the fourth peak observed in the EXAFS R-space fitting at a further distance could not be modeled using the available FEFF paths. The resolution to obtain

information beyond the first three peaks observed in R-space was not enough given the analytical conditions used to obtain the current dataset.

Variations exist in the EXAFS parameters obtained for bond lengths indicative of distances to the nearest neighboring atoms between different color spots (Table 3). A model with an Fe-O path with six neighboring oxygen atoms was used to analyze these variations to determine the R-value distance for peak 1. Fitting results show that the R-value distance for peak 1 varies slightly between spot analyses, ranging from 1.929 Å to 1.948 Å, both in a very light green spot analysis. The R-value for peak 2 was modeled using an octahedral Fe atom and an Fe atom located in the 6g interstitial position aligned along the c axis at ~ 2.300 Å (Fe-Fe path). The modeled R-values for the Fe- Fe path also vary between spot analyses from 2.054 Å in a green spot to 2.072 Å in a very light green spot. The R-value for peak 3 was modeled using octahedral Fe and its nearest Si atom (parallel to the c axis), with the Fe-Si path varying between spot analyses from 3.286 Å in a green spot to 3.307 Å in a very light green spot. The fourth peak, located as a shoulder feature along the Fe-Si peak, was not fit due to insufficient energy range.

DISCUSSION

The synchrotron XAS and XRF spectroscopy data obtained in this study were utilized to investigate potential variations in the valence state and local environment of Fe atoms, and Fe, Cr, Mn, and V intensity related to color variations within the zoned emerald crystal. Previous research has shown that the spectral characteristics observed in the pre-edge region correspond to the electronic transition from 1s to 3d orbitals, from which the average oxidation state and coordination geometry can be inferred (Bajt et al., 1994; Berry et al., 2003). Several studies have

shown a connection between XAS spectra parameters pre-edge fit centroid and integrated intensity and the $Fe^{3+}/\Sigma Fe$ ratio in silicate glasses and other minerals (Berry et al., 2003; Dyar et al., 2016). Additionally, some research has been carried out to find out the relative oxidation state (i.e., $Fe^{3+}/\Sigma Fe$) of other minerals by using their pre-edge peak centroid and integrated intensity and comparing them with standards that have a known oxidation state and coordination geometry (e.g., Bajt et al., 1994; Wilke et al., 2001). The following discussion explores the observed relationships between color variations, Fe, Cr, Mn, and V intensity, XAS and EXAFS parameters, and their potential significance for the origin of the green color and variations in beryl and emerald.

Very-fine scale micro-XRF Fe, Cr, V, and Mn zoning relation to green color zoning

Although the present study is the first investigation reporting synchrotron XRF chemical maps of beryl, and specifically emerald, the synchrotron XRF study of emerald from Brazilian mines in the Goiás, Minas Gerais, and Tocantins states by Curado et al. (2014) was the first to chemically characterize the elemental fingerprint of (forty-seven) emeralds. They showed the reliability and utility of synchrotron radiation micro-XRF analysis for distinguishing some chemical characteristics of emeralds from different localities and colors ranging from light to dark green using element content histograms, principal component analysis, and ternary plotting. The study did not focus on the influence of Fe or other elemental content on color variation, used a lower beam resolution (0.5 mm beam), and did not present elemental maps. The present study reports the first evidence of high-resolution variations in Fe, Cr, and V abundance that correlate with green color differences in a zoned emerald crystal obtained by synchrotron XRF mapping (Fig. 5).

Ratios of Cr/V calculated from Cr and V elemental intensities obtained by synchrotron XRF for the zoned emerald crystal were compared to those for other emeralds available from previous studies in order to identify the type of beryl and chemical compositional relations with the two color zones (Table 1; Bosshart, 1991). Overall, Cr/V ratios for the zoned emerald are higher than 1 (3.3-6.8), classifying the emeralds as beryl-type I in Bosshart (1991) scheme, reflecting a higher Cr than V content. The highest Cr/V ratio (6.8) is observed in a green spot, whereas the lowest ratio (3.3) corresponds to a very light green spot. These Cr/V ratios are much higher than those for the (6) high-V emeralds from the Malipo deposit, Yunnan, China, reported by Bai et al. (2019) that have significantly higher contents of V^{3+} than Cr^{3+} and Cr/V values < 1. Therefore, the Chivor, Colombia, emerald can be regarded to as a type-I beryl and a Cr emerald.

Synchrotron-based micro-XRF chemical maps of the zoned emerald show fine-scale zoning in Fe, Cr, V, and Mn intensity seen as bands perpendicular to the c axis down to 0.1 mm in width that exhibit internal zoning smaller than 0.05 mm (Fig. 5). For example, a high Cr intensity band ~0.1 mm thick can be seen between spots 9 and 10 corresponding to a green band within the very light green zone of the crystal. Micro-zoning of Fe and Cr seen in the chemical maps and cross sections correlates with variations in visible color from green to very light green from one end to the other end of the area analyzed within the crystal. Further, based on the chemical maps and binary plotting, a correlation exists between the darkening of the green color with increasing Fe and Cr content (Figs. 5, 6). Among the four chromophore elements, Fe intensity strongly marks the boundary between the green and very light green zones in the crystal, whereas Cr has lower overall intensity and a less marked contrast between the zones. At ~ 0.6 mm from the center of the area analyzed into the very light green zone, a spike in Cr content coincides with the occurrence of a micrometric green growth band within the very light

green zone, whereas V and Fe contents are lower in this area (Fig. 5). This suggests that the presence of Cr atoms plays a critical role in generating the green color of this emerald. Yet, the very strong difference in Fe intensity at the color boundary suggests that the presence of Fe also strongly contributes to the critical darkening of the green color that generates the emerald-green color or lightening of the color to a very light green color.

The observation that the very light green spots have the lowest Fe contents and the green spot analyses have the highest Fe contents within the zoned emerald crystal agrees with recent results on blueish-green beryl by Shang et al. (2022). In their study of colored Fe-bearing beryl varieties, Shang et al. (2022) compared Fe contents obtained by energy-dispersive XRF spectroscopy and electron microprobe analysis with five colors and found that green beryl has lower Fe contents than beryl of other colors, and based on extrapolation of Fe data, it can be seen that Fe contents are lower in pale green beryl than in darker green beryl. Therefore, the results of the present study are consistent with those of Shang et al. (2022) that show that higher Fe contents darken the green color of beryl.

A relationship between the content of chromophores Cr and V and color within the zoned emerald crystal can be seen in the XRF elemental maps that show a marked contrast between the green zone with a Cr content higher than V, and the very light green zone with a Cr content lower than V, with V being more homogeneous in both zones. The lightest green growth bands have the lowest Fe, Cr, V, and even Mn contents. Color-element intensity relationships showing that in the green color zone of the emerald Cr contents are the highest, followed by Fe, with V also present, and that the very light green zone has the lowest Fe and Cr contents, but V is also present and more homogeneous, suggest that the green color is due to the presence and content of Cr and that higher Fe content makes it darker. Vanadium being more homogeneously present

in both color zones suggests that its presence may also play a role in generating a green color along with Cr, but V content variations do not seem to have a strong effect on green color variations (Fig. 6b). The darkening of the green color by higher Fe contents in the zoned emerald is consistent with previous studies that showed that the presence of Fe can modify the green color generated by other chromophores (Wood & Nassau, 1968), in this case this being Cr, and in less degree V. Similarly, the green color of the emeralds from Malipo was considered to be caused by Cr, V, and Fe^{3+} (and Fe^{2+}) identified by IR spectroscopy and EMP analysis, consistent with the results of this study. Because for Fe not only its concentration but its overall valence state within the crystal may influence the green color, this relationship will be evaluated further in the following sections that deal with the relationship between XAS parameters and color.

Results from the synchrotron micro-XRF chemical maps are consistent with results from previous studies that identified that variations in Cr, V, and Fe contents in emeralds generally affect color (Wood & Nassau, 1968; Fritsch & Rossman, 1988; Mathew et al., 2000; Andersson, 2019; Hu & Lu, 2020; Table 6). The presence of small quantities of V and Mn in the emerald crystal may also contribute to its coloration, and their detailed maps mostly evidence variation only within the very light green portion of the zoned emerald, which has not been shown before. Overall, the XRF maps provide detailed microscopic insights into the color zoning of the emerald crystal and its chemical composition that cannot be captured by conventional analytical techniques, also providing valuable information on the mineral's geological history and formation.

Significance of zoning for emerald genesis and fluid evolution

Based on the color zoning from the base to the top (left to right in Fig. 5) of the zoned emerald crystal that correlates with elemental variations, a decrease in Fe, Cr, V, and Mn was recorded during crystal growth. This chemical variability is visualized by color changes within the crystal in which the first half of the crystal with green color crystalized from a hydrothermal fluid high in Fe, Cr, and V, whereas the second part of the crystal with a very light green color grew with lower Fe, Cr, and V contents. Recorded chemical variations reflect a major compositional change in the source hydrothermal fluid at the two-color boundary from green to very light green. After the major change, further compositional changes in the hydrothermal fluid are seen in the crystal by the delicate very fine-scale color zoning throughout the very light green color zone of the crystal towards its top end. Therefore, these compositional variations reflect an initial hydrothermal fluid of homogeneous chemical composition during the growth of the first ~1.5 mm green color zone of the emerald, followed by an abrupt fluid change seen in a distinct color change that started the growth of the very light green zone, continuing with an evolving fluid variation seen by very fine scale color zoning throughout the second half of the remaining ~ ~2.5 mm of crystal towards its end top.

Studies that investigated color zoning in emeralds include that of Cui et al. (2023) of emeralds from Davdar, China by EMP analysis. The emeralds exhibit multiple-color or concentric zoning with colorless core-green rim growth zonation and variable amounts of Cr and V indicating periodic growth and changes in the crystallization environment. This zoning contrasts with that in the zoned emerald crystal from Colombia that exhibits linear zoning varying perpendicular to the c axis that started by a green color lower zone and ended in a very light green upper color zone. This suggests different crystallization conditions for the emeralds

from the two localities, which can be explained, at least in part, by emeralds from Colombia crystallizing in veins within black shales and those from China crystallizing in veins within slate. However, both show episodic changes during growth but fluids evolved differently.

In a study on emeralds from Malipo, Yunnan, China, Hu and Lu (2019) employed Raman spectroscopy, X-ray diffraction (XRD), laser ablation-inductively coupled plasma-mass spectrometry (LA-ICP-MS), micro UV-Vis, and EPR spectroscopy to show that the yellowish-green color was due to high V and Cr content. The Malipo emeralds show concentric color zoning perpendicular to the c-axis, ranging from a colorless core to a yellowish green rim, suggested to be due to variations in V and Cr concentrations that increase along the crystal growth direction from core to rim. This elemental and color variation in the emeralds from colorless core to yellowish green rim associated with increasing V and Cr is similar to that in the emeralds from Davdar, China, but differ from the results of the zoned emerald crystal of the present study that show a starting green bottom part transitioning to a very light green top with further fluctuations associated with decreasing Fe and Cr contents, and to a lesser extent, Mn and V. These differences evidence contrasting crystallization histories and formation processes.

Variation of Fe K-edge pre-edge XAS parameters with green color zoning

Wilke et al. (2001) showed in a study of Fe K-edge XANES of natural minerals and synthetic compounds, that the pre-edge centroid and total integrated intensity are the most reliable pre-edge parameters for extracting information about oxidation state (Fe^{2+} and Fe^{3+}) and coordination geometry of Fe (tetrahedral (^{IV}Fe) and octahedral (^{VI}Fe)). They show that in a graph of centroid position *vs.* integrated intensity, the position and separation between the average pre-edge centroid positions for Fe^{2+} and Fe^{3+} is different (by 1.4 ± 0.1 eV), and the centroid position

for mixed Fe^{2+}-Fe^{3+} compounds occurs between those two. This difference in centroid position with Fe valence can be used to measure the average Fe oxidation state of Fe in minerals, confirming earlier observations by Bajt et al. (1994). In addition, distinctly different trends of pre-edge centroid position *vs.* pre-edge integrated intensity can be observed for minerals with varying coordination environments and oxidation state. Although results examining the pre-edge features of Fe in different oxidation states and coordination environments ($^{VI}Fe^{3+}$, $^{VI}Fe^{2+}$, $^{IV}Fe^{3+}$, $^{IV}Fe^{2+}$) suggest that the pre-edge position and peak area for these mixtures can vary non-linearly with the average oxidation state of Fe, these variables were used by Wilke et al. (2001) to estimate the Fe^{3+}/Fe^{2+} ratio in 12 minerals containing unknown amounts of Fe^{2+}/Fe^{3+} in different coordination environments.

Utilizing the methods of Wilke et al. (2001), a combination of synchrotron micro-XRF and micro-XANES was used to characterize the color response in colored glass vessels by Arletti et al. (2008). Fe K-edge micro-XANES spectra were collected to map the oxidation state of Fe across the samples, using the pre-edge extraction procedure from Wilke et al. (2001) to determine the position and intensity of the pre-edge peaks. Although the study did not focus on beryl, the approach used was like that taken in the present study presented below, and it was useful in determining the relative oxidation state of Fe in different colored zones of the vessels. The present study also utilized synchrotron-based micro-XRF and micro-XAS to determine the relative oxidation state of Fe in different colored zones within a zoned emerald, but it also used EXAFS in addition to pre-edges. This study is the first to combine synchrotron-based XAS and micro-XRF analysis of green beryl and present detailed chemical maps in a zoned emerald, which is useful in understanding the relationship between Fe, Cr, V, and Mn contents, XAS and EXAFS parameters, and color variation.

Following Wilke et al. (2001), results from the Fe K-edge XAS pre-edge fitting of the zoned emerald data were used to plot the different green color spot analyses in the graph of Fe K-edge pre-edge fit centroid *vs.* integrated intensity (Fig. 9a). Wilke et al. (2001) provided the basis for understanding the relationship between pre-edge centroid energy and the relative valence state of Fe. Initially, the centroid values of the zoned emerald studied here were rescaled (shifted) to fit the results of Wilke et al. (2001) by calibrating the energy from the Fe foil of the present study (7110.913eV) to the energy of the Fe foil of Wilke et al. (2001) (7111.08 eV) following the method from Giuli et al. (2002). Then, the centroid position of the two end members of 6-fold coordinated Fe^{3+} and Fe^{2+} (7113.3 and 7111.9 eV, respectively) from Wilke et al. (2001) were determined. However, because crystal orientation effects are not well understood and affect the results, in this study we did not attempt to use the end-member centroid positions of $^{VI}Fe^{2+}$ and $^{VI}Fe^{3+}$ of that study to quantify Fe^{3+}/Fe^{2+} ratios or Fe^{2+} and Fe^{3+} percentages for the two color areas in the zoned emerald crystal.

Comparison of the data obtained with the relative position of the model end-members $^{VI}Fe^{3+}$, $^{VI}Fe^{2+}$, $^{IV}Fe^{3+}$, and $^{IV}Fe^{2+}$ of Wilke et al. (2001) in the same graph show that all spot analyses plot between the centroid of end members for 6-fold Fe^{2+} and Fe^{3+} end members (Fig. 9b). These results for the zoned emerald that indicate the presence of Fe as both Fe^{2+} and Fe^{3+} in predominately 6-fold coordinated sites agree with the synchrotron Fe K-edge XAS study of blueish-green beryl crystals of Bunnag et al. (2020) (Table 5). They analyzed blue, light blue, and blueish-green beryl samples comparing pre-edge features with those of Fe^{2+} and Fe^{3+} from FeO and Fe_2O_3 standards and using the pre-edge fit model of Wilke et al. (2001) in a modified plot of $E\text{-}E_0$ (the energy of the reference Fe foil – the absorption threshold from Wilke et al., 2001) *vs.* integrated intensity. Based on the position of pre-edge features in the plot, the authors

identified the presence of Fe as both Fe^{2+} and Fe^{3+} residing predominantly in 6-fold coordination sites in the blueish-green sample, consistent with the results of the present study.

Significance of pre-edge centroid differences for Fe^{3+}/Fe_{Tot} variations with green color

Although there is a lack of studies of the relationship of Fe pre-edge XAS parameters in zoned emeralds with color and the cause of the green color and color variations, Chankhantha et al. (2016) utilized XANES (and UV-VIS-NIR) to study the oxidation state of Fe of green beryl (called aquamarine in the study) upon heating (Table 5). They used the E_0 values of the green beryl compared to those of FeO and Fe_2O_3 standards to determine that green beryl crystals originally had octahedral Fe^{3+}, with Fe^{2+}, and that the green colors originate from Fe^{3+} residing in the octahedral site, but the presence of Fe^{2+}, which can be seen in UV-VIS-NIR spectra, in octahedral or channel sites was also considered. These results agree with those of the present study that suggest that both Fe^{2+} and Fe^{3+} are present. However, the study only compared XANES edges but did not perform an analysis of pre-edge features, although pre-edge differences can be seen in the XANES spectra between the original green beryl and the blue colored beryl formed after heating, and the nature of a pre-edge peak (at 7115 eV) was not identified. In the second available synchrotron based XAS study of green beryl, Eeckhout et al. (2005) reported two pre-edge peaks (with centers at 7113.82 and 7115.41 eV), similar to the results of the present study (centers at 7112.5 and 7114.1 eV). A comparison of E_0 with standards confirmed the occurrence of Fe^{3+} and Fe^{2+}, and from pre-edges identified octahedral Fe^{3+} but could not confirm the presence of octahedral Fe^{2+} due to the small pre-edge features of this ion. Below, we explore further the pre-edge characteristics of the emerald crystal investigated here.

The relative position on the graph of the two color zones of the zoned emerald studied here show the green color zone having a lower pre-edge fit centroid energy plotting closer to the Fe^{2+} end member than the very light green zone characterized by a higher energy centroid (Fig. 9). The higher pre-edge centroid energy that characterizes the very light green spots can be interpreted as indicating a higher percentage of $^{VI}Fe^{3+}$ or higher average Fe oxidation state (Fe^{3+}/Fe_{Total}) compared to the green zone spots that have lower centroid energy positions reflecting a larger proportion of $^{VI}Fe^{2+}$ and lower amounts of $^{VI}Fe^{3+}$ or lower average Fe^{3+}/Fe_{Total}. Similarly, the analysis of Bunnag et al. (2020) indicates that the blueish-green sample has a lower centroid (oxidation state) than some of the light-colored beryl when the X-rays are oriented perpendicular the c axis, which is consistent with the results of the zoned emerald that show the green zone having a lower centroid than the very light green zone. According to Bunnag et al. (2020), the greenish-blue beryl (their AQ03 sample) contains both Fe^{3+} and Fe^{2+} in octahedral and interstitial sites, and this specific configuration of iron resulted in a darker color shade compared to the other beryl samples. This agrees with the postulation that green beryl and emerald likely contain Fe^{3+} and Fe^{2+} in 6-fold coordination or in different crystallographic sites (Table 6; Wood & Nassau, 1968; Platonov et al., 1979a, 1979b; Mathew et al., 2000; Spinolo et al., 2007; Andersson 2013; Viana et al., 2022). The study also could not distinguish between the 6-fold coordinated site of Al^{3+} and the 6g interstitial site between two Al sites.

Pre-edge of zoned emerald vs. red beryl as proxy to Fe^{3+}/Fe_{Total} and relation to green color

Further analysis of the pre-edge of the zoned emerald shows a strong positive correlation between pre-edge centroid position and integrated intensity that correlates with the green and very light green color zones ($R^2 = 0.94$; Fig. 9a). A strong positive linear correlation showing

consistently higher integrated intensity and pre-edge fit centroid position energy for the very light green zone compared to the green zone that has lower centroid and integrated intensity implies a slightly different distortion of the octahedral coordination, with either the presence of a minor tetrahedral component or Fe atoms located in channel or interstitial sites in the very light green color zone, and these are discussed below. The pre-edge characteristics obtained here for the two green color zones of the zoned emerald crystal suggest slight variations in the Fe local environment with green color variations, which may affect its electronic structure and, hence, its coloration.

Compared to the red beryl crystal from the Wah Wah Mountains, Utah, USA, both the green and the very light green zones of the emerald have considerably lower pre-edge centroid and integrated intensity values (Fig. 9b; Table 2). A strong positive correlation is also observed between pre-edge parameters that distinguishes the zoned emerald and the red beryl using a slightly different pre-edge fitting (fit energy range 7109.5-7115.8 eV. baseline skip range 7110.2-7115.2 eV). There is also a clear difference between the centroid energy and integrated intensity for green spot analyses of the zoned emerald, which have the lowest centroid energy and integrated intensity, the very light green zone, which has an intermediate centroid and integrated intensity, and the red beryl, which has the highest energy centroid and integrated intensity (Fig. 9b). This is consistent with previous studies of red beryl that reported it to only have octahedral Fe^{3+} (Andersson, 2013, 2019; Gatta et al., 2022), including an absence of Fe^{2+} in the Mössbauer spectrum strongly indicating octahedral Fe^{3+} (Fridrichová et al., 2017). Similarly, Andersson (2013) reported abundant octahedral Fe^{3+} ions in red beryl utilizing EPR, and no Fe^{2+} bands present in the OA spectrum (Andersson, 2019). Based on the integrated intensity (ranging from 0.7674 to 0.07859) being close to the octahedral field in the model of Wilke et al. (2001),

the coordination of Fe in the zoned emerald and red beryl suggests octahedral coordination, consistent with previous studies by other techniques (Wood and Nassau, 1968; Mathew et al., 2000; Spinolo et al., 2007; Platonov et al., 2016; Andersson, 2019; Gatta et al., 2022; Viana et al., 2022). If the centroid and integrated intensity values of red beryl are considered to represent octahedral Fe^{3+}, it is inferred that the positions of the green color and very light green color of the zoned emerald crystal in the same graph represent successively increasing amounts of octahedral Fe^{3+} or higher Fe^{3+}/Fe_{Total}, consistent with the comparison of pre-edge parameters with the relative positions of the end members of Wilke et al. (2001) and the decreasing amounts of Fe, Cr, V, and Mn evidenced by micro-XRF. In other words, the change from green to very light green color represents increasing Fe^{3+}/Fe_{Total} during crystallization, consistent with evolution of hydrothermal fluids to higher redox conditions and lower concentration of chromophore elements during cooling and crystallization.

To further understand the relationship between pre-edge peak parameters and green color variations in the zoned emerald and the significance for Fe valence state, the ratios of peak height and amplitude for the two peaks (P1 and P2) were calculated and plotted along with those of the red beryl against pre-edge peak parameters of known meaning. In a plot of fit centroid *vs.* P2/P1 amplitude, a strong positive correlation is observed with color, with the red beryl clearly distinguished by having the highest centroid and P2/P1 amplitude compared to the zoned emerald (Fig. 9c; $R^2 = 0.7983$). The same positive correlation and relationship with color is observed between the fit centroid and P2/P1 height (in the un-smoothed data fitting) (Fig. 9d; $R^2 = 0.8579$). The very light green zone has higher P2/P1 amplitude and P2/P1 height ratios than the green zone. Values calculated of P2/P1 are smaller than 1, reflecting the visual observation that the height and amplitude of the peak located at lower energy is larger than the one located at

higher energy (Fig. 4). It follows that P2/P1 ratios can be considered to represent Fe^{3+}/Fe^{2+} or Fe^{3+}/Fe_{Total} ratios, similar to centroid values, which in minerals or crystals with significantly large differences in Fe^{3+}/Fe^{2+}contents can be used to explain redox changes recorded in minerals in different processes and geologic environments.

Using the red beryl to represent iron dominantly as Fe^{3+} (Andersson, 2013, 2019; Fridrichová, et al., 2018; Gatta et al., 2022), the lower P2/P1 amplitude and height ratios and centroid of the green zone compared to the very light green zone suggests that Fe in the green emerald color has lower average valence state (lower Fe^{3+}/Fe^{2+}) compared to that in the very light green color (higher Fe^{3+}/Fe^{2+}). This interpretation is also consistent with previous studies that report that green beryl and emerald can contain ferric and ferrous Fe in various amounts and coordination geometries and in different crystallographic sites (e.g., Andersson, 2019; Gatta et al., 2022; Table 6), but provides a quantitative way to distinguish light from darker green color generation using pre-edge Fe K-edge XAS analysis.

Significance of Fe^{3+}/Fe_{Total} and Fe coordination from pre-edge for green color variations

In the zoned emerald crystal, the higher centroid, integrated intensity, and peak ratios in the very light green compared to the green zone is interpreted as indicating a higher Fe average oxidation state (Fe^{3+}/Fe_{Total}) for the former. Although the integrated intensity alone compared to Wilke et al. (2001) end members suggests an octahedral coordination for both, the higher centroid and integrated intensity in the very light green zone and lower in the green zone suggests that some of the ferric Fe in the very light zone may be located in another position in addition to octahedral and that more Fe in the green beryl zone may correspond to $^{VI}Fe^{2+}$ or

Fe^{2+}in another position. In addition, the observed relationships imply that a higher percentage of Fe^{3+} does not correspond to a darker green color in emeralds and that the amount of Fe^{2+} may have a stronger effect in darkening the green color that characterizes emeralds. However, a role of $^{VI}Fe^{2+}$ in darkening the green color of emerald has not been reported in previous studies, as octahedral Fe^{2+}, in addition to tetrahedral Fe^{2+} and Fe^{3+}, and Fe^{3+} in the channel site do not generate color in beryl (Table 6; Wood & Nassau, 1968; Goldman et al., 1978; Mathew et al., 2000; Andersson, 2019; Taran & Vyshneyskyi, 2019). Therefore, it is possible that the lower centroid of the green beryl zone reflecting a lower average valence state of Fe may indicate Fe^{2+} in a different crystallographic position, particularly in the channel site, and this substitution has been reported in green beryl (e.g., Wood & Nassau, 1968; Fritsch & Rossman, 1988; Mathew et al., 2000; Chankhantha et al., 2016; Table 6). In addition, considering the higher integrated intensity and fit centroid, some ferric Fe in the very light green beryl could be located in a tetrahedral, channel, or interstitial positions, thus diminishing the darker green color compared to the earlier-formed part of the crystal (e.g., Wood & Nassau, 1968, Mathew et al., 2000). These observations are only partly consistent with some studies on Fe substitution and the causes of color in beryl that concluded that the green color of beryl and emerald contain mostly octahedral Fe^{3+} (Table 6; Dvir & Low, 1960; Wood & Nassau, 1968; G. Rossman, unpub. Data, Fritsch & Rossman, 1988; Spinolo et al., 2007; Chankhantha et al., 2016; Viana et al., 2022). However, the presence of Fe^{2+} in the zoned emerald is consistent with some studies that also report the occurrence of Fe^{2+} in green beryl residing in octahedral, tetrahedral, or channel sites (Wood and Nassau, 1968; Fritsch & Rossman, 1988; Mathew et al., 2000; Spinolo et al., 2007; Chankhantha et al., 2016; Platonov et al., 2016; Taran & Vyshneyskyi, 2019; Viana et al., 2022). Other studies of light green beryl with different spectroscopic techniques or even by synchrotron XAS could

not identify the presence of small amounts of Fe^{2+} (e.g., Chankhantha et al., 2016). In this study, we show that the high brilliance of synchrotron radiation X-ray spectroscopy allows to identify Fe of different valence states in crystals, including small amounts of Fe^{2+}, and quantify the differences by the new methods described above. Further synchrotron XANES/EXAFS pre-edge studies of green color zoned beryl will allow to determine if the centroid – green color – Fe valence state relationships identified are universally responsible for generating the darker green color typical of emerald.

Sensitivity of pre-edge data analysis and reproducibility of results

To investigate the sensitivity of data analysis in yielding consistent pre-edge parameters and relationships between them and with color, two separate models were applied by changing the energy window and baseline skip range in the pre-edge fitting of the zoned emerald. In addition, the pre-edge fit was performed on the zoned emerald by comparing the results of smoothing the spectral data and without smoothing the data. The pre-edge fit model using an energy fit range of 7109.5-7115.8 eV and baseline skip range of 7110.0-7115.2 eV in both smoothed and un-smoothed forms yielded the best correlation between the parameters centroid energy, integrated intensity, Fe intensity, and peak ratios effectively separating green and very light green color in all data fittings (Fig. A2). The results show that the green spots have a lower pre-edge centroid and integrated intensity than the very light green spots. Similar results are observed in the zoned emerald using a slightly different fit energy range (7109.0-7116.0 eV) and a baseline skip range (7110.2-7115.2 eV) (Fig. A3). Smoothed and un-smoothed pre-edge fittings with these latter parameters show differences between color zones but with less

correlation due to outliers. However, the general trend of differences between the color zones remains unchanged.

The fitting results for the fit energy range of 7109.0-7116.0 eV and a baseline skip range of 7110.2-7115.2 eV for the smoothed data set yield the highest correlation value among all the pre-edge parameters and between pre-edge centroid *vs.* P2/P1 height that correlate with the green and very light green color zones (Fig. 9c; $R^2 = 0.9544$). A positive correlation is observed in the un-smoothed fitting, although one outlier is within the very light green zones (not shown). The pre-edge fitting using a fit energy range of 7109.5-7115.8 eV and baseline skip range of 7110.0-7115.2 eV also yields a positive correlation between the fit centroid, P2/P1, and the different colors ($R^2 = 0.903$; not shown).

Relations between Fe coordination and bond lengths from EXAFS and green color variations

Although XAS pre-edge analysis provides information to distinguish Fe atomic environment between octahedral and tetrahedral coordination, EXAFS analysis can provide details about bond lengths of the absorbing Fe atom and its nearest neighbors that can be used to determine coordination geometries and valence state of Fe, which are known to affect color in beryl. Below, a review of the structure of beryl and the possible location of Fe ions in different coordination geometries and bond lengths is presented to then discuss the results of the EXAFS analysis in the light of pre-edge results and previous studies.

Review of location, coordination, and interatomic distances of Fe in beryl's crystal structure

Beryl's structure has several crystallographic sites where Fe atoms can reside, including the octahedral Al^{3+} site, the interstitial 6g position, the interstitial 4d position, the tetrahedral Be^{2+} position, and channel sites (Fig. 1; Platonov et al., 1979a, b; Přikryl et al., 2014; Taran & Vyshnevskyi, 2019). The dark green color of emerald is primarily explained by trace amounts of Cr^{3+} or V^{3+} ions replacing Al, with some having Fe^{3+}, whereas pale green, blue, and yellow beryl are colored by relative amounts of octahedral Fe^{3+}, channel Fe^{2+}, tetrahedral Fe^{2+}, and/or tetrahedral Fe^{3+} within the crystal lattice (Table 6; e.g., Wood & Nassau, 1968; Přikryl et al., 2014). More specifically, pale to dark green beryl varieties have also been associated with Fe located in the structure of beryl that undergo charge transfer of Fe^{3+} and Fe^{2+} in octahedral, tetrahedral, channel, or interstitial sites, in combination with IVCT between adjacent Fe pairs (Wood & Nassau, 1968; Mathew et al., 2000; Viana et al., 2002; Platonov et al., 2016; Taran et al., 2018; Taran & Vyshnevskyi, 2019). Similarly, in optical absorption studies of green beryl, IVCT between octahedral and tetrahedral Fe^{2+} and mostly octahedral Fe^{3+} with minor amounts occurring in channel or interstitial sites were identified as the cause of the green color (Table 6; Wood & Nassau, 1968; Mathew et al., 2000). Oxygen-metal charge transfer between octahedral Fe^{3+} and Fe^{2+} in the channel site was also concluded in a study of green beryl from Brazil (Fritsch & Rossman, 1998), whereas IVCT between octahedral Fe^{3+} and tetrahedral Fe^{2+} and octahedral Fe^{3+} oxygen charge transfer was reported to be the cause of green color of beryl/emerald from Volyn, Ukraine (Platonov et al., 2016). In addition, Taran and Vyshnevsky (2019) studied the substitution of Fe^{2+} for Be^{2+} in eleven gem-quality colorless to blue and green Fe-bearing beryl with varying color intensities from the Brazilian pegmatite deposits Lavra do Abilio (Minas Gerais) and Garimpo do Cercadinho (Bahia) using polarized optical absorption micro-spectroscopy and electron microprobe analysis. Although due to the relatively low

concentration of $^{Be}Fe^{2+}$ in the beryl crystal-structure refinements could not confirm the presence of Fe^{2+} replacing Be^{2+}, distinct differences in the $^{Al}Fe^{2+}$-, $^{Al}Fe^{3+}$- and $^{Be}Fe^{2+}$-content of Fe-bearing beryl crystals were identified, including variations in the distribution of $^{Be}Fe^{2+}$ along the c axis between these two deposits. Přikyl et al. (2014) considered that green beryl have similar amounts of octahedral Fe^{3+}, but that tetrahedral Fe^{2+} varies and is typical of green beryl.

In beryl, the Al sites are positioned above and below each 6g site so that 6g-Al vectors are parallel to the c axis with an Al-6g distance of 2.300 Å (Fig. 1; Table 4; Groat et al., 2010). The $6gO_6$ polyhedron shares {001} triangular faces with two AlO_6 octahedra and is slightly larger than the AlO_6 octahedron. The 6g position has six oxygen atoms in trigonal prismatic coordination with 6g-O distances of 2.161 Å, whereas the AlO_6 octahedra has Al-O distances estimated between 1.904 Å and 1.955 Å (Table 4; Groat et al., 2010; Bačík & Fridrichová, 2019). The Fe ions that substitute at the Al site thus could also substitute at the 6g position, but only in very small amounts, because of the need to maintain local charge-balance. The 4d position has four oxygen atoms in square planar coordination at distances of 1.870-1.891 Å, and the Be positions are arranged above and below each 4d site, such that the 4d–Be vectors are parallel to c, whereas the 4d–Si and 4d–6g vectors are perpendicular to c (Groat et al., 2010; Lin et al., 2014; Bačík & Fridrichová, 2019). Bačík & Fridrichova (2019) presented the average bond lengths of ferrous and ferric iron in different coordination based on analysis of 64 published beryl structures and found that the average bond length for Fe^{2+}-O in octahedral coordination is 2.154 Å, whereas in tetrahedral coordination it is 1.968 Å (Table 4). For Fe^{3+}-O, the average bond length is 2.016 Å in octahedral coordination and 1.870 Å in tetrahedral coordination. These coordination environments and bond distances are considered below in relation to EXAFS modeling results for the zoned emerald to understand green color variations.

Fe coordination and probabilities of Fe bonds and lengths from EXAFS analysis

The FEFF calculations derived from X-ray Larch report the distance to the nearest neighboring atom from the absorbing Fe atom. The graph of R space *vs.* probability (chi) is offset toward higher values by approximately 0.5 Å from the X-Ray Larch plot of R (Å) *vs.* $|\chi(R)|(A^{-3})$ (Fig. 8). The study of the FEFF fitting of the Fe K-edge EXAFS area data of the color-zoned emerald crystal shows three noticeable R-space peaks in the graph of R (Å) *vs.* $|\chi(R)|(A^{-3})$ similar to those obtained by Lin et al. (2013) in the Fe K-edge EXAFS study of a blueish-green beryl (Fig. 8; Table 3). Bond lengths calculated using FEFF R-space fittings were determined from an Fe atom in the octahedral Al site to its nearest neighbors.

The Fe-O bond (peak 1) for the zoned emerald shows that the probability of Fe occurring in an octahedral coordination substituting for Al is the highest, with Fe-O bond lengths obtained (1.9295 Å to 1.9483 Å; average 1.9422 Å) overlapping, and the average for the green zone being slightly longer (1.9428 Å) than that for the very light green zone (1.9418 Å) (Fig. 8; Table 3). Compared to the average obtained for Fe-O bond lengths for the red beryl crystal (1.9809 Å), the average Fe-O bond length in the zoned emerald is slightly shorter (by 0.0387 Å) (Fig. A4; Table 3). Of the possible octahedral atomic positions within the beryl crystal that Fe can occupy to explain the Fe-O bond lengths obtained from EXAFS analysis (and pre-edge XANES reflecting octahedral coordination), the Al-O octahedral site and the 6g-O octahedral interstitial site are considered. Of these, the Fe-O R values obtained for the zoned emerald (avg. 1.9422 Å) are much closer to that for Al-O (by 0.0172 Å; avg. 1.925 Å) than to 6g-O (different by 0.2188 Å; 2.161 Å). The Fe-O bond distances obtained for the zoned emerald and red beryl are similar to

those obtained for Cr-O bonds (1.97 Å) with Cr replacing Al in octahedral coordination in emerald in the EXAFS Cr study of Gaudry et al. (2007) (Table 6).

Results of FEFF fitting show a very small probability (peak 2) identified by the Fourier transform analysis for the occurrence of a model (2.3 Å) Fe-Fe bond within the zoned emerald, with modeled distances ranging from 2.0538 to 2.0724 Å (Fig. 8; Tables 3, 4). Based on available bond distances from the literature and the model used, these R distances are interpreted to represent an Fe-Fe pair between the Al octahedral site and the nearest 6g site (Table 5). This is consistent with the XANES, EXAFS, and EPR spectroscopy study of Lin et al. (2013), who provided the first experimental verification suggested in previous studies (Platonov et al., 1979a, b; Eeckhout et al., 2005; Groat et al., 2010) of IVCT between Fe^{3+}-Fe^{2+} pairs, with Fe^{3+} at the octahedral Al site and Fe^{2+} at its nearest 6g interstitial position in a light blue beryl. The best EXAFS model of Lin et al. (2013) reproduced the five peaks in the experimental spectrum, providing evidence of IVCT being responsible for the blue color of the sample. Modeling for red beryl also yielded a small probability of occurrence of an Fe-Fe bond that resulted in longer model R-space distances (avg. 2.5344 Å) compared to shorter distances in the zoned emerald (avg. 2.0651 Å) (Table 4). Lin et al. (2013) also considered that another Fe pair could be located in two adjacent Al sites at a distance of 4.6 Å. However, after numerous attempts, modeling beyond 4 Å was not possible with the data obtained in this study.

Results of the pre-edge XANES and EXAFS analysis that suggest the presence of Fe^{2+} and Fe^{3+} dominantly in octahedral coordination in the green and very light green zones of the zoned emerald (Fig. 9b; Tables 4, 5) are also consistent with the findings of Taran and Vyshnevsky (2019) in certain crystals from Lavra do Abilio that exhibited a green hue, a coloration typically attributed to a combination of Fe^{3+} and Fe^{2+} color centers (e.g., Viana et al.,

2002). Next, the relative valence state and coordination geometry for Fe in the zoned emerald and red beryl are explored further by using the fit centroid energy and Fe-O and Fe-Fe bond lengths obtained from FEFF R-space fitting modeling and comparing the zoned emerald and red beryl values with each other and with Fe^{2+}-O and Fe^{3+}-O bond lengths in tetrahedral and octahedral coordination from the literature (Fig. 10a; Table 5).

Significance of pre-edge XAS parameters and EXAFS bonds in zoned emerald and red beryl for green color variations

A comparison of the pre-edge fit centroid and the calculated bond lengths for Fe-O and Fe-Fe obtained from R-space fitting of EXAFS data of the different spot analyses in the very light green and green areas in the zoned emerald crystal was made to identify any correlations with color. Results from R-space Fe-O fitting for the zoned emerald show that although Fe-O bond lengths vary slightly (1.929 – 1.948 Å) they are similar for the green and very light green zones and overlap (Fig. 10a; Table 3), which implies that there is no significant difference in Fe-O length and no correlation exists between Fe-O bond distance and color for the green and very light green zones. The shortest and longest distances for Fe-O are observed in the very light green spot analyses. In addition, the average Fe-O distance for the very light green spot analyses (1.9418 Å) is only slightly shorter than that for the green spot analyses (1.9428 Å). In addition, no correlation is observed between the pre-edge fit centroid and octahedral Fe-O bond lengths because bond lengths in both color zones are similar and overlap (Fig. 10a; $R^2 = 0.1179$). Overlapping Fe-O distances may indicate the presence of Fe residing in the same octahedral coordination site in all the spots analyzed with slight variations in the distortion of the octahedra. Overall, no correlation exists between EXAFS Fe-O bond length parameters, Fe intensity, and

green color variations within the zoned emerald crystal. Because of the analytical conditions used, the resolution for EXAFS analysis may not be high enough to allow precise determinations of bond lengths to distinguish small differences between spots in the two different green colors. Alternatively, Fe-O bond distances are indeed not measurably different, but further EXAFS studies of similar crystals at higher resolution can determine if there are any real differences.

In contrast, in a graph of pre-edge Fe centroid *vs.* Fe-Fe R modeled distance, a strong positive correlation is observed with color variation for the zoned emerald ($R^2 = 0.84$; Fig. 10b). The Fe-Fe bond distances obtained for the green zone (avg. 2.0584 Å) and very light green zone (2.0651 Å) overlap slightly, with the very light green spot analyses having a slightly longer Fe-Fe bond length than the green spot analyses. Although there is some overlap, the shortest Fe-Fe distances correspond to the green beryl zone, whereas the longest were obtained for the very light green zone. If Fe-Fe pairs impart green coloration to beryl or darken the green color generated by other chromophores, a longer Fe-Fe distance in the very light green zone compared to the green zone of the crystal is consistent with shorter distances between Fe pairs causing darker colors (e.g., Lin et al., 2013). Due to the small probability for Fe-Fe bond to exist, this will not be discussed further.

The average obtained Fe-O modeled distance for the zoned emerald (avg. 1.9422 Å) is very close to the distances reported for octahedral Fe^{2+}-O in green beryl by Goldman et al. (1978; 1.95 Å; differ by 0.0078 Å) and tetrahedral Fe^{2+}-O (1.968 Å; differ by 0.0197 to 0.0385 Å, avg. 0.026 Å) by Bačik & Fridrichová (2019) and smaller than the distances reported by Groat et al. (2010) and Bačik & Fridrichová (2019) for octahedral Fe^{2+} (2.154 Å; differ by avg. 0.212 Å) and octahedral Fe^{3+} (2.016 Å; differ by avg. 0.074 Å; Table 5). Tetrahedral Fe^{3+}-O (1.87 Å) is the only reported distance shorter than the average modeled for the zoned emerald

(different by ~0.0722 Å). The Fe-O distances for the zoned emerald (avg. 1.9422 Å) are slightly closer but similar to tetrahedral Fe^{2+}-O (1.968 Å; differ by 0.0197 to 0.0385 Å, avg. 0.026 Å) than octahedral Fe^{3+}-O distances (2.016 Å; differ by avg. 0.074 Å) obtained by Bačik & Fridrichová (2019). The average Fe-O distance for the zoned emerald is between those for $^{IV}Fe^{2+}$-O (differ by 0.026 Å) and $^{IV}Fe^{3+}$-O (1.87 Å) (differ by 0.072 Å) and $^{VI}Fe^{3+}$-O (2.016 Å; by 0.074 Å) (Table 5). Overall, for the zoned emerald the difference between Fe-O values obtained and available Fe-O distances for tetrahedral Fe^{3+} and octahedral Fe^{3+} is almost the same (~0.07 Å). These bond length comparisons show that Fe-O distances obtained here for the zoned emerald (avg. 1.9422 Å) are closer (by 0.01 to 0.03 Å) to tetrahedral Fe^{2+}-O (1.968 Å) than octahedral Fe^{3+}-O (2.016 Å) obtained by Bačik & Fridrichová (2019).

For red beryl, the average Fe-O bond length (1.981 Å) falls between those for $^{IV}Fe^{2+}$-O (1.968 Å) and $^{VI}Fe^{3+}$-O (2.016 Å), with the difference between the values for Fe-O in red beryl and $^{IV}Fe^{2+}$-O being slightly smaller (differ by 0.013 Å) than the difference with $^{VI}Fe^{3+}$-O (differ by 0.035 Å). The Fe-O R values obtained from the R space model for the zoned emerald (avg. 1.9422 Å) and red beryl (avg. 1.98 Å) differ slightly (by 0.04 Å), with that for red beryl being slightly longer. The modeled Fe-O distances for the red beryl and the zoned emerald are closer to octahedral Fe^{3+}-O than octahedral Fe^{2+}-O. However, Fe-O distances for red beryl and the zoned emerald are of the same order of magnitude (differ by 0.04 to 0.07 Å) for octahedral Fe^{3+} as for tetrahedral Fe^{2+}. On the other hand, Fe-O values for the red beryl and zoned emerald are most different (by 0.17 to 0.21 Å) from octahedral Fe^{2+}-O (2.154 Å) than all other reported Fe-O bond lengths.

The average Fe-O R distance obtained from the R space model for red beryl (avg. 1.98 Å) is very close to the Fe-O distance (1.99 Å) reported by Lin et al. (2013) obtained from fitting of

EXAFS data of a blue beryl. The pre-edge fit centroid average obtained here for red beryl (avg. 7112.82 eV) being higher than for the zoned emerald (avg. 7112.71 eV) suggests a higher average valence state for the former (Fig. 9; e.g., Wilke et al., 2001). From previous studies, Fe in red beryl is expected to be only or mostly ferric Fe, confirmed by the absence of ferrous Fe in Mössbauer spectra (Fridrichová et al., 2018; Andersson, 2019; Gatta et al., 2022), and located at the octahedral coordination site, which is consistent with the higher average centroid value for red beryl. Because the obtained pre-edge integrated intensity values are slightly lower for the zoned emerald than for red beryl, and they both fall close to octahedral Fe in the model of Wilke et al. (2001) (Fig. 9 b-d), they are inconsistent with average Fe-O distances being close to tetrahedral Fe-O and more consistent with octahedral Fe-O. These relations coincide with the determination of red beryl containing octahedral Fe^{3+} and the zoned emerald having a lower Fe^{3+}/Fe_{Tot}. Further, the higher integrated intensity for the very light green zone than for the green zone of the zoned emerald, combined with modeled Fe-O bond distances being similarly close to octahedral Fe^{3+} than tetrahedral Fe^{3+} suggest the possibility of some Fe occurring as $^{IV}Fe^{3+}$.

With some contribution of octahedral Fe^{2+} in the zoned emerald based on the obtained lower pre-edge centroid values compared to the red beryl and information from previous studies, it is expected to obtain a longer Fe-O bond length in the zoned emerald than in the red beryl, but only if Fe concentrations are the same, which is unlikely but unknown. However, the closeness in the Fe-O values obtained for red beryl and octahedral Fe^{3+}-O (2.016 Å) and less so for the zoned emerald, is consistent with red beryl having more octahedral Fe^{3+} than the zoned emerald. In addition, Fe-O distances obtained for the zoned emerald are closest to those for octahedral Al-O (1.904-1.955 Å; Faye, 1972; Gibbs et al., 1968; Goldman et al., 1978), and more different for the red beryl. The small difference in modeled Fe-O values between the red beryl and the zoned

emerald and the slightly smaller Fe-O value for the zoned emerald can be explained by the occurrence of less octahedral Fe^{3+} in the zoned emerald substituting for Al that creates less distortion (smaller) of the octahedra compared to more Fe^{3+} in red beryl causing a larger distortion of the octahedra (larger; i.e., concentration effect; Fritsch & Rossman, 1988).

Compared with available bond distances from previous studies, the occurrence of octahedral Fe^{2+} can be ruled out due to the order of magnitude difference in Fe-O distances compared to the distances obtained in the current study. The obtained Fe-O distance for the zoned emerald is likely representative of octahedral Fe^{3+} (2.016 Å) rather than tetrahedral Fe^{2+} (1.968 Å; Bacik & Fridrichova, 2019). Previous studies have shown that tetrahedral Fe^{2+} and Fe^{3+} and octahedral Fe^{2+} substitutions are not known to cause color in beryl or emerald by themselves (Wood & Nassau, 1968; Mathew et al., 2000; Andersson, 2019). However, some studies have reported the occurrence of tetrahedral Fe^{2+} in green beryl (e.g., Přikryl et al., 2014).

The results obtained in the present study for Fe-O values for the zoned emerald are consistent with and very similar to those for octahedral Fe-O lengths obtained by Lin et al. (2013), only differing slightly for the studied red beryl (by 0.009 Å) and zoned emerald (by 0.05 Å). This is consistent with previous studies that showed that octahedral Fe^{3+} is present in green beryl and emerald (Dvir & Low, 1960; Wood & Nassau, 1968; Fritsch & Rossman, 1988; Spinolo et al., 2007; Přikryl et al., 2014; Viana et al., 2022). Therefore, we interpret the Fe-O distances obtained by EXAFS fitting to better represent octahedral ferric Fe replacing Al in the zoned emerald. The shorter modeled Fe-O distance in the zoned emerald compared to the red beryl is a distinguishing characteristic of the green color of the emerald that suggests a different amount of Fe in the Al octahedral site and/or location of other Fe atoms in additional crystallographic sites.

CONCLUSIONS

Major highlights and broad contributions from the present study include:

1) This study presents results of the first combined synchrotron micro-XANES Fe K-edge pre-edge, micro-EXAFS, and micro-XRF analysis on a zoned emerald crystal, and comparisons with a red beryl crystal from the Wah Wah Mountains, Utah, USA.
2) The current study reports the first synchrotron-based micro-XRF chemical maps of a green color zoned emerald from Chivor, Colombia, which show noticeable strong variations in Fe, Cr, V, and Mn intensity correlated with green and very light green color zones and sub-millimetric (0.05 mm) scale growth planes perpendicular to the c axis of the crystal.
3) To our knowledge, this is the first study to compare K-edge Fe parameters in two different green colors in the same crystal. Results are consistent with previous studies that report that green beryl and emerald can contain ferric and ferrous Fe in various amounts and coordination geometries and in different crystallographic sites, but provides new quantitative results and analysis to distinguish light from darker green color generation using pre-edge peaks Fe K-edge XAS.
4) The high brilliance of synchrotron radiation X-ray spectroscopy allows to identify the relationship between Fe K-edge pre-edge parameters, green color variations, chromophore intensities, and Fe coordination and bond distances in an emerald crystal.

In detail, the combined synchrotron-based XAS and XRF spectroscopy study of the zoned emerald compared with the red beryl crystal provided the following findings:

5) High-resolution synchrotron micro-XRF mapping of the two-color zoned emerald crystal shows that remarkably higher Fe content in the Cr-rich, followed by V, bottom green zone is responsible for darkening of the green color generated by chromophore Cr, and in less degree V.
6) Results of XAS Fe K-edge pre-edge centroid and integrated intensity relations for the zoned emerald show mostly octahedral iron substitution. A red beryl crystal used for comparison, considered to contain only octahedral ferric Fe, has a higher centroid energy than the zoned emerald (by 0.11 eV).
7) Pre-edge centroid energies for the zoned emerald indicate the presence of octahedral Fe^{3+} and Fe^{2+} in both the green and very light green color zones. A higher overall centroid energy of the very light green zone compared to the green zone suggests that Fe in the very light green color zone has a higher average Fe valence state or more Fe^{3+} than Fe in the green color zone characterized by more Fe^{2+} or lower Fe^{3+}/Fe_{Tot}.
8) Some ferric Fe in the very light green beryl could be located in channel or interstitial positions, thus diminishing the darker green color compared to the earlier-formed part of the crystal.
9) EXAFS analysis of the zoned emerald in the context of the pre-edge data suggests that overlapping modeled Fe-O R distances (1.9295-1.9483 Å, avg. 1.9422Å) in both color zones are consistent with known Fe^{3+}-O distances (2.016 Å) in beryl in distorted Al-O octahedra (avg. 1.925 Å) reported in the literature. Minor incorporation of tetrahedral Fe^{3+}, especially in the very light green area of the zoned emerald crystal is indicated based on model Fe-O bond distances and integrated intensity. This shows the role of octahedral Fe^{3+} in generating and darkening the green color of beryl. Shorter modeled Fe-O distances in the zoned emerald

compared to the red beryl (avg. 1.981 Å) suggest less distortion of the octahedra by lower amounts of octahedral Fe in the zoned emerald, and the presence of Fe^{2+}, than in red beryl.

10) Modeled Fe-Fe bonds (avg. 2.062 Å) in the zoned emerald that have low probability of occurring suggest the location of small amounts of Fe pairs located in Al-6g sites. Longer Fe-Fe distances in the very light green zone than in the green zone suggest that shorter Fe pairs may have a role in generating the darker green color of emerald.
11) Delicate color and corresponding elemental zoning in the green to very light green color emerald crystal reflects a hydrothermal fluid of changing composition starting with high and homogeneous Fe, Cr, and V content, abruptly decreasing in concentration at the two-color boundary, and then varying slightly within a low concentration, very light green zone until final crystallization.
12) Because of the sensitivity of data fitting methods, additional synchrotron-based XAS/XANES/EXAFS investigations of other green-color zoned beryl crystals combined with detailed chemical compositions and/or other spectroscopic techniques will allow to determine if the same pre-edge centroid – Fe valence state – Fe coordination – green color variation relationships identified are universally responsible for generating the darker green color typical of emerald.

ACKNOWLEDGEMENTS

Funding for this study was provided by an East Carolina University Thomas Harriot College of Arts and Sciences Research Initiation Grant (to AHR). Beryl samples 97019.2 and 131716 were provided on loan by the Mineralogical and Geological Museum of Harvard University. This research used resources of the Advanced Photon Source (APS), a U.S.

Department of Energy (DOE) Office of Science User Facility operated for the DOE Office of Science by Argonne National Laboratory under Contract No. DE-AC02-06CH11357. This work was performed at GeoSoilEnviroCARS (GSECARS), The University of Chicago, Sector 13 of the APS, Argonne National Laboratory, IL, and supported by Drs. Tony Lanzirotti and Matt Newville. GSECARS (Sector 13) is supported by the NSF (grant # EAR-1634415) and the U.S. Department of Energy (DOE, grant # DE-FG02-94ER14466). Discussions with Darby Dyar, Elizabeth Cottrelle, and Yuanming Pan in the early stages of data analysis are greatly appreciated.

REFERENCES

Alonso Perez, R., & Day, J. M., 2021. Rare earth element and incompatible trace element abundances in emeralds reveal their formation environments. Minerals, 11, 5, 513.

Andersson, L. O., 2006. The positions of H^+, Li^+ and Na^+ impurities in beryl. Phys Chem Minerals, 33, 403-416. doi:10.1007/s00269-006-0086-x.

Andersson, L. O., 2013. The yellow color center and trapped electrons in beryl. The Canadian Mineralogist, 51, 1, 15-25. doi:10.3749/canmin.51.1.15

Andersson, L. O., 2019. Comments on beryl colors and on other observations regarding iron-containing beryls1. The Canadian Mineralogist, 57, 4, 551-566. https://doi.org/10.3749/canmin.1900021.

Arletti, R., Vezzalini, G., Quartieri, S., Ferrari, D., Merlini, M., & Cotte, M., 2008. Polychrome glass from Etruscan sites: first non-destructive characterization with synchrotron μ-XRF, μ-XANES and XRPD. Applied Physics A, 10.1007/s00339-008-4462-x.

Artioli, G., Rinaldi, R., Stahl, K., & Zanazzi, P. F., 1993. Structure refinements of beryl by single-crystal neutron and X-ray diffraction. American Mineralogist, 78, 762-768.

Aurisicchio, C., Franzini, M., Grubessi, O., & Zanazzi, P. F., 1988. Reappraisal of the crystal chemistry of beryl. American Mineralogist, 73, 826-837.

Aurisicchio, C., Grubessi, O., & Zecchini, P., 1994. Infrared spectroscopy and crystal chemistry of the beryl group. The Canadian Mineralogist, 32, 55-68.

Bačík, P., & Fridrichová, J., 2019. The Site Occupancy Assessment in Beryl Based on Bond-Length Constraints. Minerals, 9, 641. doi:10.3390/min9100641.

Bai, F., Pan, H., & Li, X., 2019. Replacement degree of Al^{3+} and Cr/V ratio in high-V emeralds from Malipo, Yunnan, China12. Arabian Journal of Geosciences, 12, 377. https://doi.org/10.1007/s12517-019-4465-2.

Bajt, S., Sutton, S. R., & Delaney, J. S., 1994. X-ray microprobe analysis of iron oxidation states in silicates and oxides using X-ray absorption near edge structure (XANES). Geochimica et Cosmochimica Acta, 58, 23, 5209-5214. doi:0016-7037(94)00300-9.

Banks, D.A, Giuliani, G., Yardley, B.W.D., and Cheilletz, A., 2000. Emerald mineralization in Colombia: fluid chemistry and the role of brine mixing. Mineralium Deposita, 35, 699–713. https://doi.org/10.1007/s001260050273.

Barton, M. D., & Young, S., 2002. Non-pegmatitic deposits of beryllium: Mineralogy, geology, phase equilibria and origin. Reviews in Mineralogy and Geochemistry, 50, 14. doi:10.2138/rmg.2002.50.14

Berry, A. J., O'Neill, H. St.C., Jayasuriya, K. D., Campbell, S. J., & Foran, G. J., 2003. XANES calibrations for the oxidation state of iron in a silicate glass. American Mineralogist, 88, 967-977.

Bosshart, G., 1991. Emeralds from Colombia (Part 2). Journal of Gemology, 22, 7, 409–425.

Bragg, W. L., & West, J., 1926. The structure of beryl, $Be_3Al_2Si_6O_{18}$. Proceedings of the Royal Society of London. Series A, Containing Papers of a Mathematical and Physical Character, 111, 759, 691-714.

Branquet, Y., Laumonier, B., Giuliani, G., & Cheilletz, A., 1999. Emeralds in the Eastern Cordillera of Colombia: Two tectonic settings for one mineralization. Geology, 27, 7, 597-600. doi:10.1130/0091-7613(1999)027<0597:EITECO>2.3.CO;2.

Bunnag, N., Kasri, B., Setwong, W., Sirisurawong, E., Chotsawat, M., Chirawatkul, P., & Saiyasombat, C., 2020. Study of Fe ions in aquamarine and the effect of dichroism as seen using UV–Vis, NIR and x-ray. Radiation Physics and Chemistry, 177, 109107. https://doi.org/10.1016/j.radphyschem.2020.109107.

Butt, S., Sutton, S.R., Delaney, J.S., 1994. X-ray microprobe analysis of iron oxidation states in silicates and oxides using X-ray absorption near edge structure (XANES). Geochimica et Cosmochimica Acta, 58, 23, 5209-5214.

Berry, A., O'Neill, H., Jayasuriya, K., Campbell, S., Foran, G., 2003. XANES calibrations for the oxidation state of iron in a silicate glass. American Mineralogist, 88, 7, 967-977.

Chankhantha, C., Thanasuthipitak, P., & Kidkhunthod, P., 2016. Iron K-Edge Xanes Study of Heated Green Beryl from Madagascar. Walailak Journal of Science and Technology, 13, 12, 977-983.

Cheilletz, A., & Giuliani, G., 1996. The genesis of Colombian emeralds: a restatement. Mineralium Deposita, 31, 4, 359-364. doi:10.1007/BF00196135.

Copper, P., Tosdal, R. M., & Stacey, J. S., 1995. Geology and geochemistry of the Muzo emerald deposits, Colombia. Economic Geology, 90, 8, 2041-2059.

Cui, D., Wu, Q., Liao, Z., Qi, L., Zhou, Z., Zhang, L., Zhong, Q., Liu, Y., & Li, L., 2023. Growth heterogeneity and zonation characteristics of emeralds from Davdar, Xinjiang, Earth Science Frontiers, 30, 2, 401-414.

Curado, J. F., Radtke, M., Buzanich, G., Reinholz, U., Riesemeier, H., Guttler, R. A. S., & Rizzutto, M. A., 2014. μ-SRXRF characterization of Brazilian emeralds. Journal of Physics: Conference Series, 499, 012016. doi:10.1088/1742-6596/499/1/012016.

Dvir, M., & Low, W., 1960. Paramagnetic resonance and optical spectrum of iron in beryl. Physical Review, 119, 5, 1587-1591.

Dyar, M. D., Gunter, M. E., Delaney, J. S., Lanzarotti, A., & Sutton, S. R., 2002. Systematics in the structure and XANES spectra of pyroxenes, amphiboles, and micas as derived from oriented single crystals. The Canadian Mineralogist, 40, 1375-1393.

Dyar, M., Breves, E., Gunter, M., Lanzirotti, A., Tucker, J., Carey, C., Peel, S., Brown, E., Oberti, R., Lerotic, M., Delaney, J., 2016. Use of multivariate analysis for synchrotron micro-XANES analysis of iron valence state in amphiboles. American Mineralogist, 101, 5, 1171-1189.

Eeckhout, S., Neisius, T., Castañeda, C., 2005. Oxidation effects in beryl induced by synchrotron radiation. Nuclear Instruments and Methods in Physics Research section B: Beam Interactions with Materials and Atoms, 229, 1, 73-77.

Evans, K., Dyar, M., Reddy, S., Lanzirotti, A., Adams, D., Tailby, N., 2014. Variation in XANES in biotite as a function of orientation, crystal composition, and metamorphic history. American Mineralogist, 99, 2-3, 443-457.

Executive Office of the President. 2017. A Federal Strategy to Ensure Secure and Reliable Supplies of Critical Minerals. Federal Register 82(246): 60835-60837. Accessed February 14, 2022.

Fiege, A., Ruprecht, P., Simon, A., Bell, A., Göttlicher, J., Newville, M., Lanzirotti, T., Moore, G., 2017. Calibration of Fe XANES for high-precision determination of Fe oxidation state in glasses: Comparison of new and existing results obtained at different synchrotron radiation sources. American Mineralogist, 102, 2, 369-380.

Figueiredo, M.O., Silva, T., Veiga, J.P., Gomes, C., De Andrade, V., 2008. The blue coloring of beryls from Licungo, Mozambique: An X-ray absorption spectroscopy study at the iron K-edge. Mineralogical Magazine, 72, 175-178.

Figueiredo, M. O., Silva, T., Veiga, J. P., 2010. The blue of iron in mineral pigments: A Fe K-edge XANES study of vivianite. Applied Physics, 99, 357-361.

Fortaleché, D., Lucas, A., Muyal, J., Hsu, T., & Padua, P., 2017. The Colombian emerald industry: Winds of change. Gems & Gemology, 53, 3, 332-358.

Fridrichová, J., Bačík, P., Ertl, A., Wildner, M., Dekan, J., & Miglierini, M., 2017. Jahn-Teller distortion of Mn3±occupied octahedra in red beryl from Utah indicated by optical spectroscopy. Journal of Molecular Structure, 1152, 79-86. https://doi.org/10.1016/j.molstruc.2017.09.081.

Fritsch, E., & Rossman, G. R., 1988. An update on color in gems. Part 2: Colors involving multiple atoms and color centers. Gems & Gemology, 24, 1, 3-15.

Gatta, G. D., Adamo, I., Zullino, A., Gagliardi, V., Lorenzi, R., Rotiroti, N., Faldi, L., & Prosperi, L., 2022. A multi-methodological investigation of natural and synthetic red beryl gemstones. Minerals, 12, 439. https://doi.org/10.3390/min12040439.

Gaudry, E., Cabaret, D., Brouder, C., Letard, I., Rogalev, A., Wilhlem, F., Jaouen, N., & Sainctavit, P., 2007. Relaxations around the substitutional chromium site in emerald: X-ray absorption experiments and density functional calculations. Physical Review B, 76, 9, 094110. doi:10.1103/PhysRevB.76.094110.

Gibbs, G. V., Breck, D. W., & Meagher, E. P., 1968. Structural refinement of hydrous and anhydrous synthetic beryl, $Al_2(Be_3Si_6)O_{18}$ and emerald, $Al_{1.9}Cr_{0.1}(Be_3Si_6)O_{18}$. Lithos, 1, 3, 275-285. https://doi.org/10.1016/S0024-4937(68)80044-1.

Giuli, G., Pratesi, G., Cipriani, C., & Paris, E., 2002. Iron local structure in tektites and impact glasses by extended X-ray absorption fine structure and high-resolution X-ray absorption near-edge structure spectroscopy. Geochimica et Cosmochimica Acta, 66, 24, 4347-4353. doi:S0016-7037(00)01030-X.

Giuliani, G., France-Lanord, C., Cheilletz, A., Coget, P., Branquet, Y., & Laumonier, B., 2000. Sulfate reduction by organic matter in Colombian emerald deposits: chemical and stable isotope (C, O, H) evidence. Economic Geology, 95, 5, 1129-1153. doi:10.2113/gsecongeo.95.5.1129.

Giuliani, G., Fallick, A. E., Garnier, V., France-Lanord, C., Ohnenstetter, D., & Schwarz, D., 2005. Oxygen isotope composition as a tracer for the origins of rubies and sapphires. Geology, 33, 4, 249-252. doi:10.1130/G21261.1.

Goldman, D. S., Rossman, G. R., & Parkin, K. M., 1978. Channel constituents in beryl. Physics and Chemistry of Minerals, 3, 3, 225-235. doi:10.1007/BF00307535.

Grew, E. S., 2002. Mineralogy, Petrology, and Geochemistry of Beryllium: An introduction and list of beryllium minerals. Reviews in Mineralogy and Geochemistry, 50, 1, 1-76.

Groat, L. A., Hart, C. J. R., Lewis, L. L., & Neufeld, H. L. D., 2005. Emerald and aquamarine mineralization in Canada. Geoscience Canada, 32, 2, 65-72.

Groat, L. A., Rossman, G. R., Dyar, M. D., Turner, D., Piccoli, P. M., Schultz, A. J., Ottolini, L., 2010. Crystal chemistry of dark blue aquamarine from the True Blue showing, Yukon Territory, Canada. The Canadian Mineralogist, 48, 3, 597-613.

Hazen, R. M., Au, A. Y., & Finger, L. W., 1986. High-pressure crystal chemistry of beryl ($Be_3Al_2Si_6O_{18}$) and euclase ($BeAlSiO_4OH$). American Mineralogist, 71, 7-8, 977-984.

Hu, Y., & Lu, R., 2019. Unique vanadium-rich emerald from Malipo, China. Gems & Gemology, 55, 3, 338-352. http://dx.doi.org/10.5741/GEMS.55.3.338.

Hu, Y., & Lu, R., 2020. Color characteristics of blue to yellow beryl from multiple origins. Gems & Gemology, 56, 1, 54–65. http://dx.doi.org/10.5741/GEMS.56.1.54.

Ingall, E. D., Brandes, J. A., Diaz, J. M., de Jonge, M. D., Paterson, D., McNulty, I., Elliotte, W. C., & Northrup, P., 2011. Phosphorus K-edge XANES spectroscopy of mineral standards.

Journal of Synchrotron Radiation, 18, 2, 189–197. https://doi.org/10.1107/S0909049510045322.

Lin, J., Chen, N., Huang, D., & Pan, Y., 2013. Iron pairs in beryl: New insights from electron paramagnetic resonance, synchrotron X-ray absorption spectroscopy, and ab initio calculations. American Mineralogist, 98, 10, 1745-1753. http://dx.doi.org/10.2138/am.2013.4472.

Loeffler, B.M., & Burns, R.G., 1976. Shedding light on the color of gems and minerals. American Scientist, 64, 6, 636-647.

Mathew, G., Karanth, R. V., Gundu Rao, T. K., Deshpande, R. S., 2000. Colouration in natural beryls: A Spectroscopic investigation. Journal of the Geological Society of India. 9, 56, 285-303.

Morosin, B. 1972. Structure and thermal expansion of beryl. Acta Cryst. B28, 1899-1903, https://doi.org/10.1107/S0567740872005199.

Newville, M., 2004. Fundamentals of XAFS. Consortium for Advanced Radiation Sources. 1-37.

Newville, M., 2013. Larch: An analysis package for XAFS and related spectroscopies. Journal of Physics. Conference Series, 430:012007.

Ottaway, T., Giuliani, G., & Dubessy, J., 1994. The role of organic matter in the formation of Colombian emeralds. European Journal of Mineralogy, 6, 4, 497-508.

Parkin, K. M., Loeffler, B. M., & Burns, R. G., 1977. Mössbauer spectra of kyanite, aquamarine, and cordierite showing intervalence charge transfer. Physics and Chemistry of Minerals, 1, 301-311.

Penner-Hahn, J. E., 2003. X-ray absorption spectroscopy. Journal of Synchrotron Radiation, 2, 13,159-182.

Platonov, A. N., Taran, M. N., & Polshin, E. V., 1979a. On the forms of iron in beryls. Zap Vses Miner Obsch 6, 725–730.

Platonov, A. N., Taran, M. N., Polshin, E. V., & Minko, O. E., 1979b. On nature of color of iron-bearing beryls. Izv AN SSR Ser Geol 10, 54–68.

Platonov, A. N., Khomenko, V. M., & Taran, M. N., 2016. Crystal chemistry, optical spectra and color of beryl. I. Heliodor and golden beryl — two varieties of natural yellow beryl. Mineralogical Journal, 38, 2, 3-14. https://doi.org/10.15407/mineraljournal.38.02.003.

Přikryl, J., Novák, M., Filip, J., Gadas, P., & Galiová, V., 2014. Iron + magnesium-bearing beryl from granitic pegmatites: An EMPA, LA-ICP-MS, Mössbauer spectroscopy, and powder XRD study. The Canadian Mineralogist, 52, 431-444.

Rehman, H. U., Martens, G., Tsai, Y.L., Chankhantha, C., Kidkhunthod, P., & Shen, A. H., 2020. An X-ray Absorption Near-Edge Structure (XANES) Study on the Oxidation State of Chromophores in Natural Kunzite Samples from Nuristan, Afghanistan. Minerals, 10, 5, 463. https://doi.org/10.3390/min10050463.

Rondeau, B., Fritsch, E., Peucat, J. J., Nordrum, F. S., & Groat, L., 2008. Characterization of emeralds from a historical deposit: Byrud (Eidsvoll), Norway. Gems & Gemology, 44, 2, 108-122.

Shang, Y., Guo, Y., & Tang, J., 2022. Spectroscopy and chromaticity characterization of yellow to light-blue iron-containing beryl. Scientific Reports, 12, 10765. https://doi.org/10.1038/s41598-022-11916-z.

Shigley, J. E., Thompson, T. J., & Keith, J. D., 2003. Red beryl from Utah: A review and update. Gems & Gemology, 39, 4, 302-313.

Spinolo, G., Fontana, I., & Galli, A., 2007. Optical absorption spectra of Fe^{2+} and Fe^{3+} in beryl crystals. Physica Status Solidi (b), 244, 12, 4660-4668. https://doi.org/10.1002/pssb.200743102.

Taran, M. N., & Rossman, G. R., 2001. Optical spectroscopic study of tuhualite and a re-examination of the beryl, cordierite, and osumilite spectra. American Mineralogist, 86, 9, 973-980.

Taran, M. N., Dyar, M. D., Khomenko, V. M., & Boesenberg, J. S., 2018. Spectroscopic study of synthetic hydrothermal Fe3±bearing beryl. Physics and Chemistry of Minerals, 45, 4, 489-496. https://doi.org/10.1007/s00269-017-0936-8.

Taran, M. N., & Vyshnevskyi, O. A., 2019. Be, Fe^{2+}-substitution in natural beryl: an optical absorption spectroscopy study12. Physics and Chemistry of Minerals, 46, 7, 795–806. https://doi.org/10.1007/s00269-019-01040-2.

U.S. Geologic Survey, 2021. Mineral commodities summaries: Beryllium, https://pubs.usgs.gov/periodicals/mcs2021/mcs2021-beryllium.pdf. 2 pp. Last accessed March 7, 2024.

Viana, R. R., da Costa, G. M., De Grave, E., Jordt-Evangelista, H., & Stern, W. B., 2002. Characterization of beryl (aquamarine variety) by Mössbauer spectroscopy. Physics and Chemistry of Minerals, 29, 1, 78-86. doi:10.1007/s002690100210.

Villain, O., Calas, G., Galoisy, L., Cormier, L., & Hazemann, J. L., 2007. XANES determination of chromium oxidation states in glasses: comparison with optical absorption spectroscopy. Journal of the American Ceramic Society, 90, 11, 3578-3581. https://doi.org/10.1111/j.1551-2916.2007.01905.x.

Wenk, H. R., Bulakh, A. G., 2004. Minerals: Their constitution and origin. Cambridge, Cambridge University Press.

Westre, T. E., Kennepohl, P., DeWitt, J. G., Hedman, B., Hodgson, K. O., & Solomon, E. I., 1997. A multiplet analysis of Fe K-Edge 1s → 3d pre-edge features of iron complexes. Journal of the American Chemical Society, 119, 27, 6297-6314. doi:10.1021/ja964352a.

Wilke, M., Farges, F., Petit, P.-E., Brown, G. E. Jr., & Martin, F., 2001. Oxidation state and coordination of Fe in minerals: An Fe K-XANES spectroscopic study. American Mineralogist, 86, 7-8, 714-730.

Wood, D. L., & Nassau, K., 1968. The characterization of beryl and emerald by visible and infrared absorption spectroscopy. The American Mineralogist, 53, 5-6, 777-800.

Zimmermann, J. L., Giuliani, G., Cheilletz, A., & Arboleda, C., 1997. Mineralogical significance of fluids in channels of Colombian emeralds: A mass-spectrometric study. International Geology Review, 39, 5, 425-437. doi:10.1080/00206819709465281.

FIGURES

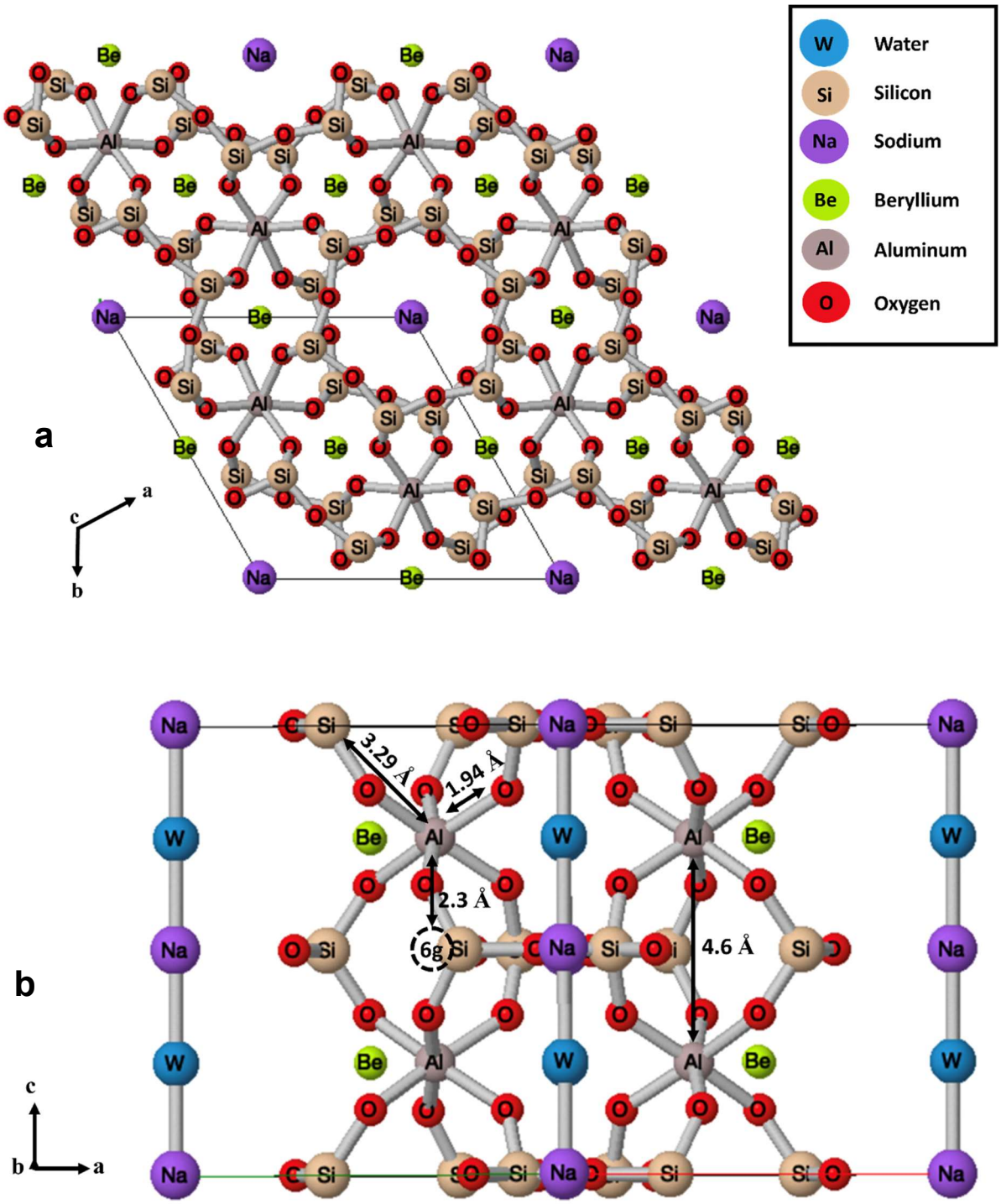

Figure 1. Atomic structure of beryl looking: (a) down the c axis perpendicular to the basal section and showing the 6-membered silicate rings forming channels that contain Na atoms (purple); and (b) down the b axis with the c axis vertical illustrating the 6g interstitial position between two octahedral Al sites along the c axis. Interatomic distances for Al-O (1.94Å), Al-6g (2.3 Å), Al-Si (3.29 Å), and Al-Al (4.6 Å) are

shown. Be (green) is shown in its tetrahedral and Al (brown) in its octahedral coordination. Water (W) molecules shown in blue. Images generated using www.Mindat.org.

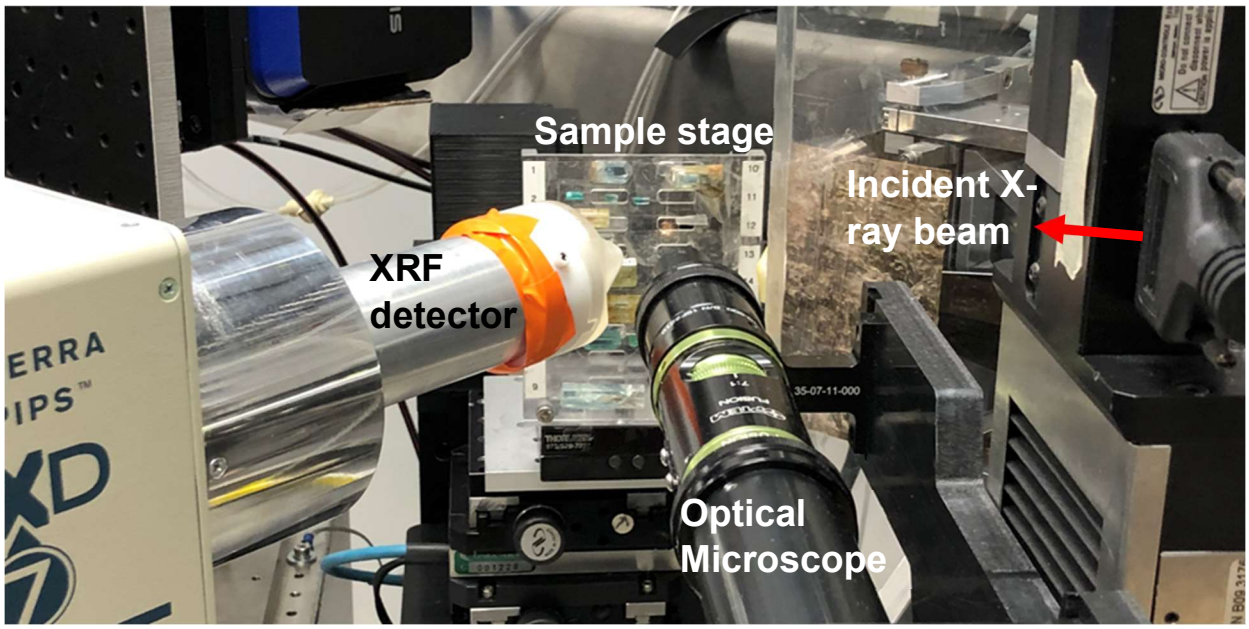

Figure 2. Sample stage setup for micro-XAS and micro-XRF experiments with the zoned emerald crystal oriented with its c axis horizontally and at 45° with respect to the propagation direction of the incident X-ray beam at the Advanced Photon Source synchrotron facility, beam line 13-IDE, Argonne National Lab, IL.

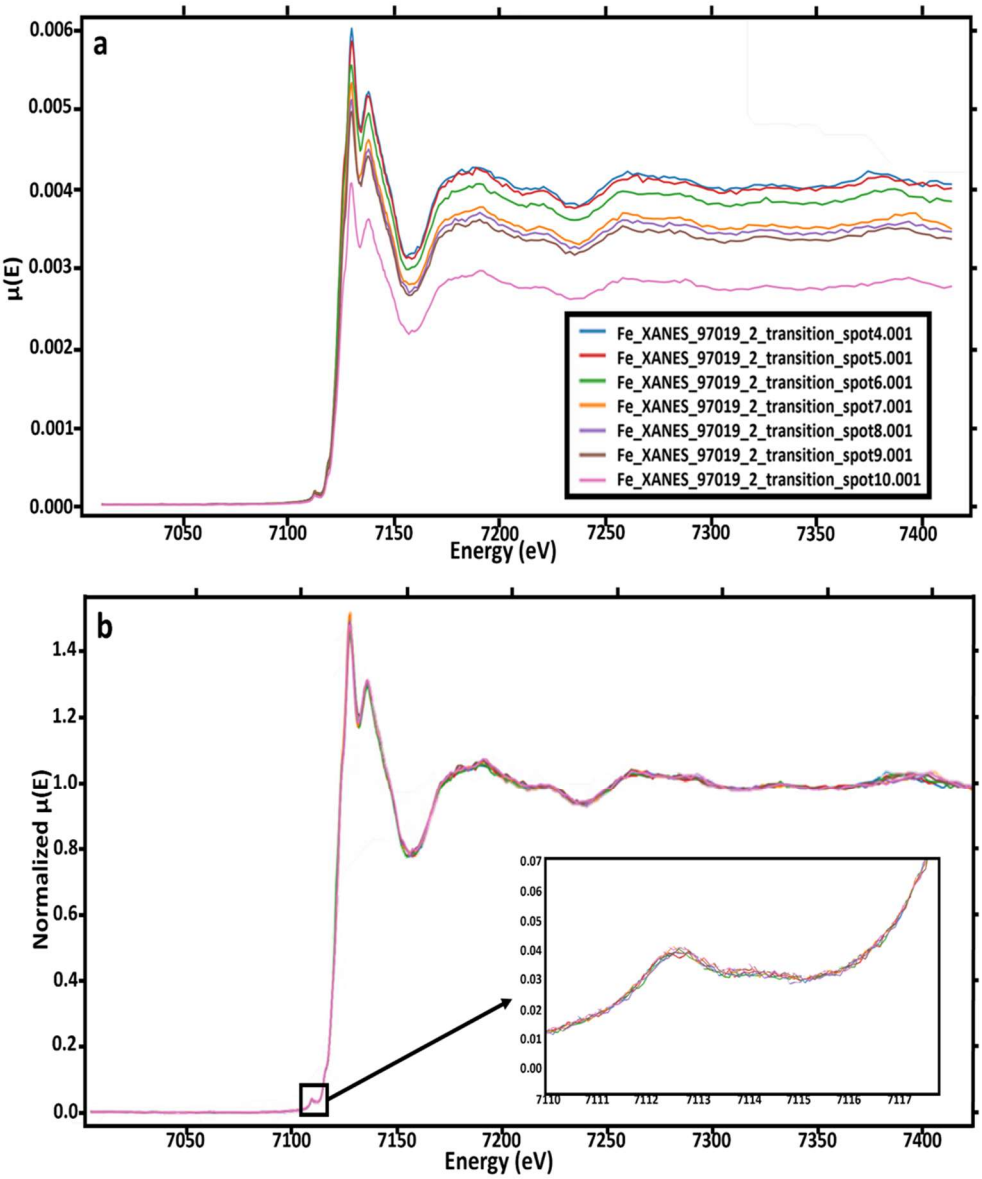

Figure 3. Synchrotron Fe K-edge X-ray absorption spectroscopy spectra for the 7 spot analyses in the zoned emerald crystal: **a.** Raw absorption coefficient, μ(E), *vs.* Energy (eV) in the full energy range of the spectrum. **b.** Normalized μ(E) *vs.* Energy (eV) in the full energy range of the spectrum and an inset with a zoomed-in view of the normalized pre-edge spectra showing two peaks. Green spots are analyses 4, 5, and 6; very light green spots are analyses 7, 8, 9, and 10. Sample 97019.2, Chivor, Colombia, from the Mineralogical and Geological Museum of Harvard University.

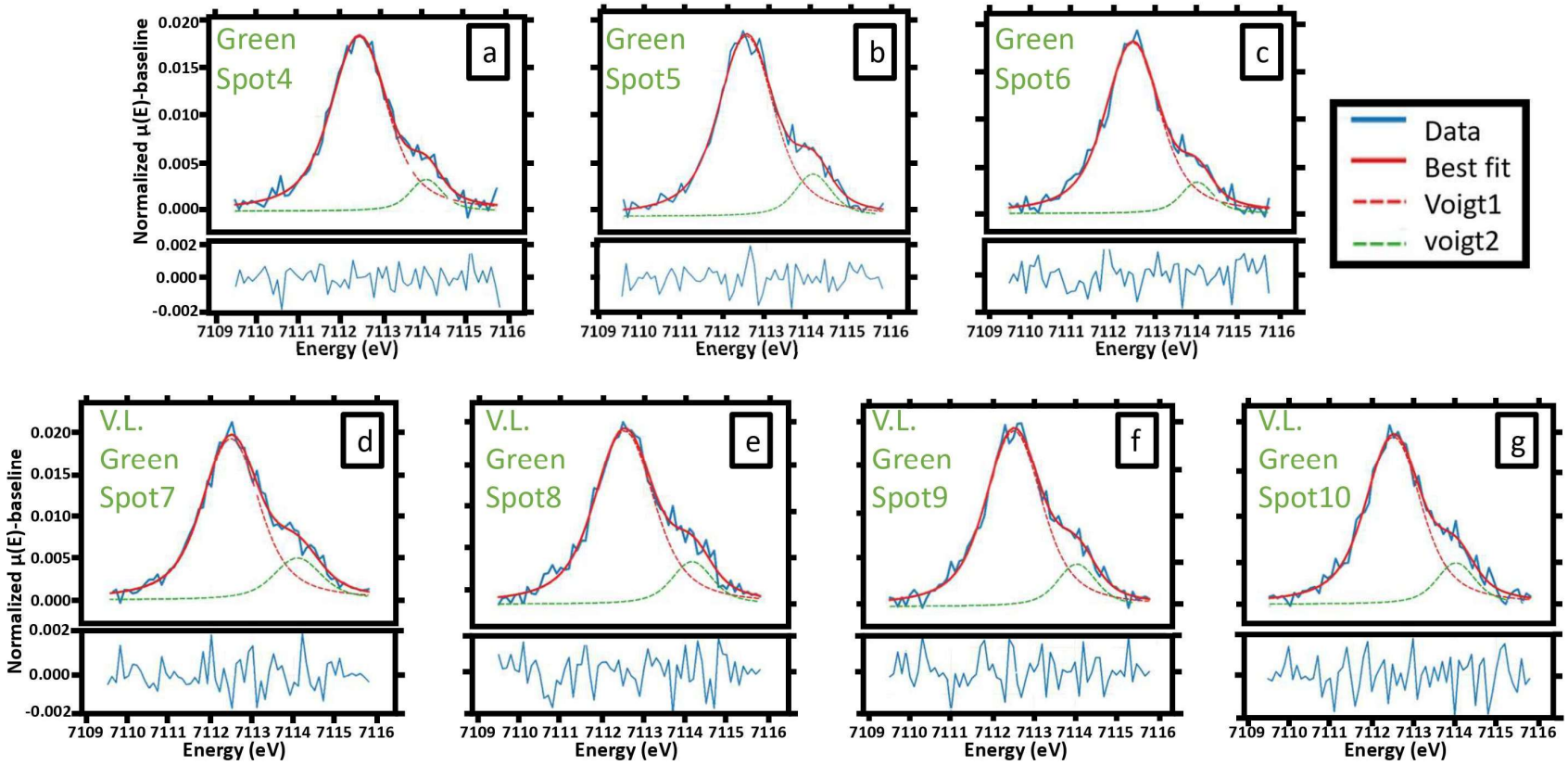

Figure 4. Graphs of unsmoothed normalized μ(E) with baseline subtracted *vs.* Energy (eV) for the seven Fe K-edge XAS pre-edge spot analyses in the zoned emerald crystal deconvoluted by two Voigt components showing the two pre-edge peaks. **a, b, and c** are green spots 4, 5, and 6, whereas **d, e, f, and g** are very light green spots 7, 8, 9, and 10. Each individual graph is accompanied by a corresponding plot of its residual, located right below. See text for analysis details.

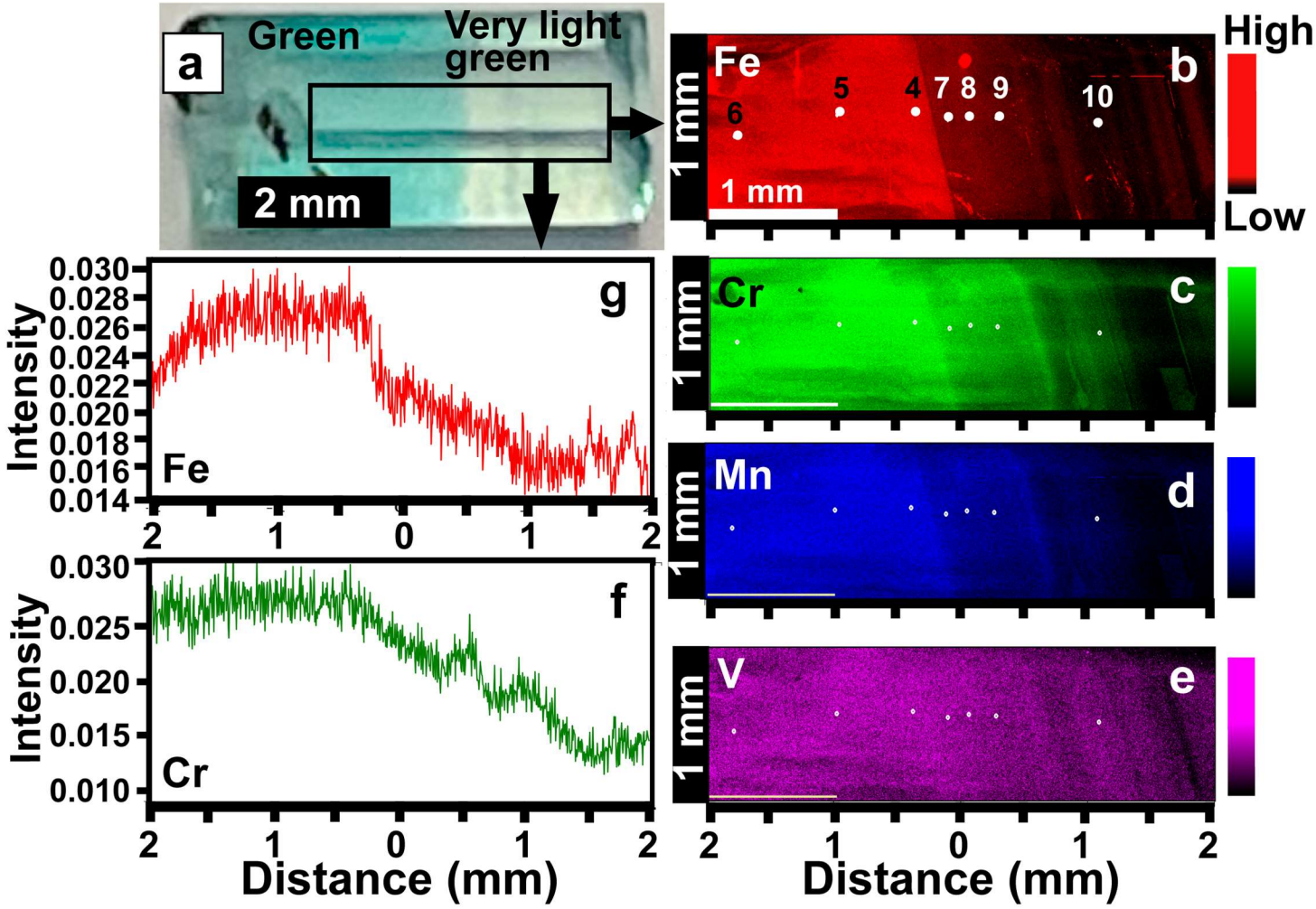

Figure 5. Synchrotron-based micro-XRF chemical maps of element intensity co-localization and cross sections of element intensity for the color zoned emerald crystal from Chivor, Colombia. **a.** Photograph of the emerald crystal showing the area analyzed enclosed by the rectangle. Chemical maps of element intensity for: **b.** Fe. **c.** Cr. **d.** Mn, and **e.** V. X-slices of distance (mm) *vs.* element intensity for: **f.** Cr and **g.** Fe. The rectangle in (a) corresponds to the areas mapped shown in b-e and the slices f and g. In (b), spots 4-6 correspond to spots analyzed in the green area and spots 7-10 correspond to those analyzed in the very light green area of the crystal. Color bars next to (b) – (e) shows per pixel signal intensity ranging from low (black) to medium to high (bright). Sample 97019.2, Mineralogical and Geological Museum, Harvard University.

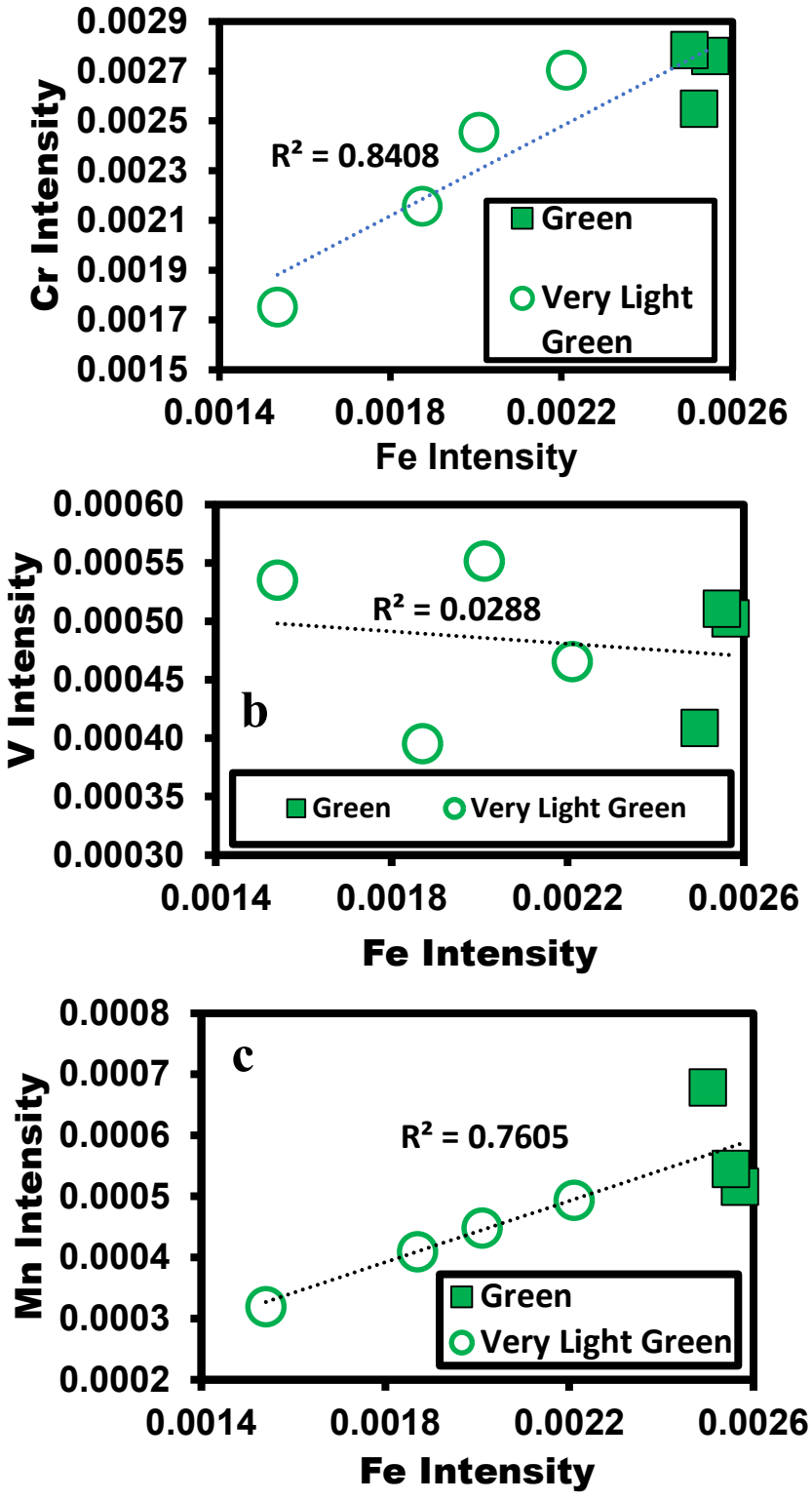

Figure 6. Binary plots of synchrotron micro-XRF elemental intensity (counts) for the zoned emerald crystal distinguishing the spots analyzed in the green area (green filled squares) from those in the very light green area (green open circles). **a.** Fe *vs.* Cr. **b.** Fe *vs.* V. **c.** Fe *vs.* Mn.

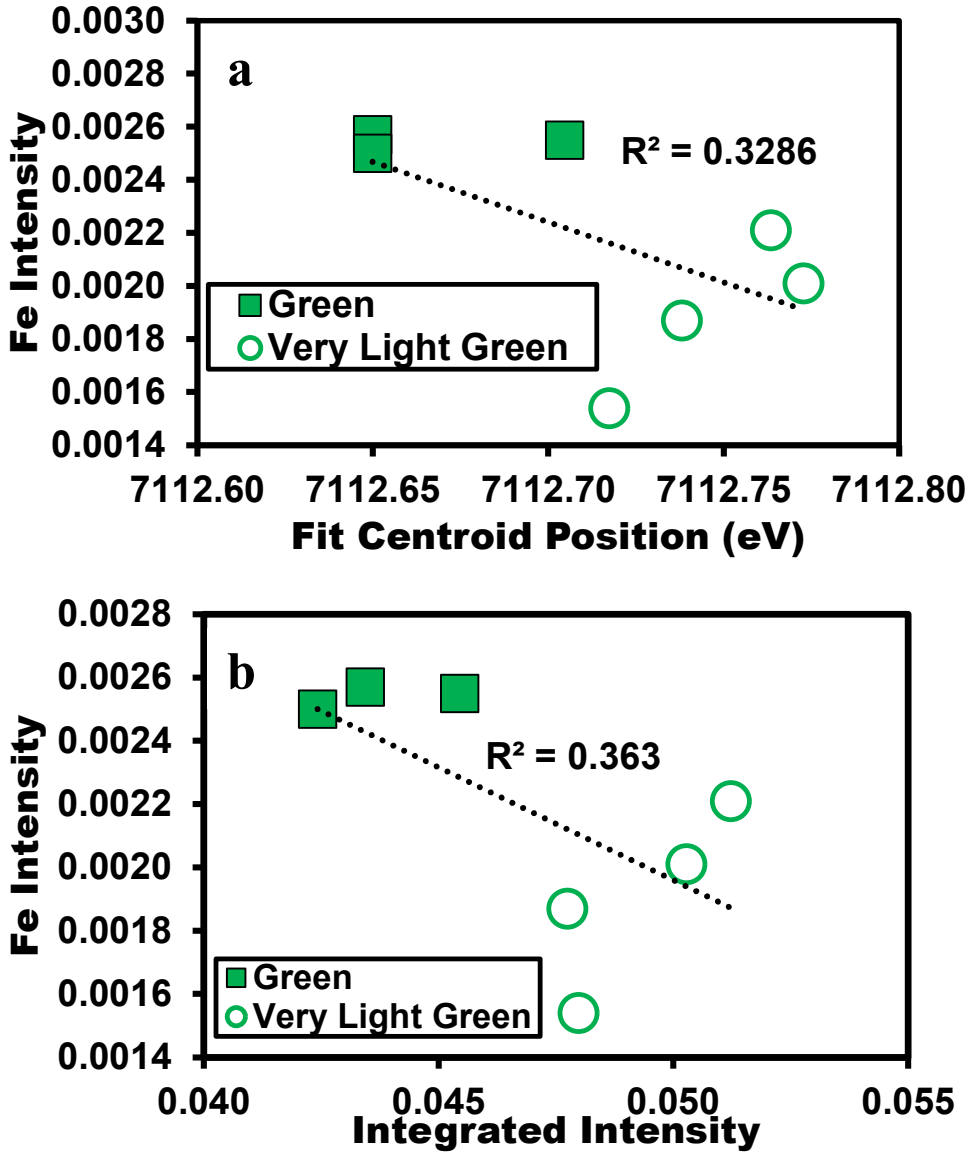

Figure 7. Binary plots of Fe K-edge pre-edge parameters for the zoned emerald crystal showing the green spots in green-filled squares and very light green spots in green open circles. **a.** Fit centroid energy position (eV) *vs.* Fe intensity. **b.** Integrated intensity (a.u.) *vs.* Fe intensity (counts).

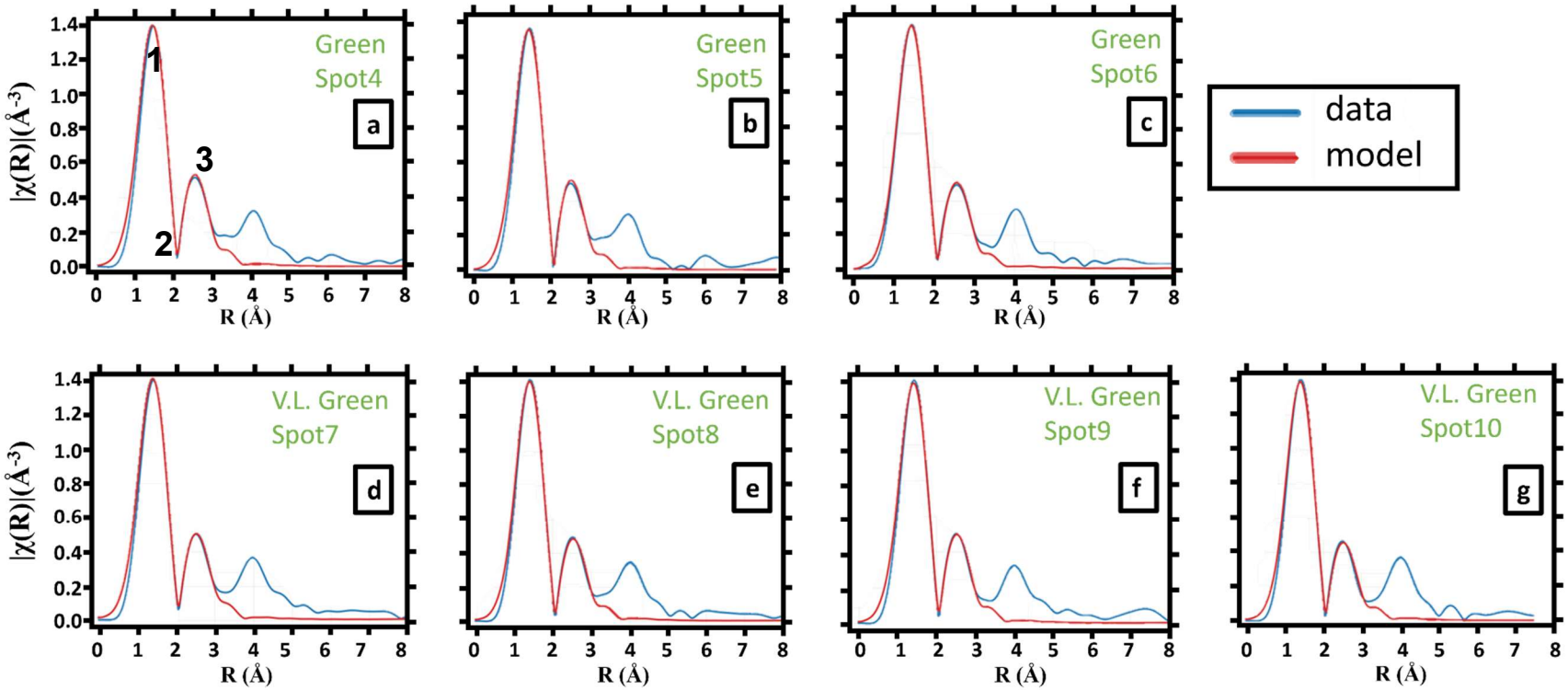

Figure 8. Graphs of R (Å) *vs.* |χ(R)|(Å^{-3}) showing the results of the FEFF fitting for Fe EXAFS data of the zoned emerald crystal. **a, b, and c** are green spots 4, 5, and 6, respectively, and **d, e, f, and g** are very light green spots 7 to 10, respectively. Only the first large peak (1), a small second peak/shoulder to peak 1 (2), and a third peak (3) were fitted

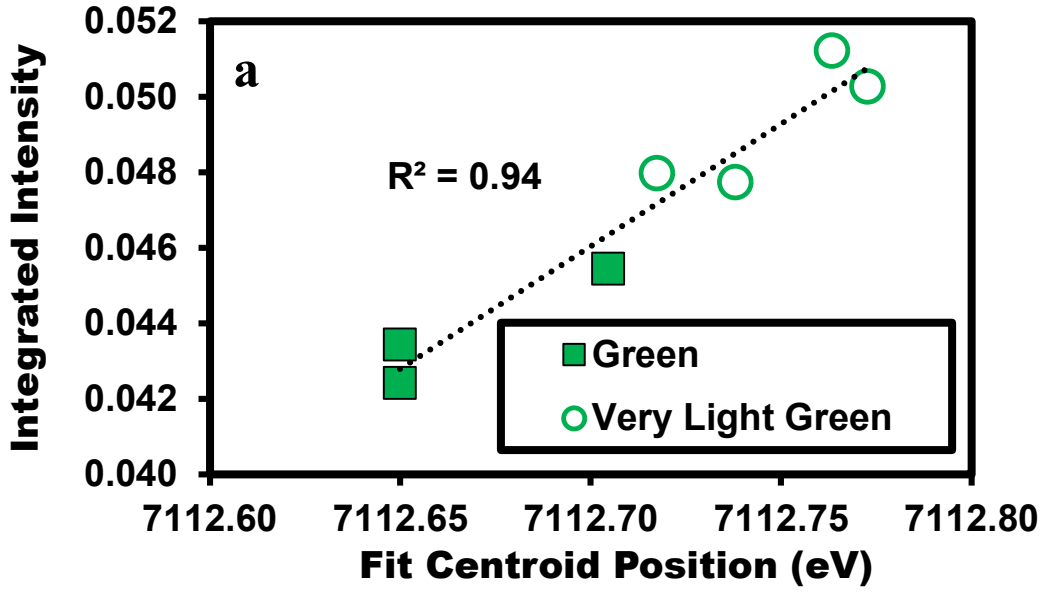
a
0.052
0.050
0.048
0.046
0.044
0.042
0.040
Integrated Intensity
R² = 0.94
Green
Very Light Green
7112.60
7112.65
7112.70
7112.75
7112.80
Fit Centroid Position (eV)

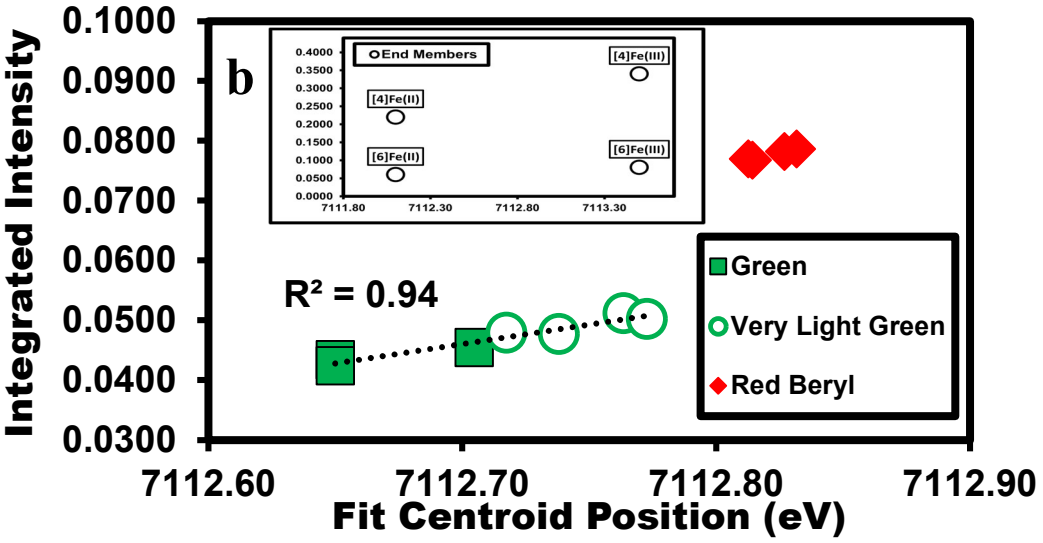
b
0.1000
0.0900
0.0800
0.0700
0.0600
0.0500
0.0400
0.0300
Integrated Intensity
End Members
[4]Fe(III)
[4]Fe(II)
[6]Fe(II)
[6]Fe(III)
R² = 0.94
Green
Very Light Green
Red Beryl
7112.60
7112.70
7112.80
7112.90
Fit Centroid Position (eV)

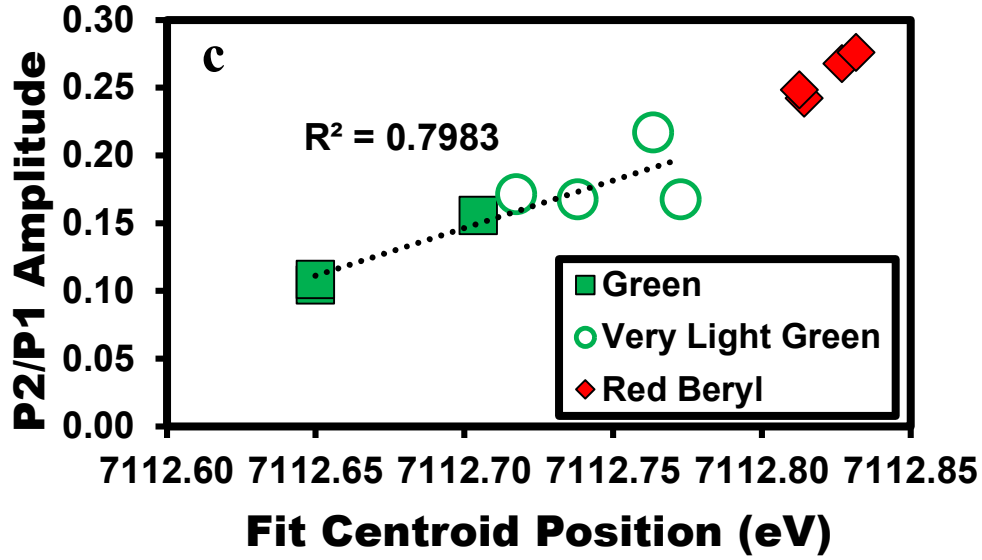

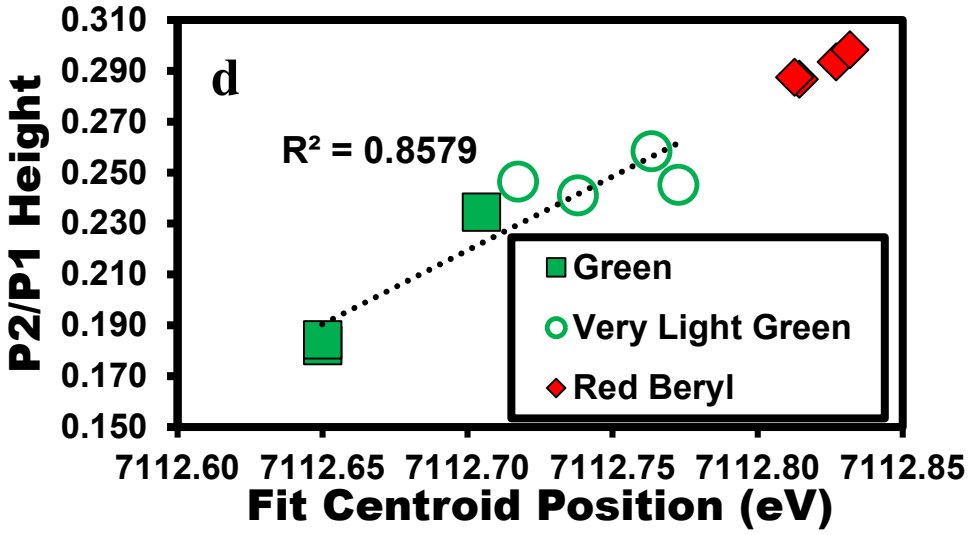

Figure 9. Binary plots of Fe K-edge pre-edge parameters for the zoned emerald. **a.** Pre-edge centroid position (eV) *vs.* integrated intensity. **b.** Pre-edge centroid position (eV) *vs.* integrated intensity for the zoned emerald compared to a red beryl crystal from the Wah Wah Mountains, Utah, USA. Sample, 131716, Geological and Mineralogical Museum, Harvard University. After Wilke et al. (2001). **c.** Pre-edge centroid position (eV) *vs.* P2/P1 Amplitude. **d.** Pre-edge centroid position (eV) *vs.* P2/P1 height. Inset shows the same graph with the end members of Wilke et al. (2001). Note different x axis scales.

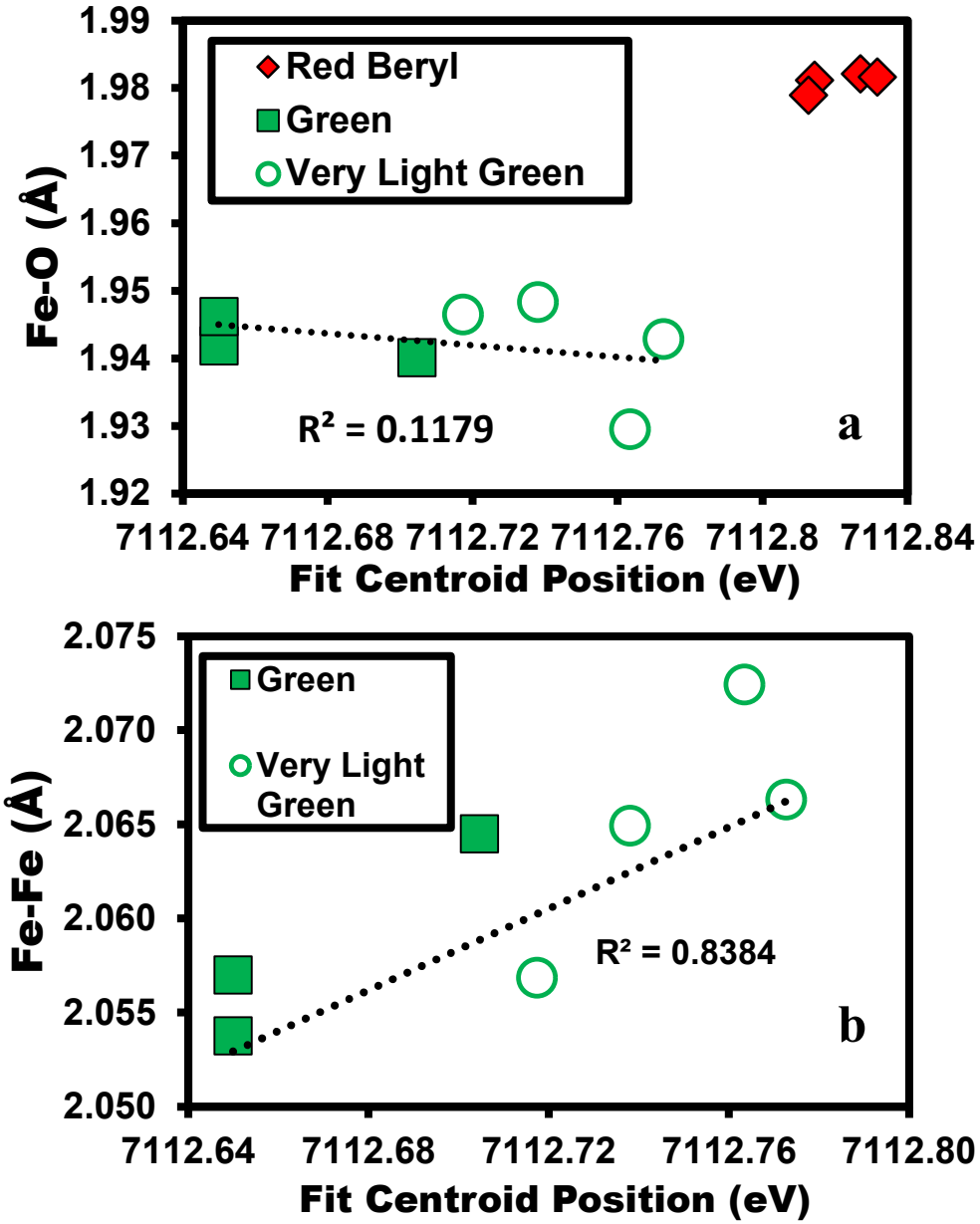

Figure 10. Graphs of pre-edge centroid position (eV) *vs.* modeled bond distances obtained by EXAFS fitting. **a.** Centroid *vs.* Fe-O (Å) for the zoned emerald crystal from Chivor, Colombia, and the red beryl from Utah, USA. **b.** Centroid *vs.* Fe-Fe distance (Å) fitting for the zoned emerald crystal from Chivor, Colombia.

TABLES

Table 1. Color, elemental intensities, and Cr/V ratios obtained by synchrotron micro-XRF for the zoned emerald crystal.

Analysis I.D.	Color	Intensity (counts)				
		Fe	Cr	V	Mn	Cr/V
Spot 4	Green	0.00257	0.002550	0.0005026	0.0005165	5.1
Spot 5		0.00255	0.002762	0.0005109	0.0005456	5.4
Spot 6		0.00250	0.002785	0.0004088	0.0006790	6.8
Spot 7	Very light green	0.00221	0.002704	0.0004657	0.0004936	5.8
Spot 8		0.00201	0.002455	0.0005517	0.0004482	4.4
Spot 9		0.00187	0.002158	0.0003955	0.0004094	5.5
Spot 10		0.00154	0.001752	0.0005352	0.0003197	3.3

Table 2. Values of parameters extracted from the Fe K-edge pre-edge fitting of the zoned emerald and red beryl crystals.*

Analysis I.D.	Color	P1 Center (eV)	P1 Amplitude	P1 Height	P2 Center (eV)	P2 Amplitude	P2 Height	Pre-edge Centroid (eV)	Integrated Intensity
Spot 4	Green	7112.4971	0.0393	0.0184	7114.1126	0.0041	0.0034	7112.6499	0.0434
Spot 5		7112.4853	0.0393	0.0186	7114.1114	0.0061	0.0044	7112.7046	0.0454
Spot 6		7112.4966	0.0383	0.0183	7114.0622	0.0042	0.0034	7112.6499	0.0424
Spot 7	Very Light Green	7112.4760	0.0421	0.0195	7114.0880	0.0091	0.0050	7112.7634	0.0512
Spot 8		7112.5380	0.0431	0.0191	7114.1711	0.0072	0.0047	7112.7727	0.0503
Spot 9		7112.5180	0.0409	0.0191	7114.0501	0.0069	0.0046	7112.7380	0.0477
Spot 10		7112.4963	0.0410	0.0194	7114.0069	0.0070	0.0048	7112.7174	0.0480
Spot 1	Red Beryl	7112.5004	0.0618	0.0303	7114.1099	0.0150	0.0087	7112.8143	0.0767
Spot 2		7112.4879	0.0617	0.0303	7114.0930	0.0165	0.0089	7112.8269	0.0782
Spot 3		7112.4945	0.0616	0.0303	7114.0930	0.0153	0.0087	7112.8126	0.0770
Spot 4		7112.4845	0.0616	0.0304	7114.0897	0.0170	0.0091	7112.8317	0.0786

* P1 denotes the pre-edge peak located at lower energy, P2 denotes the pre-edge peak located at higher energy. Data (unsmoothed) fitted together by using an energy fit range of 7109.5 -7115.8 eV and a baseline skip range of 7110.0-7115.2 eV.

Table 3. Parameters obtained from EXAFS FEFF fitting for the zoned emerald and red beryl crystals.*

Peak	Path (bond)	Valence State	R (Å) model	R (Å) Green Zone	Avg. Green R (Å)	R (Å) V. Light Green	Avg. V. Light Green R (Å)	Avg. Zoned Emeral R (Å)	R (Å) Red Beryl	Avg. Red Beryl R (Å)	Interpretation for zoned emerald
1	**Fe-O**	Fe^{3+}	1.9416 [a]	1.9401-1.9462	**1.9428**	**1.9295-1.9483**	1.9418	**1.9422**	1.9789-1.9821	**1.9809**	$^{VI}Fe^{3+}$
2	**Fe-Fe**	Fe^{3+}-Fe^{2+}	2.3000 [b]	**2.0538**-2.0645	2.0584	2.0568-**2.0724**	2.0651	**2.0623**	2.5319-2.5383	2.5344	$^{VI}Fe^{2+}$-$^{6g}Fe^{3+}$
3	**Fe-Si**	Fe^{3+}	3.2979 [c]	3.2864-3.2988	3.2942	3.2964-3.3072	3.3029	**3.2992**	3.3458-3.3515	3.3496	$^{VI}Fe^{3+}$

***** Peak number refers to peaks in Fig. 8 from left to right. [a – c] Model R (Å) values for Fe-O, ^{VI}Fe-Fe^{6g}, and Fe-Si are from Groat et al. (2010). In **bold** are bond distances discussed in the text. See text for further details.

Table 4. Bond distances (Å) for Fe of different coordination in the crystal structure of beryl of different colors taken from the literature.

Color	Bond Length (Å) and Coordination Number (CN)									References
	Fe^{3+}-O CN = 6	**Fe^{3+}-O CN = 4**	**Fe^{2+}-O CN = 6**	**Fe^{2+}-O CN = 4**	**6g-O CN = 6**	**Al-O CN = 6**	**Fe-Fe**	**Al-6g**	**4d-O**	
Beryl	**2.016**	1.870	**2.154**	**1.968**	**2.161**	Avg. **1.925**	2.604	**2.300**	1.870-1.891	Bačík & Fridrichová (2019), Lin et al. (2013)
Green beryl			1.95 (avg.)			**1.904-1.955**				Faye (1972), Gibbs et al. (1968), Goldman et al. (1978)
Blue Beryl	1.9416-2.025		2.125-2.304		2.125-2.304	1.955	2.3-2.608	2.49-2.51	1.891	Lin et al. (2013), Groat et al. (2010)
Red Beryl	1.9166		1.920			1.916				Fridrichová et al. (2017), Gatta et al. (2022)

Bold indicate bond distances discussed in the text.

Table 5. Comparison of average Fe-O R values (Å) for the zoned emerald and red beryl obtained by FEFF fitting with those from the literature.

	This Study	**Other Studies**									
	EXAFS	Bâcik & Fridrichova (2019)								Lin et al. (2013)	
Beryl Color	**Fe-O (Å) Average**	**$^{IV}Fe^{2+}$-O**	**$\Delta_{Meas-Lit}$**	**$^{VI}Fe^{3+}$-O**	**$\Delta_{Meas-Lit}$**	**$^{IV}Fe^{3+}$-O**	**$\Delta_{Meas-Lit}$**	**$^{VI}Fe^{2+}$-O**	**$\Delta_{Meas-Lit}$**	**^{VI}Fe-O**	**$\Delta_{Meas-Lit}$**
Zoned emerald	1.9422	1.968	0.025764	2.016	0.073764	1.87	0.072236	2.154	0.211764	1.99	0.047764
Red beryl	1.98099	1.968	0.012995	2.016	0.035005	1.87	0.110995	2.154	0.173005	1.99	0.009005

Meas = measured. Lit = Literature. See text for details.

Table 6. Details of existing synchrotron radiation Fe (and Cr) K-edge XAS synchrotron spectroscopy studies of green beryl and emerald.

Element	Color	Study (Ref.)	Major Findings	Method of Data Analysis (References)
Fe	Light Green to Medium Yellowish Green	XANES (+UV-Vis-NIR) (Chankhantha et al., 2016)	Octahedral Fe^{3+} (changed to Fe^{2+} by heating) Fe^{2+} also present (seen in UV-Vis-NIR) (octahedral or channel) Green beryl edge overlaps Fe_2O_3 reference (E_0 at 7125 eV); heated, reduction changed it to blue, spectra shifted to lower E_0 matching reference FeO (at 7120 eV)	Comparison with FeO (Fe^{2+}) and Fe_2O_3 (Fe^{3+}) standard edge positions. Edge-step normalization of data used a linear pre-edge subtraction and regression of a quadratic polynomial beyond the edge. No analysis of pre-edge peaks Pre-edge peaks not studied
Fe	Green	XANES (Eeckhout et al., 2005)	Confirmed presence of octahedral Fe^{3+} in green beryl Green beryl pre-edge peaks centers at 7113.82 eV and 7115.41 eV	Normalization and background subtraction performed using the WinXAS97 program Pre-edge deconvoluted into pseudo-Voigt components to derive the normalized height and position (Wilke et al., 2001)
Fe	Light Blue to Blueish Green	XANES (+UV-Vis, NIR) (Bunnag et al., 2020)	Absorption edge positions and pre-edge centroid energy positions confirmed the presence of Fe^{3+} and Fe^{2+} in the blueish-green sample Pre-edge analysis indicated predominantly 6-fold coordinated Fe	Pre-edge parameters integrated intensity and centroid energy positions of aquamarine compared with oxide standards (Wilke et al., 2001) Samples graphed with parameters for Fe speciesFe^{2+}[4], Fe^{3+}[4], Fe^{2+}[6], and Fe^{3+}[6] of Wilke et al. (2001). [4] and [6] = 4-fold and 6-fold coordination, respectively
Cr	Green	EXAFS and XANES (Gaudry et al., 2007)	Beryl: Al-O (1.90 Å), Al-Be (2.66 Å), Al-Si (3.26 Å) Emerald: Cr-O (1.97 Å), Cr-Be (2.70 Å), Cr-Si (3.31) Pre-edge feature occurring at 5998.5 eV	Pre-edge background removed using a polynomial fit to the pre-edge data and extrapolated into the post-edge region. Data normalization and energy shift performed using a step function and a pseudo-Voigt peak function. Energy scale converted to reciprocal space units (Koningsberger & Prins, 1988)

				EXAFS fitting performed using a program to process the EXAFS data with theoretical phases, amplitudes, and mean free paths calculated with a real space multiple scattering approach in the FEFF8 code

Table 7. Substitution mechanisms for Fe (and Cr, V, Mn) in emerald and green, yellow, blue, colorless, and red beryl.

Ion	Coordination/Site	Mechanism	Color, Notes	References
Cr^{3+} ±Fe^{3+}	Octahedral Al	Dispersed Cr (> 12 ppm/0.1%) ions e^- transitions; Absorption of violet-blue, orange, yellow & red wavelength	Dark Green Beryl (Emerald)	Wood & Nassau 1968, Loeffler & Burns 1976, Fritsch & Rossman 1988, Přikryl et al. 2014, Hu & Lu 2019
V^{3+} ±Fe^{3+}	Octahedral Al	Dispersed V ions; Absorption of violet to blue wavelength	Green (Vanadium Emerald) and Yellowish Green	Wood & Nassau 1968, Fritsch & Rossman 1988, Hu & Lu 2019
Fe^{3+} and Fe^{2+}	Octahedral and Octahedral or Channel	Not discussed	Light Green to Medium Yellowish Beryl	Chankhantha et al. 2016
V^{3+} or Fe^{3+}+ Fe^{2+}	Octahedral Octahedral, Channel	V^{3+} or Yellow from $^{VI}Fe^{3+}$ + Blue from $^{CH}Fe^{2+}$	Light to Medium Green	Goldman et al. 1978, Chankhantha et al. 2016
Fe^{3+} and Fe^{2+}	Octahedral and Channel	Oxygen-Metal Charge Transfer (O^{2-}→Fe^{3+})	Green Beryl	Wood & Nassau 1968, Fritsch & Rossman 1988
Fe^{3+} and Fe^{2+}	Octahedral, minor Channel or Interstitial and Octahedral and Tetrahedral Be or Channel	IVCT and UVCT transitions	Pale Green Beryl	Mathew et al. 2000
Fe^{3+} and **Fe^{2+}**	Octahedral	UVCT + Yellow color center	Green Beryl	Spinolo et al. 2007
Fe^{3+} and Fe^{2+}	Octahedral and Tetrahedral		Green Beryl - constant $^{VI}Fe^{3+}$, variable $^{IV}Fe^{2+}$	Přikryl et al. 2014
Fe^{3+} Fe^{2+}-Fe^{3+}	Octahedral, Tetrahedral-Octahedral	IVCT + UVCT	Pale Greenish Yellow to Orange Beryl	Platonov et al. 2016
Fe^{2+}, **Fe^{3+}**	Octahedral Octahedral	O^{2-}→Fe^{3+} CT (Absorption of blue)	Golden Yellow to Brown (Heliodor)	Wood & Nassau 1968, 1969, Nassau 1999

Fe^{2+} and **Fe^{3+}**	Octahedral and Channel	UVCT	Golden Yellow	Goldman et al. 1978
Fe^{3+}	Octahedral	O^{2-}→Fe^{3+} CT absorption in violet	Yellow	Wood & Nassau 1968, Loeffle & Burns 1976, Chankhantha et al. 2016
Fe^{3+}+ Fe^{2+} and Fe^{3+}	Octahedral and Tetrahedral		Yellow, Yellowish Green	Samoilovich et al. 1971
Fe^{3+} Fe^{2+}-Fe^{3+}	Octahedral, Tetrahedral-Octahedral	UVCT + Yellow color center	Golden Beryl	Platonov et al. 2016
Fe^{3+} and Fe^{2+}	Octahedral		Green and Blueish Green	Goldman et al. 1978, Rossman 1981
Fe^{2+} or Fe^{2+}-Fe^{3+} and Fe^{3+}	NR	Higher Fe and higher Fe^{2+} or Fe^{2+}-Fe^{3+} pairs	Pale Greenish Blue, medium Blue, and dark Blue beryl	Hu & Lu 2020
Fe^{3+} and Fe^{2+}	Octahedral and Channel	UVCT - Relative % of $^{VI}Fe^{3+}$-O and $^{CH}Fe^{2+}$-O	Aquamarine – dark Blue to Greenish Blue Greener w/more $^{VI}Fe^{3+}$ or less $^{CH}Fe^{2+}$; Blue - $^{CH}Fe^{2+}$ Deep Blue little Fe^{3+}	Viana et al. 2002
Fe^{2+}	Channel (site B)		Blue Beryl	Wood & Nassau 1968, Price et al. 1976, Goldman et al. 1978, Chankhantha et al. 2016
Fe^{2+} and Fe^{2+}-Fe^{3+}	**Octahedral and Octahedral-Interstitial 6g or Octahedral-Octahedral**	**$^{VI}Fe^{2+}$ and Fe pairs IVCT transitions. Absorption of yellow, orange**	**Pale blue, blue, darker blue with more Fe^{3+}** and IVCT (Reduction of Fe^{3+} → Fe^{2+} changes Yellow to Blue) More Fe^{3+} - Green	Dvir & Low 1960, Wood & Nassau 1968, Loeffle & Burns 1976, Parkin et al. 1977, Goldman et al. 1978, Platonov et al. 1979, Taran & Rossman 2001, Spinolo et al. 2007, Groat et al. 2010, Lin et al. 2013, Taran & Vyshnevskyi 2022
Fe^{2+}	Octahedral	d-d Transitions	Light Blue	Taran et al. 2018
Fe^{2+}- Fe^{3+}	Octahedral	IVCT	Darker Blue	
Fe^{2+} and Fe^{3+}	Octahedral and Interstitial 4d/Channel and Octahedral/Interstitial	IVCT; Absorption in the red	Deep Blue (non-Maxixe)	Loeffle & Burns 1976, Parkin et al. 1977, Goldman et al. 1978
Fe^{2+}, Fe^{3+}, ±Fe^{2+}	**Octahedral, 6g Tetrahedral (Be)**	**$^{VI}Fe^{2+}$-$^{6g}Fe^{3+}$ IVCT**	Blue Beryl	Taran & Vyshnevskyi 2022

Fe^{2+}	**Channel (site A)**	Crystal field absorption	**Colorless (Goshenite), different colors** (no direct coloring effect)	Wood & Nassau 1968, Nassau 1999, Mathew et al. 2000
Fe^{2+}	**Octahedral**	Crystal field absorption	" "	Wood & Nassau 1968
Fe^{3+}	**Tetrahedral**	Absorption in UV & violet (d-d transitions)	Colorless	Wood & Nassau 1968
Fe^{2+} and Fe^{3+}	Octahedral, Tetrahedral, and Channel; and Channel*	NA	Colorless	Mathew et al. 2000
Fe^{2+}	Tetrahedral	NA	Colorless	Andersson 2019
Mn^{3+} **(Fe^{3+})&**	Octahedral Al Octahedral		Red Beryl	Keith et al. 1993, Shigley & Foord 1984, Gatta et al. 2022, Fridrichová et al. 2018 Nassau & Wood 1968

Note: The incorporation of Fe^{2+} and Fe^{3+} in channel sites in beryl has been considered unlikely by several studies, but their presence in channel sites has been postulated based on spectroscopy alone by others (e.g., Wood & Nassau 1968, Goldman et al. 1978, Blak et al. 1982, Lehmann 1983, Viana et al. 2002, Spinolo et al. 2007, Bačík & Fridrichová 2019). Bold = most important color-causing ion and mechanisms. NA – not applicable; Fe is present but not at color-causing sites. NR – not reported; * Fe^{3+} in octahedral coordination would produce yellow color. & Fe^{3+} does not produce red color. e^- = electron. IVCT = Inter-Valence Charge Transfer. UVCT = Ultra-Violet Charge Transfer.

APPENDIX FIGURES

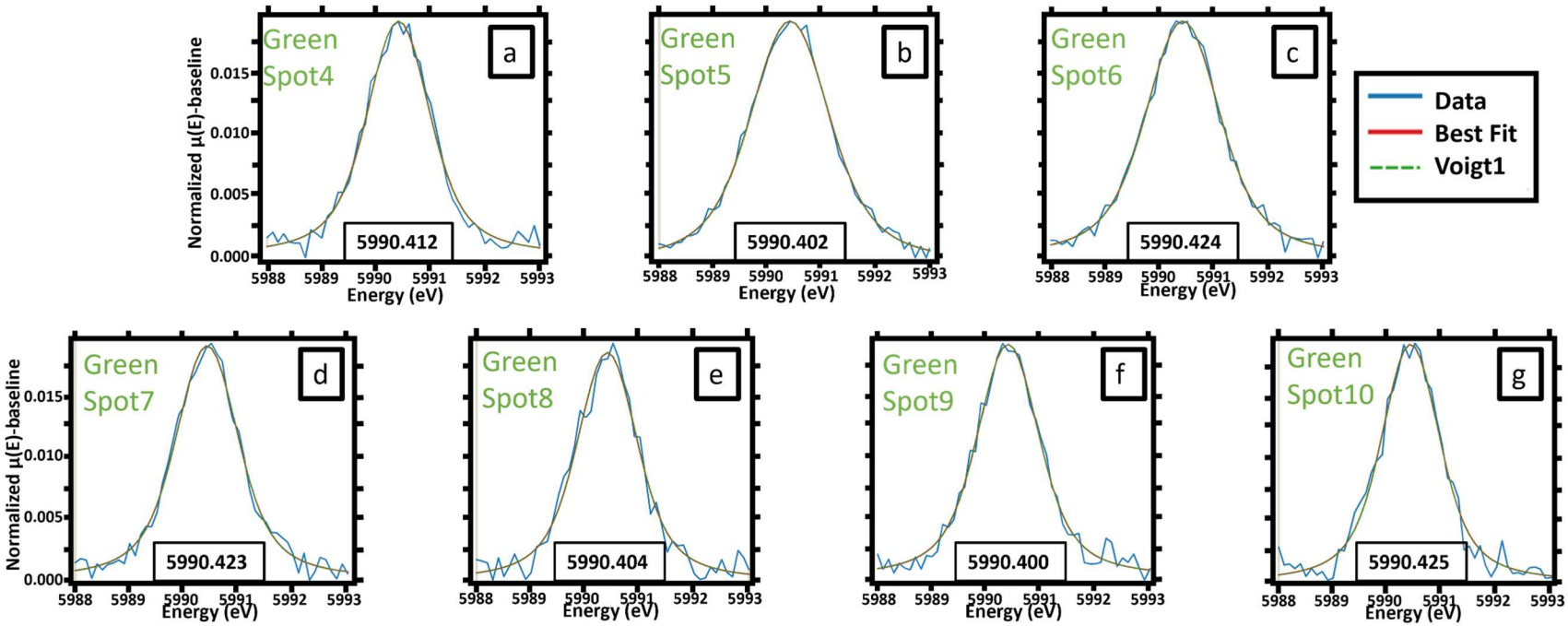

Figure A1. Graphs of normalized μ(E) with baseline subtracted *vs.* Energy (eV) for seven Cr XAS K-edge pre-edge analyses of the zoned emerald crystal deconvoluted by a Voigt component. Note a single peak in all analyses. Numbers inside graphs are Cr fit centroid position energy (eV). **a-g** show analysis spots 4 to 10.

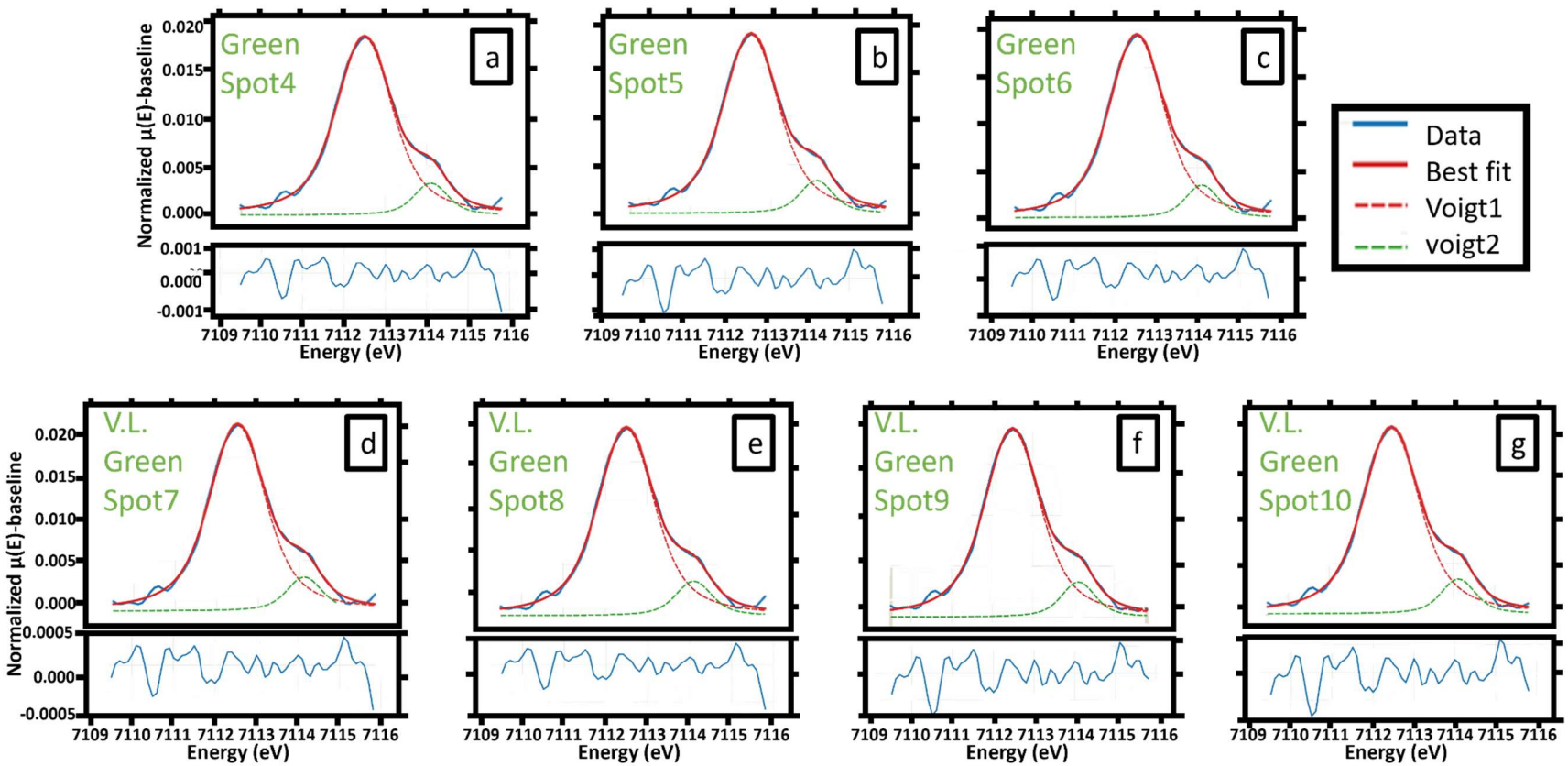

Figure A2. Graphs of smoothed normalized μ(E) with baseline-subtracted *vs.* Energy (eV) for the seven Fe K-edge XAS pre-edge spot analyses for the zoned emerald crystal deconvoluted by two Voigt components showing the two pre-edge peaks. **a, b, and c** are green spots 4, 5, and 6, and **d, e, f, and g** are very light green spots 7, 8, 9, and 10. Each individual graph is accompanied by a corresponding plot of its residual, located right below. Note different y scales in residual graphs. Data were fitted using a fit energy range of 7109.5-7115.8 and a baseline skip range of 7110.0-7115.2 eV.

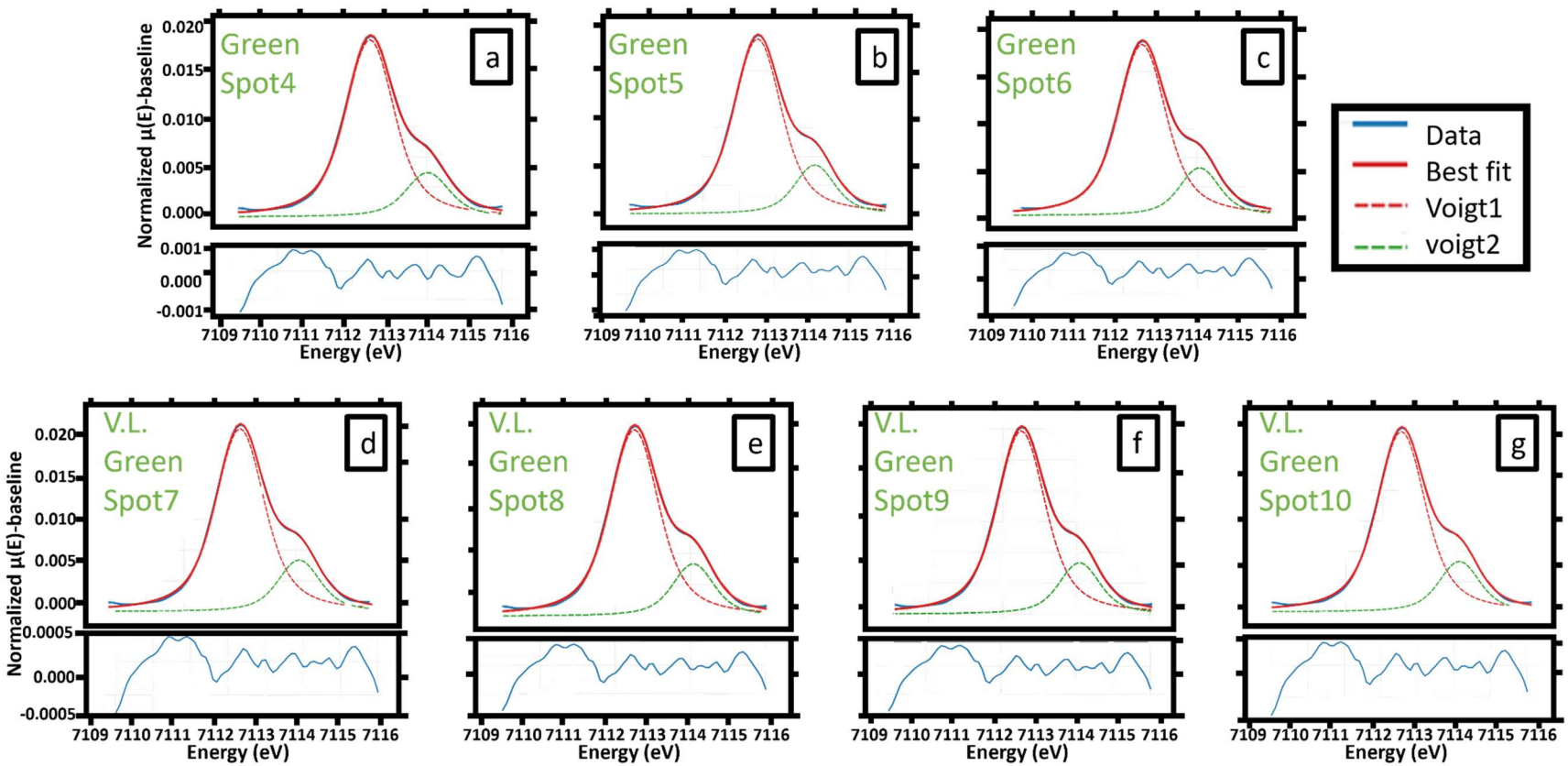

Figure A3. Graphs of normalized μ(E) with smoothed-baseline subtracted *vs.* Energy (eV) for the seven Fe K-edge XAS pre-edge spot analyses deconvoluted by two Voigt components for the zoned emerald showing the two pre-edge peaks. **a, b, and c** are green spots 4, 5, and 6, and **d, e, f, and g** are very light green spots 7, 8, 9, and 10. Each individual graph is accompanied by a corresponding plot of its residual, located right below. Note different y scales in residual graphs. Data were fitted using a fit energy range of 7109.0-7116.0 eV and a baseline skip range of 7110.2-7115.2 eV for all spots together.

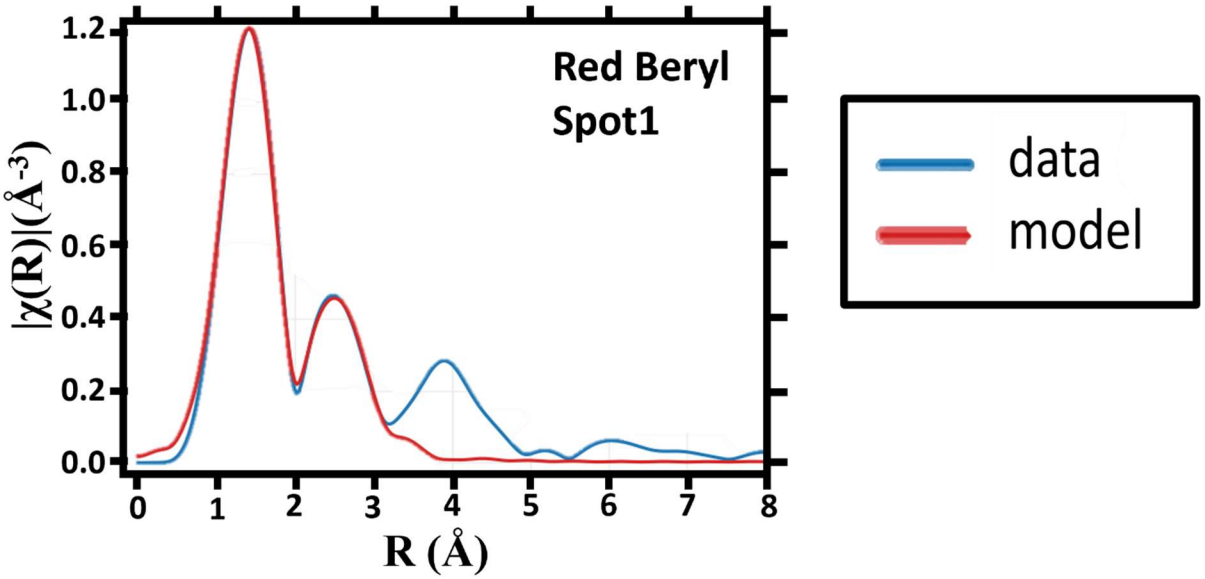

Figure A4. Graph of R (Å) *vs.* $|\chi(R)|(Å^{-3})$ showing the results of the FEFF fitting for Fe K-edge EXAFS data from a representative analysis of the red beryl crystal. Sample 131716, Geological and Mineralogical Museum of Harvard University.

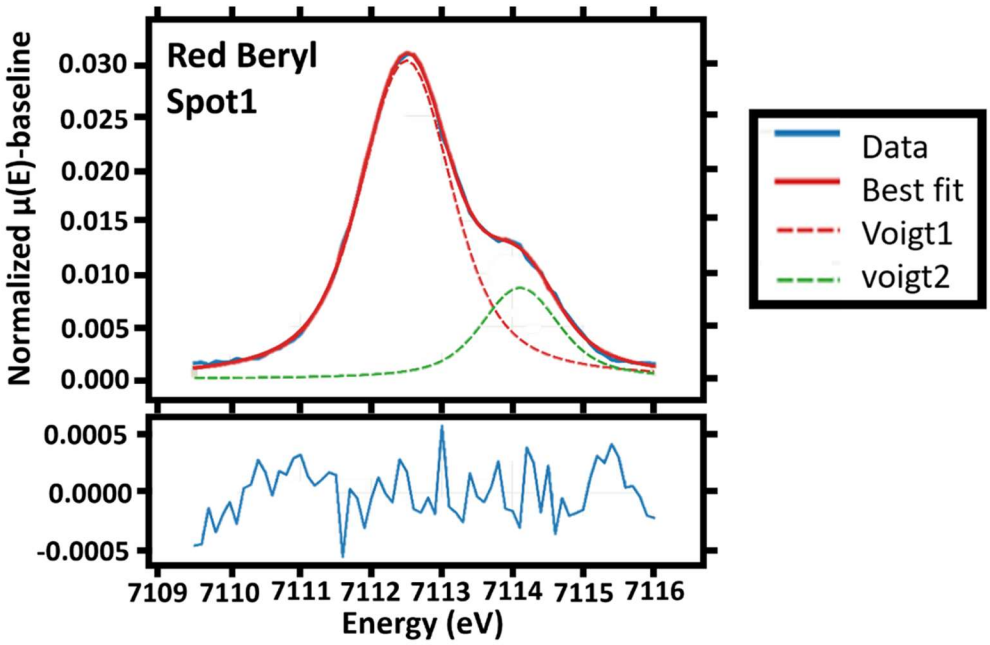

Figure A5. Representative graph of unsmoothed normalized μ(E) with baseline subtracted *vs.* Energy (eV) for the red beryl from Utah (spot 1). Fe K-edge XAS pre-edge deconvoluted by two Voigt components showing the two pre-edge peaks. Fitting graph is accompanied by a corresponding plot of its residual, located right below. See text for analysis details.

FIGURE CAPTIONS

Figure 1. Atomic structure of beryl looking down: **a.** the c axis of the basal plane and showing the 6-membered silicate rings forming channels. **b.** the b axis illustrating the 6g interstitial position between two octahedral Al sites along the c axis. Be (green) and Si (light tan) are shown in their tetrahedral site and Al (brown) in its octahedral coordination. Water (W) molecules (blue) and Na (purple) are shown in the channels. Images generated in Mindat.org.

Figure 2. Sample stage setup for micro-XAS and micro-XRF experiments with the zoned emerald crystal oriented with its c axis horizontally and at 45° with respect to the propagation direction of the incident X-ray beam at the Advanced Photon Source synchrotron facility, beam line 13-IDE, Argonne National Lab, IL.

Figure 3. Synchrotron Fe K-edge X-ray absorption spectroscopy spectra for the 7 spot analyses in the zoned emerald crystal: **a.** Raw absorption coefficient, μ(E), *vs.* Energy (eV) in the full energy range of the spectrum. **b.** Normalized μ(E) *vs.* Energy (eV) in the full energy range of the spectrum and an inset with a zoomed-in view of the normalized pre-edge spectra showing two peaks. Green spots are analyses 4, 5, and 6; very light green spots are analyses 7, 8, 9, and 10. Sample 97019.2, Chivor, Colombia, from the Mineralogical and Geological Museum of Harvard University

Figure 4. Graphs of unsmoothed normalized μ(E) with baseline subtracted *vs.* Energy (eV) for the seven Fe K-edge XAS pre-edge spot analyses in the zoned emerald crystal deconvoluted by two Voigt components showing the two pre-edge peaks. **a, b, and c** are green spots 4, 5, and 6, whereas **d, e, f, and g** are very light green spots 7, 8, 9, and 10. Each individual graph is accompanied by a corresponding plot of its residual, located right below. See text for analysis details.

Figure 5. Synchrotron-based micro-XRF chemical maps of element intensity co-localization and cross sections of element intensity for the color zoned emerald crystal from Chivor, Colombia. **a.** Photograph of the emerald crystal showing the area analyzed enclosed by the rectangle. Chemical maps of element intensity for: **b.** Fe. **c.** Cr. **d.** Mn, and **e.** V. X-slices of distance (mm) *vs.* element intensity for: **f.** Cr and **g.** Fe. The rectangle in (a) corresponds to the areas mapped shown in b-e and the slices f and g. In (b), spots 4-6 correspond to spots analyzed in the green area and spots 7-10 correspond to those analyzed in the very light green area of the crystal. Color bars next to (b) – (e) shows per pixel signal intensity ranging from low (black) to medium to high (bright). Sample 97019.2, Mineralogical and Geological Museum, Harvard University.

Figure 6. Binary plots of synchrotron micro-XRF elemental intensity (counts) for the zoned emerald crystal distinguishing the spots analyzed in the green area (green filled squares) from those in the very light green area (green open circles). **a.** Fe *vs.* Cr. **b.** Fe *vs.* V. **c.** Fe *vs.* Mn.

Figure 7. Binary plots of Fe K-edge pre-edge parameters for the zoned emerald crystal showing the green spots in green-filled squares and very light green spots in green open circles. a. Fit centroid energy position (eV) *vs.* Fe intensity. b. Integrated intensity (a.u.) *vs.* Fe intensity (counts).

Figure 8. Graphs of R (Å) *vs.* $|\chi(R)|(Å^{-3})$ showing the results of the FEFF fitting for Fe EXAFS data of the zoned emerald crystal. **a, b, and c** are green spots 4, 5, and 6, respectively, and **d, e, f, and g** are very light green spots 7 to 10, respectively. Only the first large peak (1), a small second peak/shoulder to peak 1 (2), and a third peak (3) were fitted.

Figure 9. Binary plots of Fe K-edge pre-edge parameters for the zoned emerald. **a.** Pre-edge centroid position (eV) *vs.* integrated intensity. **b.** Pre-edge centroid position (eV) *vs.* integrated intensity for the zoned emerald compared to a red beryl crystal from the Wah Wah Mountains,

Utah, USA. Sample, 131716, Geological and Mineralogical Museum, Harvard University. After Wilke et al. (2001). **c.** Pre-edge centroid position (eV) *vs.* P2/P1 Amplitude. **d.** Pre-edge centroid position (eV) *vs.* P2/P1 height. Inset shows the same graph with the end members of Wilke et al. (2001).

Figure 10. Graphs of pre-edge centroid position (eV) *vs.* modeled bond distances obtained by EXAFS fitting. **a.** Centroid *vs.* Fe-O (Å) for the zoned emerald crystal from Chivor, Colombia, and the red beryl from Utah, USA. **b.** Centroid *vs.* Fe-Fe distance (Å) fitting for the zoned emerald crystal from Chivor, Colombia.

TABLE HEADINGS

Table 1. Color, elemental intensities, and Cr/V ratios obtained by synchrotron micro-XRF for the zoned emerald crystal.

Table 2. Values of parameters extracted from the Fe K-edge pre-edge fitting of the zoned emerald and red beryl crystals.

Table 3. Parameters obtained from EXAFS FEFF fitting for the zoned emerald and red beryl crystals.

Table 4. Bond distances (Å) for Fe of different coordination in the crystal structure of beryl of different colors taken from the literature.

Table 5. Comparison of Fe-O R values (Å) for the zoned emerald and red beryl obtained by FEFF fitting with those from the literature.

Table 6. Details of existing synchrotron radiation Fe (and Cr) K-edge XAS synchrotron spectroscopy studies of green beryl and emerald..

Table 7. Substitution mechanisms for Fe (and Cr, V, Mn) in emerald and green, yellow, blue, colorless, and red beryl.

.

APPENDIX FIGURES CAPTIONS

Figure A1. Graphs of normalized μ(E) with baseline subtracted *vs.* Energy (eV) for seven Cr XAS K-edge pre-edge analyses of the zoned emerald crystal deconvoluted by a Voigt component. Note a single peak in all analyses. Numbers inside graphs are Cr fit centroid position energy (eV). a-g show analysis spots 4 to 10.

Figure A2. Graphs of smoothed normalized μ(E) with baseline-subtracted *vs.* Energy (eV) for the seven Fe K-edge XAS pre-edge spot analyses for the zoned emerald crystal deconvoluted by two Voigt components showing the two pre-edge peaks. a, b, and c are green spots 4, 5, and 6, and d, e, f, and g are very light green spots 7, 8, 9, and 10. Each individual graph is accompanied by a corresponding plot of its residual, located right below. Note different y scales in residual graphs. Data were fitted using a fit energy range of 7109.5-7115.8 and a baseline skip range of 7110.0-7115.2 eV.

Figure A3. Graphs of normalized μ(E) with smoothed-baseline subtracted *vs.* Energy (eV) for the seven Fe K-edge XAS pre-edge spot analyses deconvoluted by two Voigt components for the zoned emerald showing the two pre-edge peaks. a, b, and c are green spots 4, 5, and 6, and d, e, f, and g are very light green spots 7, 8, 9, and 10. Each individual graph is accompanied by a corresponding plot of its residual, located right below. Note different y scales in residual graphs. Data were fitted using a fit energy range of 7109.0-7116.0 eV and a baseline skip range of 7110.2-7115.2 eV for all spots together.

Figure A4. Graph of R (Å) *vs.* |χ(R)|(Å-3) showing the results of the FEFF fitting for Fe K-edge EXAFS data from a representative analysis of the red beryl crystal. Sample 131716, Geological and Mineralogical Museum of Harvard University.

Figure A5. Representative graph of unsmoothed normalized μ(E) with baseline subtracted *vs.* Energy (eV) for the red beryl from Utah (spot 1). Fe K-edge XAS pre-edge deconvoluted by two Voigt components showing the two pre-edge peaks. Fitting graph is accompanied by a corresponding plot of its residual, located right below. See text for analysis details.

CHAPTER 2: SYNCHROTRON-BASED FE K-EDGE MICRO-XAS AND MICRO-XRF SPECTROSCOPY INVESTIGATION OF VARIATIONS IN ELEMENTAL CONTENT AND FE VALENCE STATE AND COORDINATION ENVIRONMENT WITH COLOR IN A ZONED AQUAMARINE CRYSTAL

ABSTRACT

The role of Fe in causing the blue color in the beryl variety aquamarine was previously investigated using spectroscopy techniques, but only 5 studies relied on synchrotron-based spectroscopy, although they are powerful techniques to determine elemental variations and the relative valence state and coordination environment of atoms. Previous spectroscopy studies of blue beryl proposed that the blue color of aquamarine is caused by intervalence charge transfer (IVCT) between Fe^{2+} in octahedral coordination and Fe^{3+} in the 6g interstitial site or Fe^{2+} in channel sites. Some studies investigated intra-crystal variations in blue color and the occurrence of Fe in atomic sites, but debate is ongoing. There has been only one study of aquamarine crystals by combined synchrotron X-ray absorption spectroscopy (XAS) using X-ray absorption-near edge structure (XANES) and extended X-ray absorption fine structure (EXAFS) and it evidenced IVCT involving $^{6g}Fe^{3+}$ and $^{VI}Fe^{2+}$. A detailed synchrotron-based XAS investigation of the atomic environment of Fe in aquamarine and its relationship with blue color variations has yet to be performed. In this study, combined synchrotron-based high-resolution Fe K-edge micro-XAS and micro-X-ray fluorescence (XRF) spectroscopy of a color-zoned aquamarine crystal from Minas Gerais, Brazil, is used to establish the relationship between Fe, Cr, Mn, and V content, Fe XAS pre-edge and EXAFS parameters indicative of average oxidation state and coordination environment of Fe, and blue color variation. Detailed micro-XRF chemical maps within four color zones of the aquamarine crystal reveal delicate (1 mm) chemical zoning in Fe (and Mn, Cr, and V) contents that match visible color changes from colorless to pale blue, medium blue, and darker blue. A strong correlation between darkening of the blue color and Fe intensity indicates that Fe is the main chromophore in the aquamarine crystal. Consistent differences exist in Fe K-edge XAS spectra pre-edge centroid position energy and integrated

intensity and Fe contents in different color zones. Pre-edge centroid energy and integrated intensity relations indicate the presence of Fe^{2+} and Fe^{3+} in 6-fold coordination in all color zones. Darker shades of blue that correlate with higher Fe contents and centroid energy than light blue and colorless zones reflect a higher overall average redox state or $Fe^{3+}/\sum Fe$ in the darker blue color zones. A colorless to very light blue area with the lowest Fe content and lowest centroid energy indicate a lower overall average redox state with lower $Fe^{3+}/\sum Fe$ than darker blue areas. Modeling of EXAFS parameters confirms the dominant presence of octahedral Fe and small amounts of Fe pairs with Fe in both the octahedral and the 6g interstitial sites in the colorless to clear blue and blue zones. EXAFS-derived nearest neighbor lengths for Fe-Fe show that the clear zone has the longest Fe-Fe bond distance (2.151 Å), whereas the blue zones are characterized by shorter Fe-Fe bond lengths (2.066 to 2.112 Å). Shorter Fe-Fe distances in the blue zones are consistent with closer Fe-Fe pairs darkening the blue color by effective IVCT. These results support previous studies that indicate that the blue color in aquamarine is caused by octahedral Fe^{2+} and enhanced by IVCT between by octahedral Fe^{2+} and 6g Fe^{3+}. This study shows the value of synchrotron Fe K-edge pre-edge and EXAFS in determining variations in the relative oxidation state of Fe and its coordination environment as well as bond lengths to nearest neighbors with color differences. This is the first Fe K-edge XAS study of a colored zoned aquamarine crystal, contributing to a better understanding of the causes of color variation in aquamarine and other colored beryl varieties, and the role of Fe in particular.

INTRODUCTION

Beryl ($Be_3Al_2Si_6O_{18}$) is a cyclosilicate mineral containing aluminum that is relatively rare and occurs in specific geological environments, although it is most commonly found in granitic pegmatites and hydrothermal veins (e.g., Barton & Young, 2002). The mineral's structure consists of layers of cyclic silicate rings (Si_6O_{18}) connected by twisted tetrahedral $Be^{2+}([BeO_4]^{6-})$ and octahedral $Al^{3+}([AlO_6]^{9-})$ sites, which crystallize in a hexagonal space group (P6/mcc) (Fig. 1a; Brag & West, 1926; Gibbs et al., 1968; Morosin, 1972; Artioli et al., 1993). Transition metal cations (Fe^{2+}, Fe^{3+}, Cr, Mn) can be found in octahedral Al sites and 6g interstitial sites (voids between Al octahedra) and 4d interstitial (voids between Be tetrahedra) sites along the c axis (Fig. 1b; Platonov et al., 1978; Mathew et al., 2000; Lin et al., 2013; Shang et al., 2022). The six-membered silicate rings are stacked along the c axis creating open channels that can accommodate alkalis (Na^+, K^+, Cs^+), transition metals (Fe^{2+}, Fe^{3+}, Cr, Mn), and large molecules such as water and carbon dioxide (e.g., Dvir & Low 1960; Wood & Nassau, 1968; Goldman et al., 1978; Aurisicchio et al., 1988, 1994; Viana et al., 2002; Andersson, 2006; Bunnag et al., 2020; Shang et al., 2022). The arrangement of cations and other molecules within the channels and various crystallographic sites affect the color and other properties of beryl.

Gemstones are natural inorganic materials with physical features such as lusters and colors that add aesthetic value and practical use in jewelry as ornament pieces. The first systematic work focusing on the origin of the color of beryl was reported by Wood and Nassau (1968), and since then, many other studies dealing with the subject have been published (e.g., Price et al., 1976; Goldman et al., 1978; Platonov et al., 1979b; Andersson, 1979, 2019; Mathew et al., 2000; Viana et al., 2002). Most of these studies are based on optical absorption, ultraviolet-visible (UV-Vis), infrared, Mössbauer, and electron paramagnetic resonance (EPR)

spectroscopy. Colorless beryl forms without elemental substitutions in its crystalline structure or elemental substitutions that do not cause color, and when it is also transparent and gem-quality, it is called goshenite (e.g., Mathew et al., 2000; Shang et al., 2022). Goshenite has also been shown to contain Fe^{2+} in channel and octahedral sites (Wood & Nassau, 1968; Mathew et al., 2000). Gem-quality blue to blue-green beryl crystals, called aquamarine, have a high demand and commercial value, are highly sought after, and are traded worldwide. For aquamarine, the deeper the blue color, the rarer and more valuable the crystal is.

Although the causes of color variation in beryl have been extensively theorized and investigated by different means, the origin of the blue color of aquamarine remains debated, variously attributed to the occurrence of ions of Fe as Fe^{2+} and Fe^{3+} in different crystallographic sites and abundance ratios (e.g., Mathew et al., 2000, Groat et al., 2010). Iron occurs as Fe^{2+} or Fe^{3+} dominantly replacing Al^{3+} in octahedral sites (e.g., Aurisicchio et al., 1988), but other site occupancies have been postulated based on spectroscopic studies and bond length constraints, and disputed, including: interstitial sites, Fe^{3+} in tetrahedral sites replacing Be^{2+}, and channel sites (Andersson, 2013); Fe^{2+} in channel sites (Wood & Nassau, 1968; Goldman et al., 1978; Viana et al., 2002); and pairs of Fe atoms in two different octahedral sites (e.g., Dvir & Low, 1960; Wood & Nassau, 1968; Price et al., 1976; Goldman et al., 1978; Platonov et al., 1979 a,b; Blak et al., 1982; Mathew et al., 2000; Spinolo et al., 2007; Figueiredo et al., 2008; Groat et al., 2010; Andersson, 2013; Taran & Vyshnevskyi, 2019; Bačik & Fridrichová, 2019). A common pale blue color in aquamarine has been attributed to Fe^{2+} residing in channel sites and seen in optical absorption spectra (Wood & Nassau, 1968; Price et al., 1976; Goldman et al., 1978). On the other hand, a deeper blue color in aquamarine with specific bands in the optical absorption spectra was attributed to inter-valence charge transfer (IVCT) transition of electrons between

Fe^{2+} and Fe^{3+}, with Fe^{2+} located in the octahedral Al^{3+} site and less Fe^{3+} interacting from an interstitial site (Dvir & Low 1960; Wood & Nassau, 1968; Goldman et al., 1978; Platonov et al., 1979 a,b; Mathew et al., 2000; Taran & Rossman, 2001; Spinolo et al., 2007; Figueiredo et al., 2008; Groat et al., 2010; Lin et al., 2013; Taran et al., 2018; Taran & Vyshenevskyi, 2019; Shang et al., 2022). In the latest study, Shang et al. (2022) used electron microprobe, UV-Vis, energy dispersive X-ray fluorescence (XRF), and Fourier transform infrared (FTIR) spectroscopy to conclude that the blue coloration mechanism in beryl was given by ultra-violet charge transfer (UVCT) from O^{2-} to Fe^{2+} and IVCT between Fe^{2+} substituting for Al^{3+} and Fe^{3+} located at the 6g interstitial position. The latter is consistent with earlier studies by Mathew et al. (2000).

A very small number of studies utilized synchrotron radiation X-ray absorption spectroscopy (XAS) techniques to investigate the properties of Fe that may cause different colors in beryl (Eeckhout et al., 2005; Chankhantha et al., 2016), and very few studied the blue color in aquamarine (Figueiredo et al., 2008; Lin et al., 2013; Bunnag et al., 2020). Synchrotron radiation micro-XAS techniques are well-established, non-destructive, and robust analytical techniques for probing the atomic state of elements within minerals and silicate glasses that have been used to understand the local atomic structure and oxidation state of transition metals, including the determination of neighboring environments such as coordination numbers and bond distances (e.g., Bajt et al., 1994; Westre et al., 1997; Wilke et al., 2001; Bonnin-Mosbah et al, 2002; Dyar et al., 2002a, 2016; Berry et al., 2003; Villain et al., 2007; Ingall et al., 2010; Evans et al., 2014; Feige et al., 2017; Bunnag et al., 2020).

It has been demonstrated that in the XAS spectrum at the absorption edge (K-edge) for the innermost electron shell (K-shell) arising from 1s→3d (and/or 1s→4p) electronic transitions for transition metals with an open 3d shell, small absorption features present ~10-15 eV below

the edge (the pre-edge) and edges are shifted to higher energy with increasing $Fe^{3+}/\Sigma Fe$ ratios (Bajt et al., 1994; Berry et al., 2003; Penner-Hahn, 2003; Newville, 2004). High-resolution Fe K-edge XAS investigations on Fe-bearing minerals and glasses show that overall, the area, position, and intensity of pre-edge peaks can be correlated with oxidation state and local coordination (Bajt et al., 1994; Arrio et al., 2000; Wilke et al., 2001; Giuli et al., 2002; Berry et al., 2003; Farges et al., 2004; Quartieri et al., 2005; Delaney et al., 2014). Specifically, it has been revealed that the energy position of pre-edge peaks can be used to quantitatively determine the Fe redox ratio, while their intensity can provide information on the coordination state and site distribution. The extended X-ray absorption fine structure (EXAFS) region of the overall XAS spectrum, starting approximately 20-30 eV above the absorption edge, is characterized by modulations arising from interference effects of scattered electrons with their neighboring atoms. EXAFS data for a specific element is obtained by adjusting the energy of the synchrotron-induced X-rays to that of the binding energy of the innermost electron shell. The EXAFS spectra can be interpreted by inverting the pattern and providing a radial distribution function (Wenk & Bulakh, 2004). The curve produced gives the probability of finding the nearest neighbor at a distance from the absorbing atom. This distance (in Å) is derived from a theoretical EXAFS equation (Newville, 2004) and is used to determine the coordination geometry and the element being substituted.

Three synchrotron-based XAS studies investigated aquamarine crystals to determine the oxidation state and coordination environment of Fe, reaching different conclusions. A Fe K-edge XAS study of blue beryl from Mozambique by Figueiredo et al. (2008) determined that Fe was present predominantly as Fe^{2+} in the octahedral Al site based on the position, intensities, and distinct combinations of pre-edge peaks compared to those from previous studies of glasses and

other minerals by Waychunas et al. (1983), the pre-edge model of Wilke et al. (2001), and blue sapphire studied by Jheeta & Jain (2007). The substitution of Fe^{2+} in the octahedral site was interpreted to be responsible for the blue coloration. Lin et al. (2013) confirmed the occurrence of Fe pairs along the c axis within light blue beryl from South Africa utilizing single-crystal Electron paramagnetic resonance (EPR) and modeling of the EXAFS area of synchrotron Fe K-edge XAS spectra. One Fe^{3+}-Fe^{3+} pair was suggested to correspond to Fe^{3+} ions at the two nearest Al sites, whereas a second Fe^{3+}-Fe^{3+} pair corresponds to Fe^{3+} ions at an Al site and its nearest 6g interstitial position. Their study presented the first experimental confirmation by XAS that the blue coloring in aquamarine is due to charge transfer between adjacent Fe^{3+}-Fe^{2+} pairs in the octahedral Al site and its adjacent 6g interstitial site, consistent with the proposed cause of color in aquamarine by other studies that utilized different spectroscopic techniques (e.g., Dvir & Low, 1960; Wood & Nassau, 1968; Loeffler & Burns, 1971; Platonov et al., 1979b; Mathew et al., 2000; Taran & Rossman 2001; Groat et al., 2010). Bunnag et al. (2020) studied the oxidation state and coordination environment of Fe in four aquamarine crystals from Africa with different color shades using near-infrared (NIR), Raman, and UV-Vis spectroscopy, and Fe K-edge pre-edge and X-ray absorption near-edge (XANES) spectroscopy parameters. Results from the study indicate the presence of both Fe^{2+} and Fe^{3+} in all samples and that Fe resided predominately in 6-fold coordinated sites. A deeper blue shade in an aquamarine sample contains both Fe^{3+} and Fe^{2+} in octahedral and interstitial sites and this specific configuration of iron resulted in a darker blue shade compared to the other beryl samples.

Investigations of intra-crystal color zoning in individual aquamarine crystals to determine the structural role of Fe in generating color variations are yet to be undertaken utilizing the capabilities of non-destructive, synchrotron-based X-ray absorption spectroscopy techniques. In

addition, although synchrotron radiation micro-XRF is capable of providing a highly detailed view of small-scale compositional variations, it has yet to be used to investigate elemental contents within beryl crystals and their relationship to XAS parameters and color. However, the closest for this aim is a recent optical absorption study combined with electron microprobe analysis by Taran & Vyshnevskyi (2019) in which the intensity of $^{Al}Fe^{2+}$, $^{Al}Fe^{3+}$, $^{6g}Fe^{3+}$, and $^{Be}Fe^{2+}$ bands were used to evaluate inter- and intra-crystal variations in blue beryl crystals of different colorations from colorless to dark blue. The study showed some intra-crystal zoning in iron species along the c axis of some crystals, particularly in $^{Al}Fe^{2+}$ and $^{Be}Fe^{2+}$, and homogeneity in $^{Al}Fe^{3+}$ and $^{Be}Fe^{2+}$ in other samples, and variations in the band featuring the IVCT transition between $^{Al}Fe^{2+}$ and $^{6g}Fe^{3+}$ that has been considered to produce the blue color. Although not focused on beryl, Arletti et al. (2008) utilized an approach of combined synchrotron micro-XRF mapping and mapping of Fe K-edge micro-XANES pre-edge parameters to characterize the color response to elemental variations and relative oxidation state of Fe in different colored parts of glasses and vessels. They determined the position of the pre-edge peaks and intensity using the pre-edge extraction procedure and normalization of Wilke et al. (2001), from which mapping of variations in Fe oxidation state were used to identify areas where Fe^{2+} and Fe^{3+} dominated, showing the usefulness combination of the synchrotron techniques.

In this study, we investigated the relationship between color variation and average oxidation state and coordination environment of Fe in a color-zoned aquamarine crystal from Brazil ranging from colorless to various shades of blue using combined synchrotron-based Fe K-edge micro-XAS and micro-XRF spectroscopy analysis. The goal was to identify the relationship between various color zones, Fe, Cr, Mn, and V intensity variations from micro-XRF mapping, and values of Fe XAS parameters in the XANES pre-edge region, including centroid fit energy

and integrated intensity, and EXAFS regions, including bond lengths and nearest neighbors. The present study used a somewhat similar technique as that of Arletti et al. (2008) of combining synchrotron-based micro-XRF and micro-XAS to determine the relative oxidation state of Fe in different colored zones within a zoned aquamarine. At the time of writing this paper, this is the first study combining synchrotron-based XAS and micro-XRF analysis of blue beryl and the first study presenting detailed Fe chemical maps in a zoned aquamarine to visualize and explain quantitatively the relationship between Fe contents, XAS and EXAFS parameters indicative of coordination geometry (IV or VI) of Fe, relative oxidation state (as Fe^{3+}/Fe^{2+}) of Fe, and bond distances and blue color variation in a single crystal. Characterizing the local atomic structure of Fe in aquamarine and its link with color provides insights into the origin of the blue color variations in beryl as a key gemstone-defining characteristic, which can aid in the treatment process. Further, fingerprinting these physical-chemical properties and beryl's natural atomic environment in general may prove useful in gemology and in the processing of the critical metal beryllium.

SAMPLING AND ANALYTICAL METHODS

Sample Description

A euhedral, color-zoned aquamarine crystal (sample 86394) from Minas Gerais, Brazil, housed in the Geological and Mineralogical Museum at Harvard University, measuring 18 mm long and 10 mm wide, was used in this study (Fig. 2). The crystal exhibits a doubly terminated hexagonal prismatic habit with a pyramidal {1111} zone of triangular faces and a hexagonal prismatic zone with flat rectangular faces and no striations. Color zoning in the crystal is characterized by four parallel zones perpendicular to the c axis, starting with a colorless area (5

mm thick) on one end, a transition to a light blue zone (2 mm thick), followed by a dark blue area (3 mm wide) in the center, and then a medium blue zone (3 mm thick). The remaining (5 mm long) crystal has inclusions and surface minerals; it is opaque, white, and lacks blue coloration.

The zoned aquamarine crystal is derived from an unknown locality in Minas Gerais, Brazil. The Brazilian state of Minas Gerais has an area of around 586,528 km^2, and the geologic background of Brazil stretches from the Archean to the Holocene (Cassedanne & Philippo, 2015). Aquamarine has been reported in two types of granitic pegmatites, zoned and complex types. Almost all the aquamarine-bearing pegmatites of Brazil are dated at 477-545 Ma (Preinfalk et al., 2002; Cassedanne & Philippo, 2015) and are hosted by biotite gneisses or porphyritic granites with quartz phenocrysts.

Two types of aquamarine-bearing pegmatites are identified based on their complexity (Cassedanne & Philippo, 2015). The most straightforward kind of pegmatite, the zoned pegmatites, are represented by thin-zoned pegmatites (1 to 2 meters) horizontally oriented, consisting of quartz and potassium feldspar with biotite and schorl. The core of the zoned pegmatite is made of massive milky quartz. It is associated with coarse-grained zones with large potassium feldspar crystals up to 0.7 m in size and sparse aquamarine crystals in the upper part of the zone. A graphic zone with centimeter-grained biotite separates the pegmatite from the host biotite gneiss. The complex aquamarine-bearing pegmatites are represented by vertical deposits 5 meters thick and hosted by porphyritic quartz granite. The pegmatite core consists of cracked milky quartz. It is associated with a very coarse-grained zone with potassium feldspar crystals up to 0.5 m in size and vugs coated with albite, quartz, and aquamarine crystals. A graphic zone with centimeter-size biotite separates the pegmatite from the porphyritic quartz granite.

Synchrotron Micro-XRF and Micro-XAS Analysis

Synchrotron-based XAS and micro-XRF analysis were conducted at the Advanced Photon Source (APS), Argonne National Laboratory, IL, using beamline 13-ID-E due to the high brilliance of the X-rays and the high spatial resolution provided (Fig. 3). The aquamarine crystal was placed on a sample holder and oriented horizontally with its c axis oriented horizontally and at 45° from the direction of propagation of the incident X-ray beam (Fig. 3). The zoned aquamarine crystal (sample 86394) was probed for Fe at the K edge (7112 eV) using a Si (111) monochromator to obtain an adequate energy resolution under an undulator-based (high flux) beamline of 2 μm in size and using silicon mirror stripes. X-ray Larch software (Newville, 2013) was used for normalization, pre-edge peak, and FEFF analysis. Micro-XRF data were obtained on the aquamarine crystal at the same beamline using a Canberra SXD-7 XRF detector with an experimental distance of 81 mm. The X-ray energy for generating XRF elemental maps was set to 10 keV with an X-ray intensity (I0) flux of 8.83959×10^{11} Hz and an incident angle and exit angle at 45 degrees concerning the c axis of the crystal. The distance from the zoned aquamarine crystal to the detector was 50 mm, with a detector area of 50 mm^2 to create the map. A series of points close to the center length of the crystal was selected to mark the area for XRF elemental maps using the FLIR optical microscope in the experimental station that can zoom to the micrometer scale. The position of the points chosen was input into the GSE *MapViewer* program (Newville, 2013) in an XY coordinate system.

Within the zoned aquamarine crystal, spots were selected for XAS analysis to obtain the Fe Kα XAS spectrum in fluorescence mode based on specific zones within the crystal, as seen in detailed micro-XRF elemental maps. XANES mapping was recorded on spots along the c axis of the aquamarine crystal by collecting the Fe K-edge signal on light blue to dark blue zones and in

a colorless zone. For analysis of spots within the crystal at X-ray energies for a particular element, the Epics Scans script was coded to move the energy of the X-ray beam to match the binding-core energy of the innermost electron shell (i.e., “move_to_Fe(), move_to_Cr(), or move_to_Mn()”, where () refers to the coding input into the program to move the energy of the X-ray to the binding core energy of the particular element. Once the X-ray was at sufficient energy, code was written into the Epics Scans script to denote the position in the crystal where the scan would take place, the element investigated, and the number of XAS scans to perform at that position (i.e., “pos_scan(‘86394_spot1’), ‘Fe_XANES’, number=1”, where “pos_scan(‘86394_spot 1’)” indicates the type of scan (position) for sample 86394 for a spot one selected with specific XY coordinates on the sample stage, “Fe_XANES” is the chosen element and the type of spectroscopy technique used, and “number=1” refers to how many scans are to be done at the designated spot). The raw μ(E) data were read into the software program XAS Viewer (Newville, 2013), and the ten spot analyses were observed individually and as a group.

Code written in the Epics Scans script (Newville, 2013) was used to obtain XRF maps for Fe, Cr, and Mn at an acceptable energy range for elemental intensities within the samples (“move_to_mapkev()”). The software program GSE XRM MapViewer application in the X-ray Larch XAS analysis package (Newville, 2013) was used to generate and view chemical maps. The XRF map was created by selecting a center point using the optical microscope and then setting a size 6 mm long in the horizontal direction parallel to the c axis of the crystal and 1 mm in the vertical direction perpendicular to the c axis of the crystal mounted on the sample stage. A total of 1201 and 201 pixels were recorded parallel and perpendicular to the crystal's c-axis, respectively). In each direction, the step or interval was chosen at 0.0050 with a 10.0 ms per pixel dwell time. Once the XRF map scan was completed and the map generated, ten spots were

selected for XAS analysis at a single pixel within the GSE Map Viewer application based on their Fe kα region of interest (ROI) intensity using the multi-channel analyzers sum (mcasum) detector and the scalars normalization with I0 (incident X-ray intensity). Their location within the crystal was recorded for later use to obtain XAS data at those spots. The raw μ(E) data of the ten spots analyzed were read into the software program XAS Viewer (Newville, 2013). The ten spot analyses were observed individually and as a group.

TREATMENT OF XAS FE-KA DATA

XAS full spectrum data normalization and fitting

XAS spectra of the ten spot analyses were normalized by fitting the spectral region from 7050 to 7090 eV before the pre-edge using a Victoreen function and subtracting this as background absorption following the methodology of Wilke et al. (2001). The spectra were then normalized for atomic absorption based on the average absorption coefficient of the spectral region from 150 eV to 300 eV above the edge following Giuli et al. (2002). A polynomial normalization method with a constant polynomial type was used for all XAS analyses. Energy calibrations were achieved using Fe foil as a reference, and the position of the first inflection point was taken at 7110.913 eV.

XAS Fe-Kα pre-edge fitting

Pre-edge features, particularly the two pre-edge peaks, were extracted for individual XAS spectrum by fitting a baseline model to the pre-edge region with a fit energy range of 7108 to 7116 eV. A linear and Lorentzian baseline form was used with a baseline skip range of 7110 to

7115 eV (Wilke et al., 2001). The ten Fe XAS spot analyses were fitted with two pre-edge peaks, with the pre-edge of each spectrum deconvoluted into two Voigt components. The two fitted pre-edge peaks at low and high energy were labeled P1 and P2, respectively. From the pre-edge fitting using the Voigt distribution function in the pre-edge peaks deconvolution, the parameters normalized height (intensity, arbitrary units, a.u.), amplitude (area), center position energy (in eV), and full-width half-maximum (FWHM), in addition to sigma (σ), and gamma (γ, Voigt distribution function) of each peak identified were obtained using the XAS Viewer program. The average pre-edge information was obtained by calculating the integrated intensity and the fit centroid. The pre-edge fit centroid is the intensity-weighted average of the peak components' energy positions calculated by adding each pre-edge component area multiplied by its center energy position and dividing by the sum of the areas (P1 center*P1 area +P2 center*P2 area)/ (P1 area + P2 area). The integrated intensity is calculated by adding the area of each pre-edge component peak (P1 area + P2 area). The integrated peak height is calculated by adding the heights of the pre-edge peak components (P1 h + P2 h). The energy of the model compounds reported by Wilke et al. (2001) was first rescaled to compensate for the different calibrations adopted in the present study following Giuli et al. (2002). See details in the elaboration below.

EXAFS data fitting

To model the EXAFS region of the Fe XAS spectra of the zoned aquamarine crystal, the program XAS Viewer relies heavily on theoretical XAFS spectra using FEFF (Newville, 2013), was used. First, a crystallographic information file (CIF) with known bond distances for beryl with Fe was selected in the octahedral site replacing Al, the tetrahedral site replacing Be and the channel site. Then, using Fe as the absorbing atoms in different coordination sites, the scattering

amplitude and phase shifts are calculated theoretically. The calculation containing the scattering factors and mean-free path for a given coordination site is stored. Once the theoretical scattering factors are obtained, the program refines the structural parameters from the zoned aquamarine EXAFS data. The functions *f(k)* and *δ(k)* (and also *λ(k)*) derived from the EXAFS equation are used to predict and modify the structural parameters R (distance to the nearest neighbor, in Å; N, coordination number; and σ^2 (sigma square, mean square relative displacement), and also allow E_0 (absorption threshold) to change until a best-fit to the $\chi(k)$ of the data is obtained. EXAFS analysis of the zoned aquamarine was performed in R-space because it selectively ignores higher coordination shells. Therefore, when analyzing the data using R-space, the entire complex EXAFS $\chi(R)$, not just the magnitude $|\chi(R)|$, is used (Newville, 2004). The beryl structure used to model the zoned aquamarine corresponds to a dark blue aquamarine from the True Blue showing, Yukon Territory, Canada (Groat et al., 2010).

RESULTS

Variations in elemental abundances from synchrotron micro-XRF mapping

To evaluate the chemical composition of the aquamarine crystal in different color zones, continuous micro-XRF spectra were collected in an area of the zoned aquamarine crystal with different color zones. The micro-XRF elemental map (6 mm long x 1 mm wide) was obtained in a part of the crystal along the c axis showing a transition from colorless to light blue, dark blue, and medium blue bands (Fig. 7a). In the XRF Fe chemical map of the visually color-zoned aquamarine crystal, various zones with Fe intensity variations perpendicular to the c axis of the crystal are seen. A comparison between the results of micro-XRF Fe elemental mapping and color variations shows a clear correlation between Fe intensity and the color of the zoned

aquamarine (Fig. 7a). Overall, the map for Fe intensity shows Fe contents increasing from the lowest in the colorless zone to the highest in the darkest blue zone. The dark blue color zone has the highest Fe content, in contrast to the colorless to light blue regions that have the lowest Fe intensity of the measured zones and the medium blue region that has an intermediate Fe intensity. The XRF mapping along the crystal identifies additional elemental content distribution and variations that may be related to different color zones (Fig. 7).

In detail, the XRF Fe chemical map shows that the lowest Fe intensity zone coincides with the clear to light blue color zone of the crystal, as expected (Fig. 7a; spots 1, 2, and 3). Following the low Fe intensity zone, an abrupt transition occurs within the Fe chemical map to a very low Fe intensity region (0.25 mm wide) that reflects a fracture or lower relief zone. The highest Fe intensity is located in the darkest blue color zone (spots 5-7; 2 mm wide). A zone where Fe intensity decreases and is intermediate compared to the lowest and highest measured (spots 8-10) coincides with a medium blue color in the crystal. The Cr and Mn XRF chemical maps show a similar distribution in elemental intensity as the Fe chemical map (Fig. 7 a-f). Vanadium contents, as seen in the XRF chemical map, vary less than Fe, Mn, and Cr intensities, but regions of low V intensity are slightly higher than those of low Fe, Mn, and Cr intensity.

Micro-XRF elemental maps were also used to extract Fe, Cr, V, and Mn intensities in various points within the crystal (Fig. 8a-c). A comparison between Fe and Cr intensities obtained from the XRF maps and crystal color show a very low positive correlation ($R^2 = 0.18$) between Fe and Cr intensity, but a strong correlation exists between them and color, with the two highest Fe and Cr intensities occurring in two spots of the dark blue zones, whereas lower Fe and Cr intensities correspond with clear, light blue, and medium blue areas (Fig. 8a). In addition, the lowest Fe intensities are in the colorless and light blue zones, with lowest Cr intensities in one

light and one medium spot. In contrast with Fe, there is no correlation between the different color zones and Cr intensity. A stronger positive correlation exists between Fe and Mn intensities than and Fe and V intensity (R^2 = 0.35 and 0.2; Fig. 8b,c, respectively). A similar weak positive correlation between Fe and Mn contents in blue beryl was also described by Hu & Lu (2020). Overall, only Fe varies consistently with blue color changes. Because the exact location of the map within the crystal is somewhat uncertain, the precise location of the spot analyses within the different color zones, particularly due to the very-fine nature of color zoning, is approximate and based on a visual estimate and measurements of distances from the chemical map and image of the crystal.

General characteristics of micro-XAS spectra of zoned aquamarine

The Fe K-edge full spectra and XANES pre-edge zoomed in area for the nine spot analyses are shown in Figure 4 in plots of normalized μ(E) *vs.* Energy (eV). In the graph of the derivative of the normalized absorption spectrum (μ(E) ($d\mu_{norm}(E)/dE$)) *vs.* Energy (eV), at the absorption edge and where the absorption threshold (E_0) is observed as the maximum of the first derivative, two peaks are observed for all aquamarine spot analyses (Fig. 5). The two peaks represent two different phases or spectral types (basically Fe^{2+} and Fe^{3+}) that are present as a strong first derivative of μ(E) peak and another strong peak or smaller peak feature.

XAS pre-edge peak characteristics

The best fit of the pre-edge spectra obtained by the XAS Viewer computer program (Newville, 2013) is presented in Figure 6. Table 1 reports the values of the parameters extracted

from Fe K-edge spectral features, including peak position, fit centroid position energy, peak area, peak height, and integrated intensity of the different spots within the various color zones. Visually, the pre-edge spectra for all spots analyzed in the different colors of the zoned aquamarine look similar, with one peak at lower energy (peak 1) and a shoulder toward higher energy (peak 2) clearly visible (Fig. 6).

Pre-edge deconvolution shows that centroid positions for the pre-edge peaks vary from a low of 7112.670 (eV) measured in a colorless spot to a high of 7112.738 (eV) in a dark blue color spot (Table 1). The center of the first pre-edge peak, at lower energy, ranges from 7112.463 (eV) in a colorless spot to 7112.503 (eV) in a light blue color spot. At higher energy, the center of the second pre-edge peak ranges from 7114.057 (eV) in a medium blue spot to 7114.114 (eV) in a light blue color spot. Differences in the amplitude (area) of the pre-edge peaks cannot be visually distinguished in the various analyses from spectra observations alone. However, in all the analyses, the first pre-edge peak located at lower energy has a larger amplitude than the second pre-edge peak at a higher energy center position. For example, the amplitude of the first pre-edge peak ranges from 0.041725 in a colorless spot to 0.054339 in a dark blue spot, whereas for the second pre-edge peak, it ranges from 0.006212 in a colorless spot to 0.009953 in a dark blue color spot. In addition, the height of the two pre-edge peaks, recorded in normalized intensity (a.u.) at lower and higher energy, respectively, varies. The intensities of the first pre-edge peak range from 0.01892 in a colorless spot to 0.02490 in a dark blue spot. The intensities of the second pre-edge peak, at higher energy, range from 0.00472 in a colorless spot to 0.00636 in a dark blue color spot.

Relationship between pre-edge peak parameters, Fe contents, and shades of blue color

Pre-edge peak component parameters and Fe intensity derived from the XRF chemical maps were compared to determine any existing correlation with color. A strong positive correlation exists between the pre-edge fit centroid energy positions for the aquamarine data fitted together and Fe intensity for all nine spots analyzed in the different color zones of the crystal (Fig. 9a; $R^2 = 0.8274$). Overall, the pre-edge fit centroid and Fe intensity are lowest for the clear blue spot and highest for the darkest blue spots. The spot within the clear zone and the light blue area are characterized by a low pre-edge fit centroid energy (7112.670 – 7112.695 eV) and low Fe intensity. A light blue spot, three blue spots, and a dark blue spot have intermediate pre-edge fit centroids (7112.707 – 7112.724 eV) at higher energy than that of the colorless area and a medium Fe intensity. Two dark blue spots with the highest Fe intensity also have the highest pre-edge fit centroid energy (7112.729- 7112.738 eV).

A strong positive correlation also exists between pre-edge integrated intensity, Fe intensity, and color within the crystal ($R^2 = 0.9125$; Fig. 9b). Overall, the colorless spot is characterized by the lowest integrated intensity and Fe intensity, in contrast to the darker blue areas that are defined by the highest integrated intensity and Fe intensity, and the light blue and medium blue spots that have intermediate integrated intensity and Fe intensity between the dark and colorless areas. A strong positive correlation also exists between pre-edge integrated peak height, Fe intensity, and color within the crystal ($R^2 = 0.9662$; Fig. 9c). The colorless spot is characterized by the lowest pre-edge integrated peak height and Fe intensity. In contrast, high integrated peak height and Fe intensity define the darker blue areas. The light blue and medium blue spots have intermediate pre-edge integrated height and Fe intensity.

EXAFS FEFF R-space fitting

The Fe K-edge EXAFS data of the zoned aquamarine crystal modeled using FEFF8 in the software program XAS Viewer consist of four main R-space peaks seen in the graph of R (Å) *vs.* $|\chi(R)|(A^{-3})$ (Fig. 10). The model was created using a crystallographic information file (CIF) structure and reference distances from Groat et al. (2010) with Fe substituting for Al^{3+} in the octahedral site, with the first shell scattering paths from the six nearest neighbor oxygen atoms having identical Fe-O distances and the second nearest neighbor paths from six silicon atoms also having the exact same Fe-Si lengths (Lin et al., 2013). The R distances for the four peaks labeled 1-4 were derived from the FEFF model (Table 2).

Variations in distances to the nearest neighboring atoms can be identified between different color spots (Table 2). Using a model with a Fe-O path of 1.9416 Å with six neighboring oxygen atoms ($^{VI}Fe^{2+}$-O), the R-value distance for peak 1 varies slightly between spots, ranging from 1.9142Å in a blue spot to 1.9740 Å in a dark blue color spot. The R-value for peak 2 was modeled using an Fe-Fe path with octahedral Fe atom and an Fe atom located in the 6g interstitial position along the c axis at ~ 2.300 Å ($^{VI}Fe^{2+}$-$^{6g}Fe^{3+}$). The modeled R values for the Fe-Fe path vary between spot analyses from 2.066 Å in a dark blue spot to 2.1509 Å in a colorless spot. The R-value for peak 3 was modeled using an Fe-Si path of 3.2979 Å for octahedral Fe and its nearest Si atom (along the c axis, $^{VI}Fe^{2+}$-^{IV}Si), with the modeled Fe-Si path varying between spot analyses from 3.2938 Å in a blue color spot to 3.3529 Å in a dark blue color spot. The shoulder feature, peak 4, at a further atomic distance was determined to be an Fe-O path representing the bond length between octahedral Fe to one of its six neighboring oxygen atoms at a model distance of 3.7865Å ($^{VI}Fe^{2+}$-^{IV}O). This Fe-O path varies between spot analyses from 3.0206 Å in a blue color spot to 4.5157 Å in a light blue spot. The peak observed in the

EXAFS R-space fitting at a model distance of 4.6 Å representing the distance between two octahedral Al sites of Fe-Fe replacing Al in those sites could not be modeled using the FEFF paths available after numerous attempts and will not be discussed.

The relative probabilities of the four modeled peaks representing nearest neighbor atomic distances are similar in all spot analyses, which in order from high to low are: $^{VI}Fe^{3+}$-O path > $^{VI}Fe^{2+}$-^{IV}Si > $^{VI}Fe^{2+}$-$^{6g}Fe^{3+}$ > $^{VI}Fe^{3+}$-O. The peak for $^{VI}Fe^{3+}$-O (peak 1) yields the highest probability (1.2-1.4 $|\chi(R)|(Å^{-3})$), whereas the peak for $^{VI}Fe^{3+}$-O (peak 4), has the lowest probability (0.4-0.5 $|\chi(R)|(Å^{-3})$) compared to the other FEFF paths (Fig. 10). The σ^2 values for the different FEFF paths (Fe-O, Fe-Fe, Fe-Si) are used in EXAFS to account for thermal and static disorder in an ensemble of different paths that make up a full EXAFS spectrum. The σ^2 values vary between the various spot analyses within the zoned aquamarine from $2.2x10^{-9}$ in peak 3 to 0.9899 in peak 4 (Table 2).

DISCUSSION

This study utilized synchrotron XAS and X-ray fluorescence XRF spectroscopy to investigate potential variations in the oxidation state and local environment of Fe atoms, related to color variations within a zoned aquamarine crystal. Previous research has shown that the spectral characteristics observed in the pre-edge region correspond to the electronic transition from 1s to 3d orbitals, from which the average oxidation state and coordination geometry can be inferred. Several calibrations have established a correlation between the XAS spectra parameters of pre-edge fit centroid and integrated intensity with the $Fe^{3+}/\Sigma Fe$ ratio within silicate glasses and other minerals (Berry et al., 2003; Cottrell et al., 2009; Dyar et al., 2016). Moreover, some

studies have determined the relative oxidation state (i.e., $Fe^{3+}/\Sigma Fe$) of minerals from their pre-edge peak centroid and integrated intensity by using standards with known oxidation state and coordination geometry (Bajt et al., 1994; Wilke et al., 2001). The following discussion will explore the observed relationships between color variations, Fe, Cr, Mn, and V content, several XAS and EXAFS parameters, and their potential significance.

Fine-scale blue color zoning relation to synchrotron micro-XRF Fe, Mn, Cr, V variations

Synchrotron-based micro-XRF chemical maps of the zoned aquamarine show fine-scale zoning in Fe, Cr, V, and Mn intensity with bands down to 1 mm in width that further exhibit additional internal zoning (Fig. 7). For example, Fe intensity increases within a 1 mm band from spot 2 to 3. Micro-zoning of Fe, and to a lesser degree Mn, correlates with variations in visible color from clear to light blue, medium blue, and dark blue as seen in the chemical maps. From synchrotron XRF chemical maps, a strong correlation is observed between the darkening of the blue color with increasing Fe content (Fig. 7). In general, this is expected, as iron tends to darken mineral colors. The observation that the colorless to light blue spot analyses have the lowest Fe content and the medium and dark blue spot analyses have the highest Fe content within the crystal agrees with early beryl studies by Goldman et al. (1978) and a recent spectroscopy study of colored beryl, including aquamarine, by Hu & Lu (2020), and recent results of Shang et al. (2022). In a study of different Fe-bearing colored beryl varieties, Shang et al. (2022) compared Fe contents obtained by energy-dispersive XRF spectroscopy and electron microprobe analysis with color to show that Fe is the most critical chromophore in yellow to light blue beryl. Their results are consistent with those of the present study visible in the micro-XRF chemical maps that show that Fe intensity is directly related to color variations (Fig. 7). In addition, Mn intensity

variations follow those of Fe, whereas Cr intensity varies less, and V varies the least with color. Cross plots of Fe, Mn, Cr, and V intensity also show that Fe varies somewhat similar than Mn ($R^2 = 0.351$), with one dark blue spot being an outlier with much higher Mn contents, possibly due to an inclusion or surface mineral contributing to the higher value (Fig. 8b). In contrast, V and Cr do not co-vary with Fe, and V, Cr, and Mn do not exhibit any correlation among them nor with color variations (Fig. 8a-c). The strong correlation between darkening of the blue color and Fe intensity indicates that Fe is the main chromophore in aquamarine, consistent with numerous spectroscopy studies, including the only synchrotron study of aquamarine (Bunnag et al., 2020) and the study by Hu & Lu (2020). Further, the correlation of Fe with Mn contents and the blue color variation with Fe intensity seen in the results of micro-XRF is similar to that among individual goshenite and aquamarine crystals of different blue intensities shown by Hu & Lu (20120. In addition, Hu & Lu (2020) reported that Mn contents were lower than for Fe, but the darkest blue beryl have the highest Mn contents and other blue crystals have lower Mn contents, consistent with the intra-crystal variations seen in the zoned aquamarine crystal. The weak positive relationship between Fe and Mn contents in the zoned aquamarine likely reflects substitution of the elements in the octahedral Al site, based on their similar charge (2+ and/or 3+), radii, and coordination geometry, as in the case of the different blue crystals studied by Hu & Lu (2020). Although they do not report the R^2 value correlating Fe and Mn contents in the various beryl crystals, not only they included colorless and yellow samples in addition to blue, but the data are for different samples, which cannot be compared with the single crystal studied here. Finally, the lower Cr and V contents seen here in the aquamarine crystal compared to Fe and Mn are consistent with the very low Cr and V concentrations measured in the blue crystals by Hu & Lu (2020).

Based on detailed synchrotron micro-XRF chemical maps, color zoning in the zoned aquamarine crystal is mainly defined by changes in Fe content. Although no chemical maps were presented in the optical absorption spectroscopy study of Taran & Vyshnevskyi (2019), intra-crystal variations in Fe contents were identified by electron microprobe analysis and by the relative size of specific Fe bands in the spectra of blue beryl. They showed that $^{Al}Fe^{3+}$ was homogeneous, that $^{Al}Fe^{2+}$ was zoned within the crystals, and that $^{Be}Fe^{2+}$ was complexly zoned but varied smoothly along the c axis. However, as presented, the Fe variations could only be seen as differences in the intensity of Fe spectral bands of individual spots within crystals, some of which had color variations seen in photos of the crystals, but not in chemical maps related to exact places in the crystal. Considering the findings of Taran & Vyshnevskyi (2019), the consistent Fe variations with blue color zoning in the aquamarine crystal studied here could be interpreted to reflect differences in the abundance of $^{Be}Fe^{2+}$ or $^{Al}Fe^{2+}$. However, previous studies show that blue color variations and darkening of the blue color of normal blue aquamarine are due to the presence and increasing amounts of Fe^{3+}, in addition to the occurrence of octahedral Fe^{2+}, variations in the amount of octahedral Fe^{3+} and Fe^{2+}, and the effect of the IVCT mechanism between Fe^{2+} and Fe^{3+} (Dvir & Low, 1960; Wood & Nassau, 1968; Goldman et al., 1978; Aurisicchio et al., 1988; Taran & Rossman, 2001; Viana et al., 2002; Spinolo et al., 2007; Adamo et al., 2008; Groat et al., 2010; Lin et al., 2013; Plantov et al., 2016; Taran et al., 2018; Bačik & Fridrichová, 2019; Taran & Vyshnevskyi, 2019; Bunnag et al., 2022). For example, Hu & Lu (2020) reported the presence of Fe^{3+} in all the blue beryl samples analyzed, as well as the occurrence of absorption bands representing Fe^{2+} or Fe^{2+}-Fe^{3+} pairs that increased with the darkening of the blue color. Therefore, a speculation is made here that the variations measured in total Fe in the zoned aquamarine are likely to correspond to increasing amounts of octahedral

Fe^{3+} incorporated in the crystal structure, and as a result increasing average $Fe^{3+}/\Sigma Fe$ ratios, from clear to darker blue beryl zones. This is evaluated in detail in the following sections using XAS pre-edge information.

Fe K-edge pre-edge XAS and occurrence of Fe^{2+} and Fe^{3+} in various color zones in the zoned aquamarine

Previous Fe pre-edge XAS studies of aquamarine and other materials

The use of Fe Kα pre-edge fit to determine coordination environments and relative Fe oxidation state has been demonstrated for several minerals and silicate glasses in a number of studies (Wilke et al., 2001; Bonnin-Mosbah et al., 2002; Giuli et al., 2002; Berry et al., 2003; Cottrell et al., 2009; Fiege et al., 2017), including in three studies of aquamarine (Figueiredo et al., 2008; Lin et al., 2013; Bunnag et al., 2020). This utility was also shown by Arletti et al. (2008) in a combined synchrotron μ-XRF and μ-XAS study of the coloring agent in polychrome glass in which they determined variations in oxidation state of Fe related to color. In a XANES Fe K-edge study of natural minerals and synthetic compounds, Wilke et al. (2001) showed that the pre-edge centroid and total integrated intensity are the most reliable pre-edge parameters for extracting information about oxidation state and coordination geometry. The study shows that the average pre-edge centroid positions for Fe^{2+} is at lower energy than that for Fe^{3+} located at higher energy, with a difference of 1.4 ± 0.1 eV between the two, and that the centroid position for mixed Fe^{2+}-Fe^{3+} compounds occurs between those two. Thus, this difference in centroid position with Fe valence has been used as a measure of variations in the average Fe oxidation state of Fe in minerals. That the centroid is sensitive to the oxidation state also confirms earlier

observations made by Bajt et al. (1994). In a graph of pre-edge centroid position *vs.* integrated intensity, distinctly different trends can be observed for minerals with different coordination environments ([IV], [VI]) and oxidation states (Fe^{2+} and Fe^{3+}) (Wilke et al. 2001). Although results examining the pre-edge features of Fe in different oxidation states and coordination environments ($^{VI}Fe^{3+}$, $^{VI}Fe^{2+}$, $^{IV}Fe^{3+}$, $^{IV}Fe^{2+}$) suggest that the pre-edge position and intensity for these mixtures can vary non-linearly with the average oxidation state of Fe, these variables were used by Wilke et al. (2001) to estimate the Fe^{3+}/Fe^{2+} ratio in twelve minerals containing unknown amounts of Fe^{2+}/Fe^{3+} in different coordination environments. Using a pre-edge integrated intensity *vs.* centroid energy plot modified from the pre-edge fit model of Wilke et al. (2001) and a comparison of pre-edge features of four aquamarine crystals with those of Fe^{2+} and Fe^{3+} from FeO and Fe_2O_3 standards, Bunnag et al. (2020) also identified the presence of both Fe^{2+} and Fe^{3+} as Fe pairs residing predominantly in 6-fold coordinated sites (Edgar & Hutton, 1982). Therefore, the centroid energy and integrated intensity can be used to obtain information about relative variations in valence state and coordination of Fe in the different zones of the zoned aquamarine, and this is discussed below.

Occurrence of $^{VI}Fe^{2+}$ and $^{VI}Fe^{3+}$ derived from pre-edge centroid and integrated intensity

Following Wilke et al. (2001) and Bunnag et al. (2020), the pre-edge fit centroid *vs.* integrated intensity graph was used to plot the results of the Fe K-edge pre-edge fitting of different color spots within the zoned aquamarine to compare them with the model of Wilke et al. (2001) and the position of 6-fold and 4-fold Fe^{2+} and Fe^{3+} (Fig. 11). Results show that all spot analyses in the zoned aquamarine crystal fall mostly within or close to the parameters of 6-fold coordinated Fe^{2+} and extending from those toward higher centroid energies of 6-fold coordinated

Fe^{3+}, indicating that Fe in all color zones occurs as a mixture of dominant Fe^{2+} and minor Fe^{3+} both in octahedral coordination. To compare the pre-edge centroid and integrated intensity of the zoned aquamarine spot analyses with the parameters of the four types of end-member Fe species ($^{IV}Fe^{2+}$, $^{VI}Fe^{2+}$, $^{IV}Fe^{3+}$, and $^{VI}Fe^{3+}$) used by Wilke et al. (2001), the centroid values of the aquamarine crystal were also plotted after calibrating (shifting) the energy of the Fe foil of the present study (7110.913 eV) to fit the energy of the Fe foil of Wilke et al. (2001) (7111.08 eV) using the method from Giuli et al. (2002). When plotting the pre-edge parameters with the shifted energy, the results are similar and yield the same type of correlations as those obtained without shifting the data to those of Wilke et al. (2001) (not shown).

Results from this study of the Fe K-edge pre-edge fitting of the zoned aquamarine data indicating the presence of Fe as both Fe^{2+} and Fe^{3+} predominantly in 6-fold coordination in all spots analyzed agree with previous Mössbauer spectra, charge-balance considerations, optical absorption spectroscopy, and X-ray and neutron-diffraction of dark blue aquamarine from the True Blue showing, Canada (Groat et al., 2010), EPR and synchrotron-based Fe K-edge XAS studies of a light blue beryl from South Africa by (Lin et al., 2013), synchrotron XANES and UV-vis studies of four light blue aquamarine crystals from South Africa (Bunnag et al. 2020), and UV-Vis spectroscopy studies of yellow to light blue beryl from China (Shang et al., 2022) all showing the occurrence of iron as Fe^{2+} and Fe^{3+}. Specifically based on XAS features in the Fe K-edge XANES spectra compared with five standards, Lin et al. (2013) determined that the light blue aquamarine contains a mixture of both Fe^{2+} and Fe^{3+} in octahedral coordination, consistent with study. In addition to the presence of $^{VI}Fe^{2+}$ and $^{VI}Fe^{3+}$ in various blue beryl crystals demonstrated by optical spectroscopy by Taran & Vyshnevskyi (2019), they investigated the occurrence of small amounts of $^{Be}Fe^{2+}$, particularly in colorless beryl but also in blue beryl, that

could not be distinguished in pre-edge spectra area analyzed in the present study. A four-fold coordinated geometry for Fe atoms in beryl would yield much higher pre-edge integrated intensity values than those obtained in this study (e.g., Wilke et al., 2001; Bunnag et al., 2020).

Relative $^{VI}Fe^{2+}$ and $^{VI}Fe^{3+}$ and relation to intra-crystal blue color variation

The presence of $^{VI}Fe^{3+}$ and Fe^{2+} in all spots analyzed in the zoned aquamarine (Fig. 6) is consistent with previous studies using Mössbauer and optical spectroscopy that show that in beryl Fe substitutes mostly as Fe^{2+} in the weakly distorted octahedral Al site, and that Fe^{3+} and Fe^{2+} are attributed to the origin or darkening of the blue coloration (e.g., Price et al., 1976; Platonov et al., 1978, 1979a, b). The additional presence of $^{VI}Fe^{3+}$ in the Al site or 6g interstitial site enhances the blue coloration by IVCT between the two Fe atoms ($^{Al}Fe^{2+}$-$^{6g}Fe^{3+}$) (e.g., Loeffler & Burns, 1960; Goldman et al., 1978; Taran & Rossman, 2001; Groat et al., 2010; Lin et al., 2013; Taran et al., 2017; Taran & Vyshnevskyi, 2019).

Darkening of the blue color by the concomitant occurrence of $^{VI}Fe^{2+}$ and $^{VI}Fe^{3+}$ shown in previous studies by other techniques is confirmed in the present study using the combination of synchrotron-based pre-edge XAS parameters and micro-XRF in the zoned aquamarine crystal. The graph of pre-edge centroid *vs.* integrated intensity shows a relatively strong positive correlation between the two variables that vary consistently with intra-crystal color variations (R^2 = 0.7411; Fig. 11a). The colorless and light blue spots plot closer to 6-fold Fe^{2+}, whereas the medium and dark blue spots plot toward an increase in the $^{VI}Fe^{3+}$ component. The colorless spot has the lowest pre-edge fit centroid position energy (and integrated intensity), followed by a light-blue spot, in contrast to two dark blue spots that have the highest pre-edge fit centroid (and

integrated intensity). The three medium-blue, one dark blue, and one light blue spot have intermediate pre-edge centroid energies (and integrated intensity). These centroid energy variations used as a proxy for Fe^{2+}-Fe^{3+} relations with color are consistent with the results of Taran & Rossman (2001), Groat et al. (2010), and Lin et al. (2013) that show the presence of both Fe^{3+} and Fe^{2+} as iron pairs in blue beryl. However, the results seem to differ from those from an optical spectroscopy study focused on Fe^{2+} substitution in the Be site in beryl crystals from two Brazilian deposits that show that the distribution of Fe^{3+} in the Al site in colorless, light blue, and dark blue beryl crystals is homogeneous and that there is no correlation between total Fe, $^{Be}Fe^{2+}$, and $^{Al}Fe^{2+}$, the latter imprinting the blue coloring property of beryl along with Fe^{2+}-Fe^{3+} IVCT (Taran & Vyshnevskyi, 2019). The same study showed variations in the small amount of $^{Be}Fe^{2+}$ along the c axis of the crystal from one locality that can be seen as zoning in the blue color (or in green). That the authors estimate that the concentration of $^{Be}Fe^{2+}$ is at least one order of magnitude lower than those of $^{Al}Fe^{2+}$ and $^{Al}Fe^{3+}$ and that it was the highest in a colorless beryl is consistent with the low values of pre-edge integrated intensity and centroid energy obtained for the aquamarine in this study that show the dominance of octahedral Fe (Wilke et al., 2001; Lin et al., 2013; Bunnag et al., 2020). In addition, the study by Taran & Vyshnevskyi (2019) also reported distribution variations in $^{Al}Fe^{2+}$ contents in crystals that can be seen as blue color zoning, especially when IVCT between this ion and $^{6g}Fe^{3+}$ are the strongest. It is unclear if the difference in color they attribute to $^{Al}Fe^{2+}$ variations is due to that alone or if it could be due to variability of $^{Al}Fe^{3+}$ or $6gFe^{3+}$, as interpreted in the current study, since the former study did not investigate $^{Al}Fe^{3+}$ in detail but reported homogeneous distributions in crystals.

Some overlap in centroid position between one dark blue, one medium blue, and one light blue spot may be due to slight uncertainty in the exact position of the spots analyzed within the

exact color zones, or that the small color difference is not enough to translate into consistent differences in centroid energy and integrated intensity in all cases. One dark blue spot also has a centroid position that overlaps with the medium blue spots, but its integrated intensity is higher than in the other colors. Overall, following previous studies, the highest pre-edge centroid energy that characterizes two of the dark blue spots can be interpreted as indicating a higher percentage of $^{VI}Fe^{3+}$ or higher Fe^{3+}/Fe^{2+} ratios in the darker blue color compared to the colorless and light blue zones that have lower centroid energy positions reflecting higher amounts of $^{VI}Fe^{2+}$ or lower Fe^{3+}/Fe^{2+} ratios. This can also be seen by increasing centroid energy with darkening of the blue color being best correlated with the amplitude of P2 and less with that of P1 (Fig. A1), suggesting that the size of the higher energy peak that can be considered to represent $^{VI}Fe^{3+}$ is related to the darkening of the blue color.

Bunnag et al. (2020) also showed that a darker blue aquamarine has a higher centroid position energy than medium and light blue beryl, consistent with this study. However, although Bunnag et al. (2020) concluded that the deeper blue shade was due to IVCT between Fe^{3+} and Fe^{2+} in octahedral positions, they referenced a greenish-blue sample (their AQ03 sample) as the "deeper blue" color but based on the colors seen in the picture of the crystals, it is unclear that the greenish blue sample has a "deeper blue shade" than their blue sample. Further, their blue beryl crystal plots in the Fe^{2+} model field of Wilke et al. (2001) with a lower centroid position than the light blue aquamarine and the greenish blue (darker blue) beryl that plot together at the boundary or outside the Fe^{2+} model field and slightly closer to the Fe^{3+} model field, with no correlation between the light blue, medium blue, and darker blue color and centroid position energy. This means that the samples do not show a clear correlation between the darkening of the blue color and centroid position, perhaps because of the greenish color of the darker blue sample

considered in the study. The results of this study contrast with those of an XAS Fe K-edge study of three blue beryl crystals from Mozambique by Figueiredo et al. (2008) in which a comparison between the energy position and intensities of deconvoluted pre-edge peaks with those of octahedral Fe^{2+} and Fe^{3+} from Wilke et al. (2001) were used to interpret the occurrence of only Fe^{2+} in 6-fold coordinated octahedral sites replacing Al (rather than Be in the 4-fold coordinated tetrahedral sites). Pre-edge features were also identical in all samples analyzed. However, because the centroid positions for the pre-edge peaks are not reported in the study, it is unclear how the determination of Fe occurring in its ferrous state was made. In addition, the basis to determine that Fe was octahedrally coordinated and replacing Al was not reported. However, the study concluded that the substitution of Fe by Al in octahedral coordination may be responsible for the blue color. The results of the current study show a higher

Relationship between Fe contents, pre-edge parameters, relative $^{VI}Fe^{2+}$ and $^{VI}Fe^{3+}$, and intra-crystal blue color variation

Analysis of pre-edge parameter data with color variation identified that the pre-edge centroid and peak (P1 and P2) amplitudes (areas) have a significant positive correlation with color variations ranging from clear to dark blue. Specifically, significant positive correlations exist between pre-edge centroid energy and P1 amplitude ($R^2 = 0.6369$; Fig. A1a), P2 amplitude ($R^2 = 0.8787$; Fig. A1b), and P2/P1 amplitude ratio ($R^2 = 0.6952$; Fig. A1c), all being directly correlated with darkening of the blue color. The strongest correlation is between the area of peak 2, which is the smallest of the two pre-edge peaks, with centroid and color variations. If the centroid is considered a proxy for valence state of Fe and that the high energy peak is related to Fe^{3+} (e.g., Wilke et al., 2001; Bonin-Mosbah et al., 2002), and the correlations indicate that a

higher valence state of Fe is related to an increase in the small peak (P2) located at higher energy that can be interpreted as higher amounts of Fe^{3+} causing a darkening of the blue color. This observation is consistent with previous studies that show darkening of the blue color of beryl is due to higher amounts of Fe^{3+} or Fe^{2+}-Fe^{3+} (e.g., Hu & Lu, 2020; Bumnnag et al., 2020).

Investigation of pre-edge XAS parameters with Fe intensity obtained from micro-XRF chemical maps show that Fe content is closely related to color variations from clear to light, medium, and darker blue with centroid energy and the intensity of each of the pre-edge peaks, particularly the low center energy peak located at an energy range of 7112.670 to 7112.738. Overall, the relationship between Fe intensity and centroid energy for all spots analyzed show that both parameters increase with darkening of the blue color in the zoned aquamarine crystal from the clear spot to the darker blue spots, with some overlap between one darker blue, a medium blue, and a light blue spot ($R^2 = 0.8274$; Fig. 9a). Similarly, a very strong positive correlation exists between integrated intensity and Fe intensity directly related to darkening of the blue color ($R^2 = 0.9125$; Fig. 9b). An even stronger positive correlation with color is observed between Fe intensity and integrated peak height ($R^2 = 0.9662$; Fig. 9c). A very strong positive correlation also exists between increasing Fe intensity and P1 intensity ($R^2 = 0.9555$; Fig. A2a) and Fe intensity and P2 intensity ($R^2 = 0.9103$; Fig. A2b) with color variation from clear to darker blue, but there is no significant correlation between Fe intensity and peak intensity ratios ($R^2 = 0.0935$; Fig. A2c). These relationships additionally show that an increase in Fe is related to higher Fe^{3+}/Fe_{Tot} ratios, and these generate a darker blue color in beryl.

***Relative* Fe^{3+}/Fe^{2+} in blue colors in aquamarine compared with Fe^{3+} in red beryl**

In the absence of beryl standards and to obtain quantitative information of the relative abundance of Fe^{2+} and Fe^{3+} in the different blue color zones within the crystal, a red beryl crystal from the Wah Wah Mountains of Utah (Shigley & Foord, 1984), was analyzed by Fe K-edge XAS (in the same orientation as the zoned aquamarine) and the pre-edge parameters of fit centroid energy position and integrated intensity were obtained by fitting the data of the two crystals together. Results plotted in terms of the two parameters show that the red beryl has consistently higher fit centroid energy position (7112.81749-7112.83723 eV) (and integrated intensity; 0.08115- 0.08167) than all the different color spots of the zoned aquamarine crystal (Fig. 11b; Tables 1, A2). Because iron in red beryl has been shown to occur as Fe^{3+} in octahedral coordination substituting for Al, concomitant with an absence of Fe^{2+} (Andersson, 2013, 2019; Fridrichová et al., 2018; Taran & Vyshnevskyi, 2019; Gatta et al., 2022), the average fit centroid energy (7112.82491 eV ± 0.0087 eV) obtained for red beryl is thus considered to represent $^{VI}Fe^{3+}$. Then, the lowest centroid energy of the clear blue beryl is considered to represent the lowest amount of Fe^{3+} (or maximum Fe^{2+}) present in the crystal, whereas darker blue zones thus have increasingly higher amounts of Fe^{3+}. Due to the absence of beryl crystal standards of known Fe^{3+}/Fe_{Tot} previously analyzed for XAS available for this study, calculations of the ratios are beyond the scope of this study and will be investigated in the near future.

The present is the first synchrotron XAS Fe K-edge pre-edge study of a single crystal to demonstrate a relationship between colorless and light blue color and a lower fit centroid energy indicating a higher proportion of Fe^{2+} compared to medium and darker blue color zones characterized by higher energy centroid energy reflecting the presence of Fe^{2+} and Fe^{3+} and higher Fe^{3+}/Fe_{Tot}. These results are consistent with previous studies showing light blue colors

originating from dominant Fe^{2+} in Al octahedral sites (or in channel sites) and less Fe^{3+} (Goldman et al., 1978; Lin et al., 2013; Bunnag et al., 2020; Shang et al., 2022) and darker blue colors due to octahedral Fe^{2+} and interstitial Fe^{3+}, and with more Fe^{3+} than lighter blue (e.g., Taran & Vyshnevskyi, 2019). This is consistent with the relationships shown between blue color variation and centroid position in the zoned aquamarine. To the best of our knowledge, the present is the first study to demonstrate intra-crystal blue color variations in aquamarine from clear to light blue to darker blue associated with Fe contents and relative oxidation state as seen in the centroid energy used as a proxy for mixtures of $^{VI}Fe^{2+}$ and $^{VI}Fe^{3+}$.

Relationship between EXAFS-determined Fe site occupancy, bond lengths, and blue color variation

The blue-green color of aquamarine is one of its most desirable characteristics, and it is primarily due to the presence of trace amounts of Fe within the crystal lattice. More specifically, the blue color has been attributed to Fe pairs (e.g., Dvir & Low, 1960) in the structure of beryl that undergo IVCT between Fe^{2+} and Fe^{3+} ions (e.g., Groat et al., 2010; Lin et al., 2013; Taran et al., 2017; Taran & Vyshnevskyi, 2019). Loeffler & Burns (1976) summarized that the optical absorption of aquamarine shows a metal→metal (intervalence) charge transfer transition between Fe atoms in Al-Al at a distance of 4.6 Å that is responsible for the blue color. Below, a review of the structure of beryl and a discussion of the results of the EXAFS study in the light of previous studies are presented.

Beryl's crystal structure and location of Fe atoms and bond lengths

Beryl's structure has several crystallographic sites where Fe atoms can reside, including the octahedral Al site, the interstitial 6g position, the interstitial 4d position, and the tetrahedral Be^{2+} position (Fig. 1; Platonov et al., 1978, 1979a, b, c; Taran & Vyshnevskyi, 2019). The Al sites are positioned above and below each 6g site, so that 6g-Al vectors are parallel to the c axis with an Al-6g distance of 2.3 Å (Groat et al., 2010). The $6gO_6$ polyhedron shares {001} triangular faces with two AlO_6 octahedra and is slightly larger than the AlO_6 octahedron. The 6g position has six oxygen atoms in trigonal prismatic coordination with 6g-O distances of 2.16 Å, whereas the AlO_6 octahedra has shorter Al-O distances estimated between 1.904 Å and 1.955 Å (Table 3; Groat et al., 2010; Bačík & Fridrichová, 2019). The 4d position has four oxygen atoms in square planar coordination at distances of 1.870-1.891 Å from the central atom (Groat et al., 2010; Lin et al., 2014; Bačík & Fridrichová, 2019). The Bačík & Fridrichová (2019) study calculated the average bond lengths of ferrous and ferric iron in different coordination based on analysis of 64 published beryl structures and found that the average bond length for Fe^{2+}-O in octahedral coordination is 2.154 Å, whereas in tetrahedral coordination it is 1.968 Å. For Fe^{3+}-O, the average bond length is 2.016 Å in octahedral coordination and 1.870 Å in tetrahedral coordination (Table 3). There are also two Si, two Be, and two 6g positions at distances of 1.826, 2.300, and 2.682 Å, from the 4d position, respectively.

Location of Fe atoms and bond lengths in the zoned aquamarine from EXAFS modeling

The study of the FEFF fitting of the Fe K-edge EXAFS area data of the color zoned aquamarine crystal studied here using a CIF structure from Groat et al. (2010) shows four

distinct R-space peaks in the graph of R (Å) *vs.* $|\chi(R)|(\text{Å}^{-3})$ representing different Fe bonds (Fig. 10a, b). The peaks are similar to those obtained by Lin et al. (2013) for aquamarine in the only available Fe K-edge EXAFS study for blue beryl. The FEFF fitting of the aquamarine crystal using Fe in the octahedral Al site (model Fe-O = 1.9416 Å) shows that in all spot analyses Fe has the highest probability of occurring in this site with Fe-O bond distances that vary from shorter to longer than the model distance (1.9142 to 1.9740 Å; Fig. 12; Table 2). A low-probability peak corresponding to an Fe-Fe bond modeled at 2.3 Å (2.0663-2.1510 Å) is interpreted to represent an Fe-Fe pair between the Al octahedral site and the nearest 6g site (Fig. 1b). The two bonds are discussed below in relation to color variations. Lin et al. (2013) also considered that Fe pairs could correspond to Fe atoms located in two adjacent Al sites at a distance of 4.6 Å. However, after numerous attempts modeling past the first four peaks beyond 3.8 Å was not possible in this study.

Fe in the Al octahedral site, ^{VI}Fe-O bond length variations, and blue color variation

Octahedral positions within the beryl crystal that Fe can occupy are the Al-O octahedral site and the 6g-O octahedral interstitial site. Considering available Fe interatomic distances from previous studies, most distances (1.9142-1.9742 Å) obtained from the FEFF fitting path for Fe-O are close to the lengths for Fe^{3+}-O in octahedral coordination (1.955-2.16 Å; Table 3) obtained in previous studies, including those reported by Lin et al. (2013) via synchrotron EXAFS modeling and calculation of Fe-O distances in the Al and 6d interstitial sites (1.927 to 2.455 Å). Further, the average Fe-O distance obtained (1.95 Å; Table 2) is almost the same as the model Fe-O distance (1.94 Å) of Groat et al. (2010) used in the modeling. It is noted that the shorter Fe-O modeled distances obtained for some spots of the zoned aquamarine fall within the range of Fe-O

distances reported for Fe^{3+} in tetrahedral coordination in the Be-O and 4d-Fe interstitial site (1.870-1.968 Å; Table 3; Groat et al., 2010; Lin et al., 2013; Bačík & Fridrichová, 2019). However, shorter Fe-O distances are likely due to larger amounts of octahedral Fe^{3+} substituting for Al in the zoned aquamarine studied here than in other aquamarine and beryl from studies yielding longer distances.

Variability in the modeled ^{VI}Fe-O bond distances suggests distortion of the Al-O octahedra by different amounts of Fe atoms substituting for Al, as shown in previous studies (e.g., Aurisicchio et al., 1988). However, no measurable systematic variation was found between obtained ^{VI}Fe-O distances and variability in blue color changes within the aquamarine crystal, which results in no relationships with pre-edge centroid energy, Fe contents, and integrated intensity (Fig. 12). This suggests that variations in the octahedral Fe environment alone, visualized by Fe-O bond lengths with Fe^{3+} substituting in the Al octahedra, are not related to color changes and Fe contents. Small differences in Fe-O environments in the zoned aquamarine are consistent with spectroscopy studies of zoned aquamarine by Taran & Vyshnevskyi (2019) that show that ^{VI}Fe does not vary much with zoning. Further, although Fe-O distances are expected to be longer with incorporation of Fe^{2+} into the Al octahedral site compared to the same amount of Fe^{3+} in the same site (e.g., Aurisicchio et al., 1988), the absence of correlation between centroid position energy and Fe-O distances suggests that different relative amounts of the two ions in the different color zones do not generate a consistent variation in bond length (Fig. 12). To note is also the recognition that bond lengths for metal-oxygen do vary considerably in matter and in natural beryl (e.g., Andersson, 2019; Gagné & Hawthorne 2020) and do not necessarily need to be close to those obtained for other beryl crystals. Further, complication in the absorption (single *vs.* multiple) and scattering of photoelectrons that were not

considered in the data analysis and modeling could explain the variability of the Fe-O bond length data obtained. It is also not known if the octahedral Fe-O bond length necessarily affects the color of beryl, but the results of this study suggest there is no relationship between the two. Alternatively, it is possible that the EXAFS data obtained do not allow enough resolution to distinguish small bond length variations. What has been shown to be related to blue color zoning in beryl is the amount of $^{VI}Fe^{2+}$, which is consistent with XRF-determined Fe intensities that clearly correlate with color zoning (Taran & Rossman, 2001; Taran & Vyshnevskyi, 2019).

Interatomic distances of Fe-Fe pairs in beryl and blue color zoning variations

Although based on FEFF fitting of EXAFS data the probability of the Fe-Fe bond in the aquamarine crystal is smaller than the probability for the Fe-O path, it is present in all spots analyzed (Figs. 10a, b). The Fe-Fe peak in the graph of R (Å) *vs.* $|\chi(R)|(\text{Å}^{-3})$ is similar to that obtained in the only EXAFS study of aquamarine, in which in combination with XANES and EPR, Lin et al. (2013) provided the experimental evidence suggested in previous studies (Platonov et al., 1978, 1979a, b; Goldman et al., 1978; Groat et al., 2010) that the blue color in aquamarine is caused by IVCT between adjacent Fe^{3+}-Fe^{2+} pairs, with Fe^{3+} at the octahedral Al site and Fe^{2+} at its nearest 6g interstitial position. The best model of Lin et al. (2013) assumed the presence of Fe^{3+} at both the octahedral Al site and the 6g interstitial position, reproducing the five peaks they obtained in the spectrum and providing evidence to also support the occupancy of Fe at both sites.

The results of the EXAFS study suggesting the occurrence of Fe-Fe pairs in the zoned aquamarine expand those of the synchrotron-based XAS study of blue beryl by Bunnag et al.

(2020) that stated that the blue and light blue colors originate from Fe^{2+} residing in the channel sites, whereas the darker blue shade is due to IVCT between Fe^{2+} and Fe^{3+} in octahedral and interstitial sites. However, by synchrotron XANES and UV-Vis data they could not distinguish between the 6-fold coordinated Al^{3+} site and the 6g interstitial site within the aquamarine. Similarly, this EXAFS study allows the visualization of the Fe-Fe bond suggesting IVCT that the study by Groat et al. (2010) could not confirm as responsible for the blue color of beryl from the True Blue showing likely due to low Fe concentrations at the 6g site not detectable by structural techniques such as Mössbauer spectroscopy and single-crystal XRD and neutron diffraction analyses. Using optical absorption, studies of blue beryl from Brazil identified $^{VI}Fe^{2+}$ as causing a blue color that is enhanced by IVCT between $^{VI}Fe^{2+}$ and $^{6g}Fe^{3+}$, whereas in colorless beryl $^{Be}Fe^{2+}$ was reported to strongly predominate over $^{Al}Fe^{2+}$ (Taran et al., 2017; Taran & Vyshnevskyi, 2019). Similar findings were presented by earlier studies (e.g., Wood & Nassau, 1968; Goldman et al., 1978).

Based on the Fe-Fe FEFF fitting model with an Fe-Fe distance of 2.30 Å, the bond distances obtained for the Fe-Fe path between Fe pairs in all color zones of the zoned aquamarine crystal deviate towards shorter distances (2.066 – 2.151 Å) compared to the model value of 2.30 Å of Groat et al. (2010) and the ~2.5 Å length calculated by Lin et al. (2013) (Table 3). The longest distance (2.15 Å) was obtained for the Fe-Fe pair in the colorless zone, whereas for the other blue color zones the bond lengths obtained are shorter (2.07 to 2.11 Å) and overlap (Fig. 13; Tables 2, A1). Compared to Fe-Fe bond distances reported in previous studies in beryl and aquamarine obtained using a variety of techniques (Table 3; Dvir & Low, 1960; Edgar & Hutton 1982; Lin et al., 2013; Andersson, 2019), those obtained here tend to be mostly shorter. For example, Edgar and Hutton (1982) determined Fe-Fe distances in natural beryl

ranging from 2.57 to 2.76 Å and Andersson (2019) found Fe-Fe distances in beryl ranging from 2.55 to 2.76 Å. Lin et al. (2013) calculated the local structural environments of FeO_6 groups in blue beryl and obtained Fe-Fe atomic distances of 2.49 Å and 2.51 Å between Fe^{3+} in the Al octahedral site and Fe^{2+} in its nearest 6g position, and Fe^{2+} in the octahedral Al site and Fe^{3+} in the 6g interstitial site, respectively, which are longer than in the model structure used of blue beryl from the True Blue Showing, Canada (~2.3 Å).

It is known that the distance between the Fe atoms in Fe pairs in beryl is a critical factor in determining the coloration of aquamarine, including the intensity and hue of the blue color (Dvir & Low, 1960; Loeffler & Burns, 1976; Groat et al., 2010; Lin et al., 2013). A longer Fe-Fe distance in the clear beryl zone compared to shorter Fe-Fe distances in the light, medium, and darker blue beryl of the zoned aquamarine is consistent with previous studies that show that shorter distances between Fe pairs are expected to result in a more intense blue color (e.g., Loeffler & Burns, 1976;), whereas a longer distance may lead to a greenish hue (Groat et al., 2010). Because the exact blue color of the aquamarine studied by Lin et al. (2013) is unknown, it is unclear why the Fe-Fe distances calculated are longer than 2.3 Å, but they are within others reported. It is also still unclear why the distances obtained in the present study are shorter than those of Groat et al. (2010), but it is likely that variations in the amount of Fe^{3+} and Fe^{2+} in the Al and 6g sites in aquamarine crystals or color zones produce different distortions of the octahedra that can result in blue color variants. However, it is possible that the FEFF path used for the model does not fully represent the data since the 6g interstitial site has been challenging to quantify in previous studies (Groat et al., 2010; Lin et al., 2013; Bunnag et al., 2020). Nonetheless, the EXAFS data showing Fe-Fe pairs present in all colors of the zoned aquamarine with bond length shorter in the colorless/very light blue zone than in the darker blue zones

supports studies indicating IVCT transitions between Fe atoms darken (blue) color in beryl (e.g., Dvir & Low, 1960; Goldman et al., 1978).

Relationship between Fe K-Edge pre-edge and EXAFS parameters and color variations

A comparison of bond lengths obtained from EXAFS parameters and pre-edge XAS parameters of the aquamarine crystal shows a slight negative correlation between the pre-edge integrated intensity and the Fe-Fe bond distance ($R^2 = 0.4872$; Fig. 13a), with the colorless spot having the lowest integrated intensity and longest bond length (R = 2.1510 Å) between Fe in the Al site and Fe within the interstitial 6g position. In contrast, two dark blue spots have the shortest Fe-Fe bond length (R = 2.0663 Å and 2.0715 Å) and some of the highest integrated intensity values, but another darker blue spot has a higher bond distance and the highest integrated intensity (Table A1). This suggests an overall different coordination environment of Fe atoms and bond lengths in the octahedral and 6g site in the colorless zone compared to Fe in the darker blue zones in the crystal, which may be responsible for the observed color differences. The darker blue zones having a shorter Fe-Fe bond length also align with these zones having more Fe^{3+}, which is discussed below. These findings are in line with studies by Groat et al. (2010), Lin et al. (2013), and Bunnag et al. (2020) that reported Fe coordination environments for blue aquamarine crystals showing predominantly octahedral coordination.

A similar slight negative correlation is observed between the Fe-Fe bond length with Fe intensity and with fit centroid (Fig. 13b, c; $R^2 = 0.396$ and $R^2 = 0.3835$, respectively). The colorless spot with its long Fe-Fe bond length also has the lowest Fe intensity and fit centroid energy. In contrast, the other blue spot analyses have shorter bond lengths, with the dark blue spots having the highest Fe intensity and fit centroid energy. Combined, these findings suggest

that higher Fe contents are associated with a higher centroid approximated to higher Fe^{3+}/Fe_{tot} ratios that define shorter Fe-Fe distances generating darker blue colors due to effective IVCT. However, with the EXAFS data obtained, differences in Fe-Fe bond length related to blue color variations between light and darker blue cannot be resolved and further studies are needed. Understanding Fe coordination environments provides insights into the coloration of aquamarine, which has important implications for the gemstone industry. Further, it can be used to understand the formation processes of varieties of aquamarine in different geologic environments.

CONCLUSIONS

To the best of our knowledge, the present is the first synchrotron-based combined Fe K-edge XAS and EXAFS and micro-XRF study of beryl, and it demonstrates consistent intra-crystal blue color variations in an aquamarine crystal from clear to light blue to medium blue to darker blue with obtained magnitudes of parameters and elemental abundances. Detailed synchrotron micro-XRF chemical maps within four color zones of the aquamarine crystal reveal delicate (1 mm) chemical zoning in Fe (and Mn, Cr, and V) contents that match visible color changes from colorless to pale blue, medium blue, and darker blue. The strong correlation between darkening of the blue color and Fe intensity, not seen for Cr, Mn, and V, indicates that Fe is the main chromophore in aquamarine.

The results of synchrotron Fe K-edge XAS pre-edge centroid energies and integrated intensities of the different blue colored zones in the aquamarine crystal indicate the presence of both Fe^{2+} and Fe^{3+} in octahedral coordination. The colorless zone is characterized by the lowest

centroid energy and Fe intensity, representing the lowest Fe^{3+}/Fe_{Tot} ratio and mostly the presence of octahedral Fe^{2+}. Increasing centroid energy with darkening of the blue color is best correlated with the amplitude of P2 and less with that of P1, suggesting that the size of the higher energy peak, thought to represent $^{VI}Fe^{3+}$, is related to the darkening of the blue color.

Considering the high centroid of red beryl representing $^{VI}Fe^{3+}$, the lowest centroid in the clear-light blue zone of the aquamarine crystal represents the lowest Fe^{3+}/Fe^{2+} ratio and higher $^{VI}Fe^{2+}$ content. Increasing centroid energy correlates with the darkening of the blue color within the aquamarine crystal, suggesting a correlation between higher Fe^{3+}/Fe_{Tot} and the darkening of the blue color. Variations measured in total Fe in the zoned aquamarine are likely to correspond to increasing amounts of octahedral Fe^{3+} incorporated in the crystal structure, and as a result increasing average Fe^{3+}/Fe^{2+} ratios, from clear to darker blue beryl zones.

Based on EXAFS modeling, Fe occurs mostly as ^{VI}Fe replacing Al in all color zones, with no consistent differences in Fe-O bond distances (1.91-1.97 Å) identified among the different blue color zones. EXAFS fitting modeling shows a low probability of Fe occurring as Fe-Fe pairs in the octahedral 6g position and Al site (^{VI}Fe-^{6g}Fe) in all blue color zones analyzed compared to Fe being present as isolated ^{VI}Fe iron atoms, but their occurrence corroborates the role of IVCT as a mechanism in generating or enhancing the blue color in aquamarine. A longer Fe-Fe bond distance obtained for the clear-light blue to colorless zone (2.15 Å) compared to shorter distances for the various darker blue color zones (2.07 to 2.11 Å) confirms that shorter Fe-Fe atomic distances in the darker blue colors are responsible for effective IVCT darkening the blue color of aquamarine. The colorless spot with its long Fe-Fe bond length also has the lowest Fe intensity and fit centroid energy. In contrast, the other blue spot analyses have shorter bond lengths, with the dark blue spots having the highest Fe intensity and fit centroid energy.

Combined, these findings suggest that higher Fe contents are associated with a higher centroid approximated to higher Fe^{3+}/Fe_{tot} ratios that define shorter Fe-Fe distances generating darker blue colors due to effective IVCT.

At the time of writing this paper, this is the first study combining synchrotron-based XAS and micro-XRF analysis of blue beryl and the first study presenting detailed Fe chemical maps in a zoned aquamarine to visualize and explain quantitatively the relationship between Fe contents, XAS and EXAFS parameters indicative of coordination geometry of Fe, relative oxidation state (Fe^{3+}/Fe_{Tot}) of Fe, and bond distances and blue color variation in a single crystal. Additional XAS and EXASFS studies are needed to corroborate the relationships obtained in this study. Characterizing the local atomic structure of Fe in aquamarine and its link with color provides insights into the origin of the blue color variations in beryl as a key gemstone-defining characteristic, which can aid in the treatment process. Further, fingerprinting these physical-chemical properties and beryl's natural atomic environment in general may prove useful in gemology and in the processing of the critical metal beryllium. Overall, these findings contribute to our understanding of beryl's electronic and crystallographic properties and provide important insights for future studies on this and other minerals with similar structures.

ACKNOWLEDGEMENTS

Funding for this study was provided by an East Carolina University Harriot College of Arts and Sciences Research Initiation Grant (to AHR). Beryl samples 86394 and 131716 were provided on loan by the Mineralogical and Geological Museum at Harvard University. This research used resources of the Advanced Photon Source (APS), a U.S. Department of Energy

(DOE) Office of Science User Facility operated for the DOE Office of Science by Argonne National Laboratory under Contract No. DE-AC02-06CH11357. This work was performed at GeoSoilEnviroCARS (GSECARS), The University of Chicago, Sector 13 of the APS, Argonne National Laboratory, IL, and supported by Drs. Tony Lanzirotti and Matt Newville. GSECARS (Sector 13) is supported by the NSF (grant # EAR-1634415) and the U.S. Department of Energy (DOE, grant # DE-FG02-94ER14466). Discussions with Darby Dyar, Elizabeth Cottrelle, and Yuanming Pan are greatly appreciated.

REFERENCES

Adamo, I., Pavese, A., Prosperi, L., Diella, V., Ajò, D., Gatta, G.D., & Smith, C.P., 2008. Aquamarine, Maxixe-type (irradiated) beryl, and hydrothermal synthetic blue beryl: Analysis and identification. Gems & Gemology, 44, 3, 214-226.

Andersson, L.O., 1979. The difference between Maxixe beryl and Maxixe-type beryl: An electron Paramagnetic resonance investigation. Journal of Gemology, 16, 5, 313-317.

Andersson, L.O., 2006. The positions of H^+, Li^+, and Na^+ impurities in beryl. Physics and Chemistry of Minerals, 33, 403-416.

Andersson, L.O., 2013. The yellow color center and trapped electrons in beryl. The Canadian Mineralogist, 51, 1, 15-25. doi:10.3749/canmin.51.1.15.

Andersson, L.O., 2019. Comments on beryl colors and on other observations regarding iron-containing beryls1. The Canadian Mineralogist, 57, 4, 551-566. https://doi.org/10.3749/canmin.1900021.

Arletti, R., Vezzalini, G., Quartieri, S., Ferrari, D., Merlini, M., & Cotte, M., 2008. Polychrome glass from Etruscan sites: first non-destructive characterization with synchrotron μ-XRF, μ-XANES and XRPD. Applied Physics A, 10.1007/s00339-008-4462-x.

Arrio, M.-A., Rossano, S., Brouder, C., Galoisy, L., & Calas, G., 2000. Calculation of multipole transitions at the Fe K pre-edge through p-d hybridization in the Ligand Field Multiplet model. Europhysics Letters, 51, 4, 454-460.

Artioli, G., Rinaldi, R., Stahl, K., & Zanazzi, P.F., 1993. Structure refinements of beryl by single-crystal neutron and X-ray diffraction. American Mineralogist, 78, 762-768.

Aurisicchio, C., Franzini, M., Grubessi, O., & Zanazzi, P.F., 1988. Reappraisal of the crystal chemistry of beryl. American Mineralogist, 73, 826-837.

Aurisicchio, C., Grubessi, O., & Zecchini, P., 1994. Infrared spectroscopy and crystal chemistry of the beryl group. The Canadian Mineralogist, 32, 55-68.

Bačík, P., & Fridrichová, J., 2019. The site occupancy assessment in beryl based on bond-length constraints. Minerals, 9, 641, 1-14.

Bajt, S., Sutton, S.R., & Delaney, J.S., 1994. X-ray microprobe analysis of iron oxidation states in silicates and oxides using X-ray absorption near edge structure (XANES). Geochimica et Cosmochimica Acta, 58, 23, 5209-5214.

Barton, C.C., & Young, S.W., 2002. Aquamarine from the Baha'i region, Madagascar. Journal of Gemology, 28, 5-6, 283-294.

Berry, A., O'Neill, H., Jayasuriya, K., Campbell, S., & Foran, G., 2003. XANES calibrations for the oxidation state of iron in a silicate glass. American Mineralogist, 88, 7, 967-977.

Blak, A.R., Isotani, S., & Watanabe, S., 1983. Optical absorption and electron spin resonance in blue and green natural beryl: A reply. Physics and Chemistry of Minerals, 9, 4, 279-280.

Bonnin-Mosbah, M., Métrich, N., Susini, J., Salomé, M., Massare, D., & Menez, B., 2002. Micro-X-ray absorption near edge structure at sulphur and iron K-edges in natural silicate glasses. Spectrochimica Acta B, 57, 711 – 725.

Bragg, W.L., & West, J., 1924. The structure of beryl and the general characteristics of covalent bonds. Proceedings of the Royal Society of London. Series A, Containing Papers of a Mathematical and Physical Character, 106, 738, 678-697.

Bunnag, N., Kasri, B., Setwong, W., Sirisurawong, E., Chotsawat, M., Chirawatkul, P., & Saiyasombat, C., 2020. Study of Fe ions in aquamarine and the effect of dichroism as seen using UV–Vis, NIR and x-ray. Radiation Physics and Chemistry, 177, 109107.

Cassedanne, J., & Philippo, S., 2015. Minerals and Gem Deposits of the Eastern Brazilian Pegmatites (Vol. 1). Luxembourg: Musée National d'Histoire Naturelle Luxembourg, 6, 429-442.

Chankhantha, C., Thanasuthipitak, P., & Kidkhunthod, P., 2016. Iron K-edge XANES study of heated green beryl from Madagascar. Walailak Journal of Science & Tech,nology, 13, 977-983.

Delaney, J.S., Dyar, M.D., Sutton, S.R., & Bajt, S., 1998. Redox ratios with relevant resolution: Solving an old problem by using the synchrotron microXANES probe. Geology, 26, 2, 139-142. doi:10.1130/0091-7613(1998)026<0139:RRWRRS>2.3.CO;2.

Dvir, M., & Low, W., 1960. Paramagnetic resonance and optical spectrum of iron in beryl. Physical Review 119, 5, 1587-1591.

Dyar, M., Lowe, E., Guidotti, C., & Delaney, J., 2002a. Fe^{3+} and Fe^{2+} partitioning among silicates in metapelites: A synchrotron micro-XANES study. American Mineralogist, 87, 4, 514-522.

Dyar, M.D., Gunter, M.E., Delaney, J.S., Lanzirotti, A., & Sutton, S.R., 2002b. Systematics in the structure and XANES spectra of pyroxenes, amphiboles, and micas as derived from oriented single crystals. The Canadian Mineralogist, 40, 5, 1375-1393.

Dyar, M., Breves, E., Gunter, M., Lanzirotti, A., Tucker, J., Carey, C., Peel, S., Brown, E., Oberti, R., Lerotic, M., & Delaney, J., 2016. Use of multivariate analysis for synchrotron micro-XANES analysis of iron valence state in amphiboles. American Mineralogist, 101, 5, 1171-1189.

Edgar, A. & Hutton, D.R., 1982. Exchange-coupled pairs of Fe^{3+} ions in beryl. Solid State Communications, 41, 2, 195-198.

Eeckhout, S., Neisius, T., & Castañeda, C., 2005. Oxidation effects in beryl induced by synchrotron radiation. Nuclear Instruments and Methods in Physics Research section B: Beam Interactions with Materials and Atoms, 229, 1, 73-77.

Evans, K., Dyar, M., Reddy, S., Lanzirotti, A., Adams, D., & Tailby, N., 2014. Variation in XANES in biotite as a function of orientation, crystal composition, and metamorphic history. American Mineralogist, 99, 2-3, 443-457.

Executive Office of the President. 2017. A Federal Strategy to Ensure Secure and Reliable Supplies of Critical Minerals. Federal Register 82, 246: 60835-60837. Accessed February 14, 2022.

Farges, F., Lefre`re, Y., Rossano, S., Berthereau, A., Calas, G., & Brown Jr., G.E., 2004. The effect of redox state on the local structural environment of iron in silicate glasses: A combined XAFS spectroscopy, molecular dynamics, and bond valence study. Journal of Non-Crystalline Solids, 344, 1-2, 176–188. doi:10.1016/j.jnoncrysol.2004.07.050.

Fiege, A., Ruprecht, P., Simon, A., Bell, A., Göttlicher, J., Newville, M., Lanzirotti, T., Moore, G., 2017. Calibration of Fe XANES for high-precision determination of Fe oxidation state in glasses: Comparison of new and existing results obtained at different synchrotron radiation sources. American Mineralogist, 102, 2, 369-380.

Figueiredo, M.O., Silva, T., Veiga, J.P., Gomes, C., De Andrade, V., 2008. The blue coloring of beryls from Licungo, Mozambique: An X-ray absorption spectroscopy study at the iron K-edge. Mineralogical Magazine, 72, 175-178.

Fritsch, E., & Rossman, G.R., 1988. An Update on Color in Gems. Part 2: Colors Involving Multiple Atoms and Color Centers. Gems & Gemology, 24, 1, 3-15.

Gibbs, G.V., Breck, D.W., & Meagher, E.P., 1968. Structural refinement of hydrous and anhydrous synthetic beryl, $Al_2(Be_3Si_6)O_{18}$ and emerald, $Al_{1.9}Cr_{0.1}(Be_3Si_6)O_{18}$. Lithos, 1. 3, 275-285. https://doi.org/10.1016/S0024-4937(68)80044-1.

Giuli, G., Pratesi, G., Cipriani, C., & Paris, E., 2002. Iron local structure in tektites and impact glasses by extended X-ray absorption fine structure and high-resolution X-ray absorption near-edge structure spectroscopy. Geochimica et Cosmochimica Acta, 66, 24, 4347-4353.

Goldman, D.S., Rossman, G.R., & Parkin, K.M., 1978. Channel constituents in beryl. Physics and Chemistry of Minerals, 3, 3, 225-235. doi:10.1007/BF00307535.

Grew, E.S., 2002. Mineralogy, Petrology, and Geochemistry of Beryllium: An introduction and list of beryllium minerals. Reviews in Mineralogy and Geochemistry, 50, 1, 1-76.

Groat, L.A., Hart, C., Lewis, L., & Neufeld, H., 2005. Emerald and aquamarine mineralization in Canada. Geoscience Canada, 32, 2, 65-76.

Groat, L.A., Rossman, G.R., Dyar, M.D., Turner, D., Piccoli, P.M.B., Schultz, A. J., & Ottolini, L., 2010. Crystal chemistry of dark blue aquamarine from the True Blue showing, Yukon Territory, Canada. The Canadian Mineralogist, 48(3), 597-613. doi:10.3749/canmin.48.3.597.

Ingall, E.D., Brandes, J.A., Diaz, J.M., de Jonge, M.D., Paterson, D., McNulty, I., Elliotte, W. C., & Northrup, P., 2011. Phosphorus K-edge XANES spectroscopy of mineral standards. Journal of Synchrotron Radiation, 18, 2, 189–197. https://doi.org/10.1107/S0909049510045322.

Jheeta, K.S., & Jain, D.C., 2007. Investigation of coordination geometry around iron in annealed sapphire (Al_2O_3) using PL, XRD, XAS, and FTIR techniques. African Physical Review, 1, 2, 56-66 http://www.aphysrev.org/index.php/aphysrev/article/viewFile/36/13.

Lin, J., Chen, N., Huang, D., & Pan, Y., 2013. Iron pairs in beryl: New insights from electron paramagnetic resonance, synchrotron X-ray absorption spectroscopy, and ab initio calculations. American Mineralogist, 98, 10, 1745-1753.

Loeffler, B.M., & Burns, R.G., 1976. Shedding light on the color of gems and minerals: The selective absorption of light according to wavelength—the result of various electronic processes whose energies correspond to certain wavelengths of visible light—gives minerals their distinctive hues. American Scientist, 64, 6, 636-647.

Mathew, G., Karanth, R.V., Gundu Rao, T.K., & Deshpande, R.S., 2000. Colouration in natural Beryls: A Spectroscopic investigation. Journal of the Geological Society of India, 56, 9, 2000, 285-303.

Morosin, B. 1972. Refinement of the crystal structure of beryl. Acta Crystallographica Section B, 28(1), 79-83.

Newville, M., 2004. Fundamentals of XAFS. Consortium for Advanced Radiation Sources, 1-37.

Newville, M., 2013. Larch: An analysis package for XAFS and related spectroscopies. Journal of Physics. Conference Series, 430:012007.

Penner-Hahn, J.E., 2003. X-ray Absorption Spectroscopy. Journal of Synchrotron Radiation, 2, 13, 159-182.

Platonov, A.N., Taran, M.N., Minko, O.E., & Polshyn, E.V., 1978. Optical absorption spectra and nature of color of iron-containing beryls. Physics & Chemistry of Minerals, 3, 87–88.

Platonov, A.N., Taran, M.N., & Polshin, E.V., 1979a. On the forms of iron in beryls. Zap Vses Miner Obsch, 6, 725–730. In Russian.

Platonov, A.N., Taran, M.N., Polshin, E.V., & Minko, O.E., 1979b. On nature of color of iron-bearing beryls. Izv AN SSR Ser Geol 10, 54–68. In Russian.

Platonov, A.N., Khomenko, V.M., & Taran, M.N., 2016. Crystal chemistry, optical spectra and color of beryl. I. Heliodor and golden beryl — two varieties of natural yellow beryl. Mineralogical Journal, 38, 2, 3-14. https://doi.org/10.15407/mineraljournal.38.02.003. In Russian.

Preinfalk, Kostitsyn, Y., & Morteani, G., 2002. The Pegmatites of the Nova Era-Itabira-Ferros pegmatite district and the emerald mineralisation of Capoeirana and Belmont (Minas Gerais, Brazil): geochemistry and Rb-Sr dating. Journal of South American Earth Sciences, 14, 867-887.

Price, D.C., Vance, E.R., Smith, G., Edgar, A., & Dickson, B.L., 1976. Mössbauer effect studies of beryl1. Le Journal de Physique Colloques, 37, C6, 811-817. https://doi.org/10.1051/jphys col:19766 171.

Proctor, K., 1984. Gem pegmatites of Minas Gerais, Brazil: Exploration, occurrence, and aquamarine deposits. Gems & Gemology, 7, 78-100.

Quartieri, S., Riccardi, M.P., Messiga, B., & Boscherini, F., 2005. The ancient glass production of the Medieval Val Gargassa glasshouse: Fe and Mn XANES study. Journal of Non-Crystalline Solids, 351, 3013-3022. https://doi.org/10.1016/j.jnoncrysol.2005.06.046.

Shang, Y., Guo, Y., & Tang, J., 2022. Spectroscopy and chromaticity characterization of yellow to light-blue iron-containing beryl. Scientific Reports, 12(10765). https://doi.org/10.1038/s41598-022-11916-z.

Shigley, J.E., & Foord, E.E., 1984. Gem-quality red beryl from the Wah Wah Mountains, Utah. Gems & Gemology, Vol. 20, 4, 208–221.

Spinolo, G., Fontana, I., & Galli, A., 2007. Optical absorption spectra of Fe^{2+} and Fe^{3+} in beryl crystals. Physica Status Solidi (b), 244, 12, 4660-4668. https://doi.org/10.1002/pssb.200743102.

Taran, M.N., & Rossman, G.R., 2001. Optical spectroscopic study of tuhualite and a re-examination of the beryl, cordierite, and osumilite spectra. American Mineralogist, 86, 9, 973-980.

Taran, M.N., Dyar, M.D., Khomenko, V.M., & Boesenberg, J.S., 2018. Spectroscopic study of synthetic hydrothermal Fe^{3+} bearing beryl. Physics and Chemistry of Minerals, 45, 4, 489-496. https://doi.org/10.1007/s00269-017-0936-8.

Taran, M.N., & Vyshnevskyi, O.A., 2019. Be, Fe^{2+}-substitution in natural beryl: an optical absorption spectroscopy study12. Physics and Chemistry of Minerals, 46, 7, 795-806. https://doi.org/10.1007/s00269-019-01040-2.

U.S. Geological Survey, 2021. Mineral commodities summaries: Beryllium, https://pubs.usgs.gov/periodicals/mcs2021/mcs2021-beryllium.pdf. 2 pp. Last accessed March 11, 2022.

Viana, R.R., da Costa, G.M., De Grave, E., Jordt-Evangelista, H., & Stern, W.B., 2002. Characterization of beryl (aquamarine variety) by Mössbauer spectroscopy. Physics and Chemistry of Minerals, 29(1), 78-86. doi:10.1007/s002690100210.

Villain, O., Calas, G., Galoisy, L., Cormier, L., & Hazemann, J.L., 2007. XANES determination of chromium oxidation states in glasses: comparison with optical absorption spectroscopy. Journal of the American Ceramic Society, 90, 11, 3578-3581.

Waychunas, G.A., Apted, M.J., & Brown, G.E., Jr., 1983. X-ray k-edge absorption spectra of Fe minerals and model compounds: near-edge structure. Physics and Chemistry of Minerals, 10(1), 1-9.

Wenk, H.R., & Bulakh, A.G., 2004. Minerals: Their constitution and origin. Cambridge, Cambridge University Press.

Westre, T.E., Kennepohl, P., DeWitt, J.G., Hedman, B., Hodgson, K.O., & Solomon, E.I., 1997. A Multiplet Analysis of Fe K-Edge 1s → 3d Pre-Edge Features of Iron Complexes. Journal of the American Chemical Society, 119, 27, 6297-6314. doi:10.1021/ja964352a.

Wilke, M., Farges, F., Petit, P.-E., Brown, G.E. Jr., & Martin, F., 2001. Oxidation state and coordination of Fe in minerals: An Fe K-XANES spectroscopic study. American Mineralogist, 86 (7-8), 714-730.

Wood, D.L., & Nassau, K., 1968. The characterization of beryl and emerald by visible and infrared absorption spectroscopy. The American Mineralogist, 53, 5-6, 777-800.

FIGURES

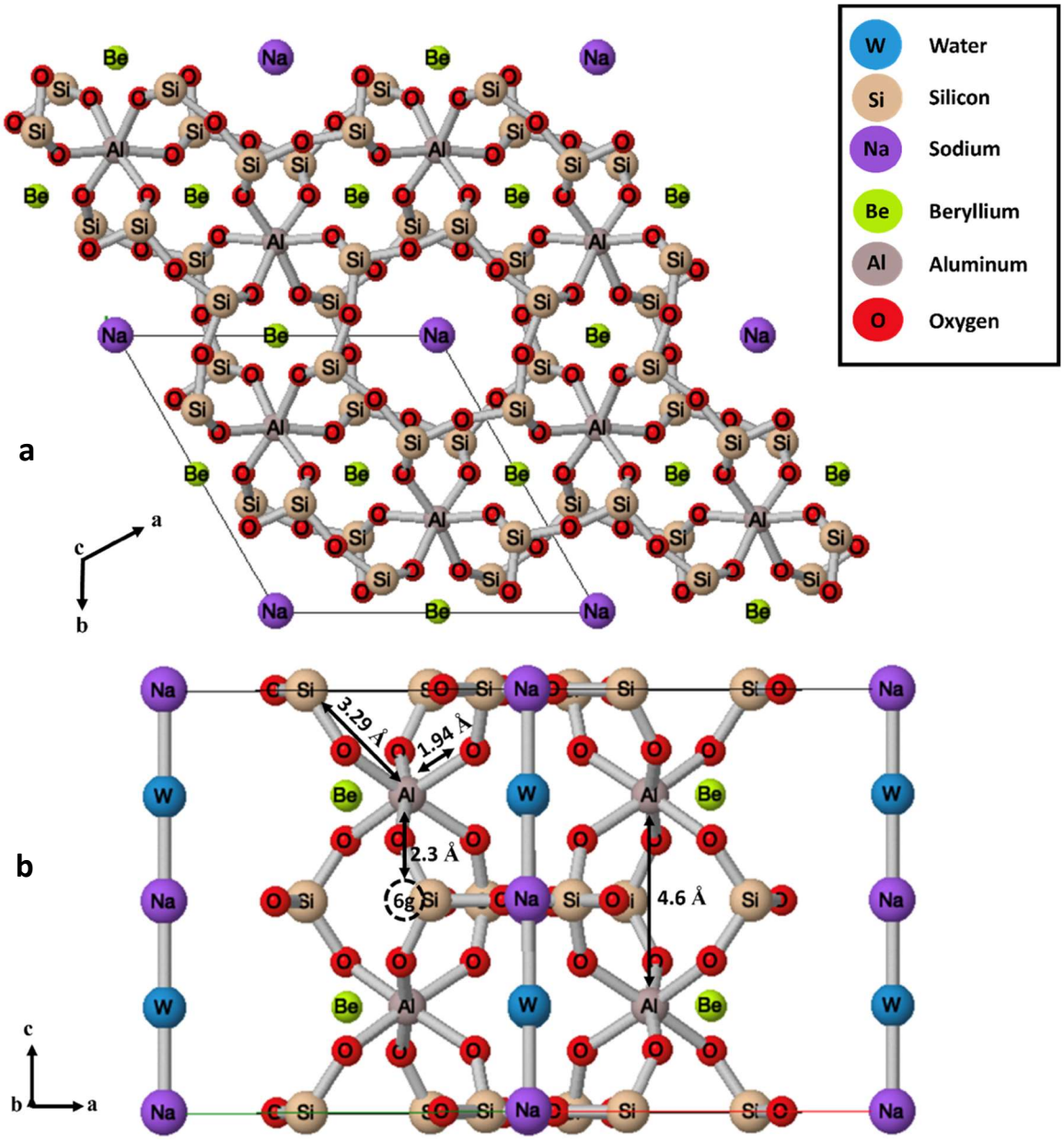

Figure 1. Atomic structure of beryl looking down: **a.** the c axis of the basal plane and showing the 6-membered silicate rings forming channels. **b.** the b axis illustrating the 6g interstitial position between two octahedral Al sites along the c axis. Be (green) and Si (light tan) are shown in their tetrahedral site and Al (brown) in its octahedral coordination. Water (W) molecules (blue) and Na (purple) are shown in the channels. Images generated in Mindat.org.

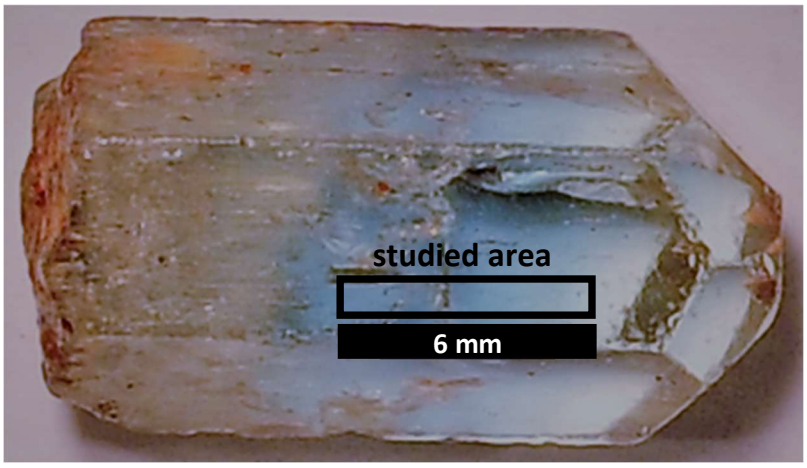

Figure 2. Zoned aquamarine crystal used for the synchrotron-based Fe K-edge XAS and XRF study showing color zoning from right to left from clear to light blue, darker blue, and medium blue. Sample 86394, Minas Gerais, Brazil, Geological and Mineralogical Museum, Harvard University

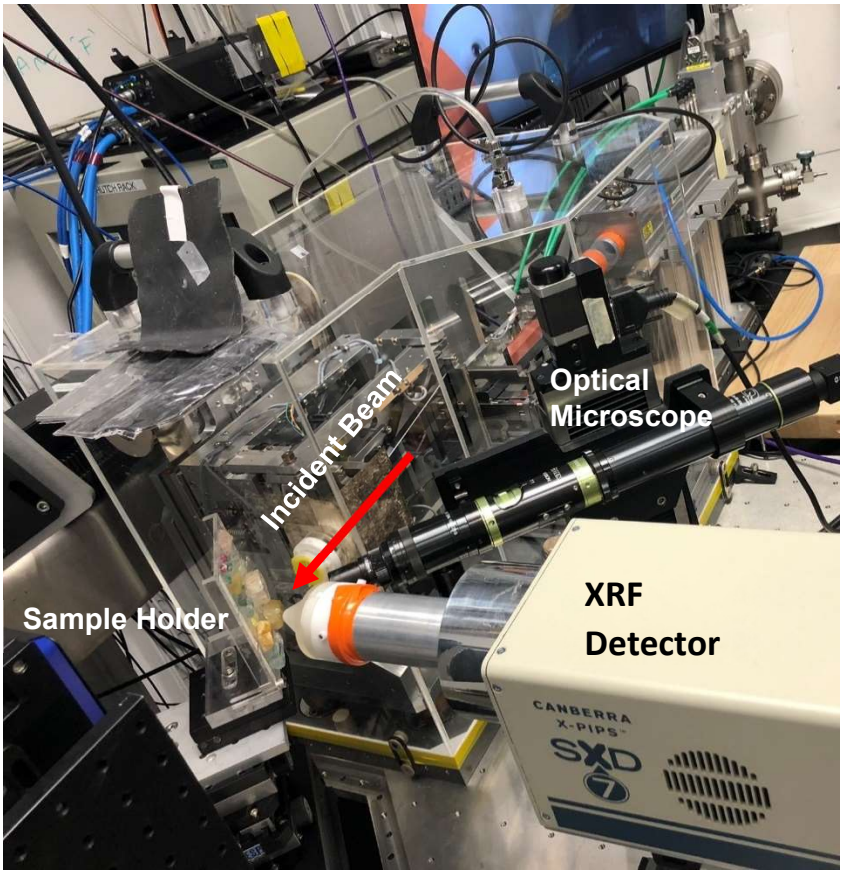

Figure 3. Sample stage setup with crystals oriented horizontally with their c axis at 45° to the direction of the incident X-ray beam. Advanced Photon Source synchrotron facility, Argonne National Lab, IL, where micro-XAS and XRF experiments were conducted.

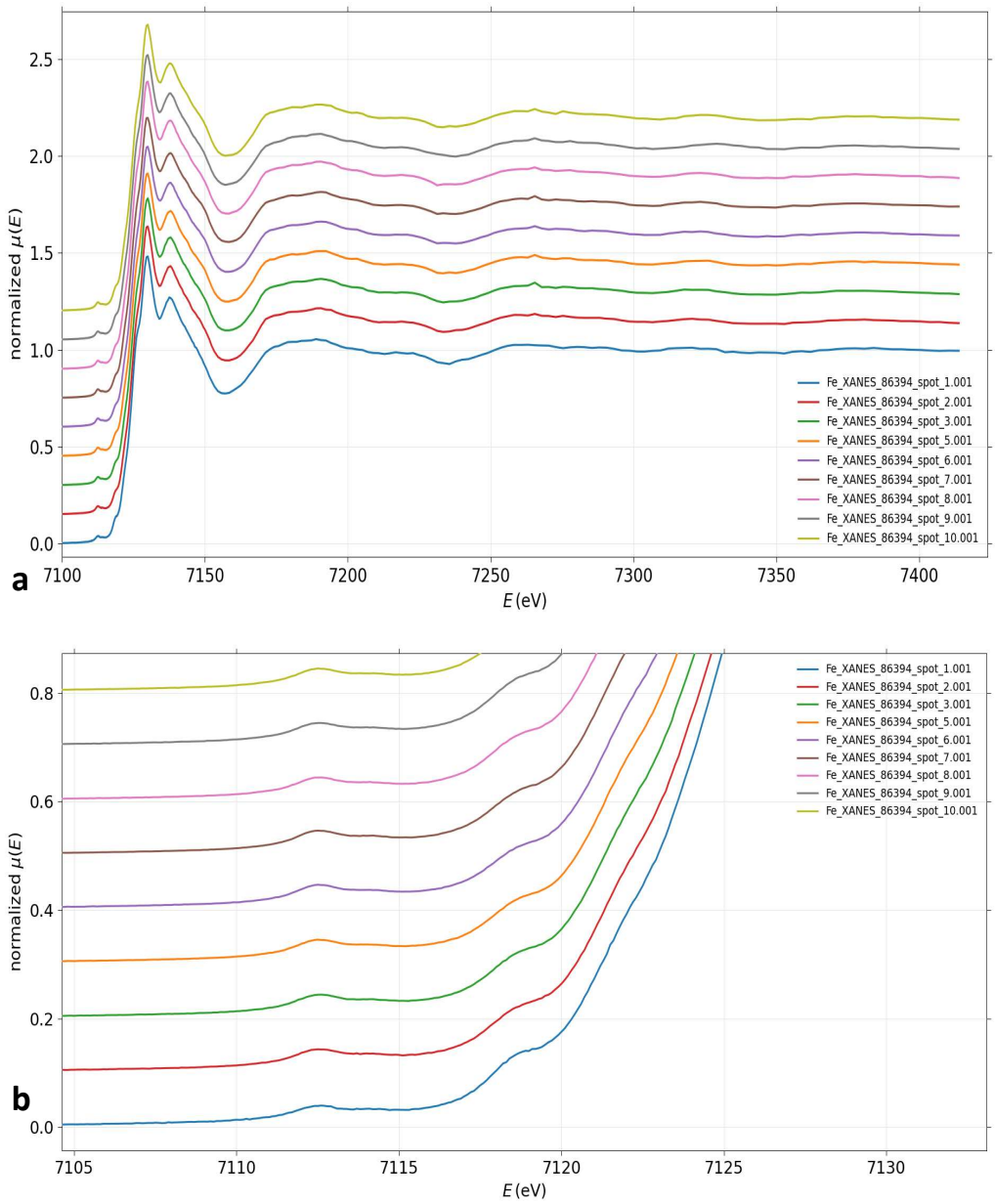

Figure 4. Graph of normalized absorption μ(E) (arbitrary units) *vs.* Energy (eV) with background subtracted for the nine XAS analyses of the zoned aquamarine crystal showing: **a.** The full energy range of the raw data spectra with analyses offset for visualization. **b.** Zoomed in view of the pre-edge area of the normalized spectrum.

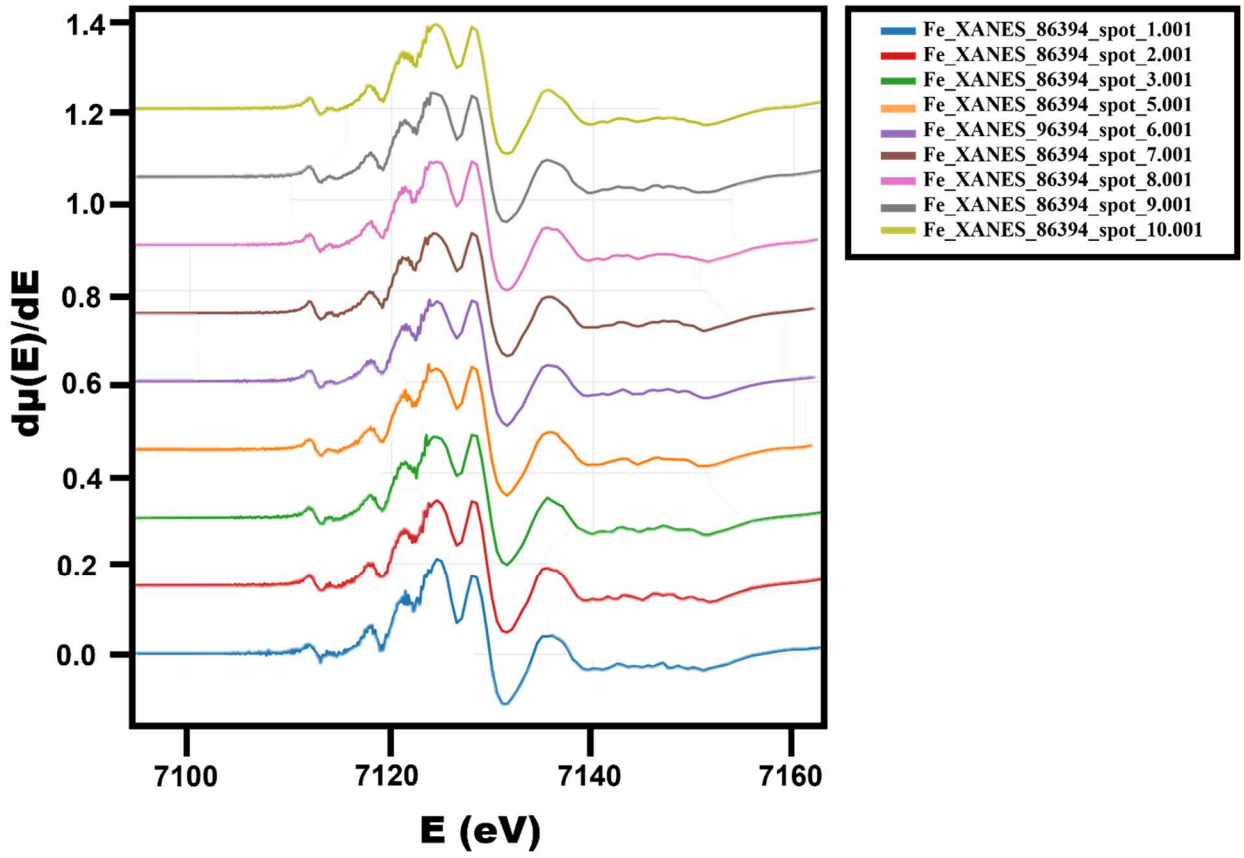

Figure 5. Graph of first derivative of the normalized absorption dμ(E)/dE (arbitrary units) *vs.* Energy (eV) for the Fe XAS analyses of the zoned aquamarine crystal showing the spectra of the XANES area at an energy range of 30 eV below the edge (E_0) and 30 eV above the edge. Note the major feature before the edge has two components (peaks) for all analyses, with the low energy peak considerably higher for the clear zone of the crystal (spot 1) compared to the darker blue zones (spots 2-10).

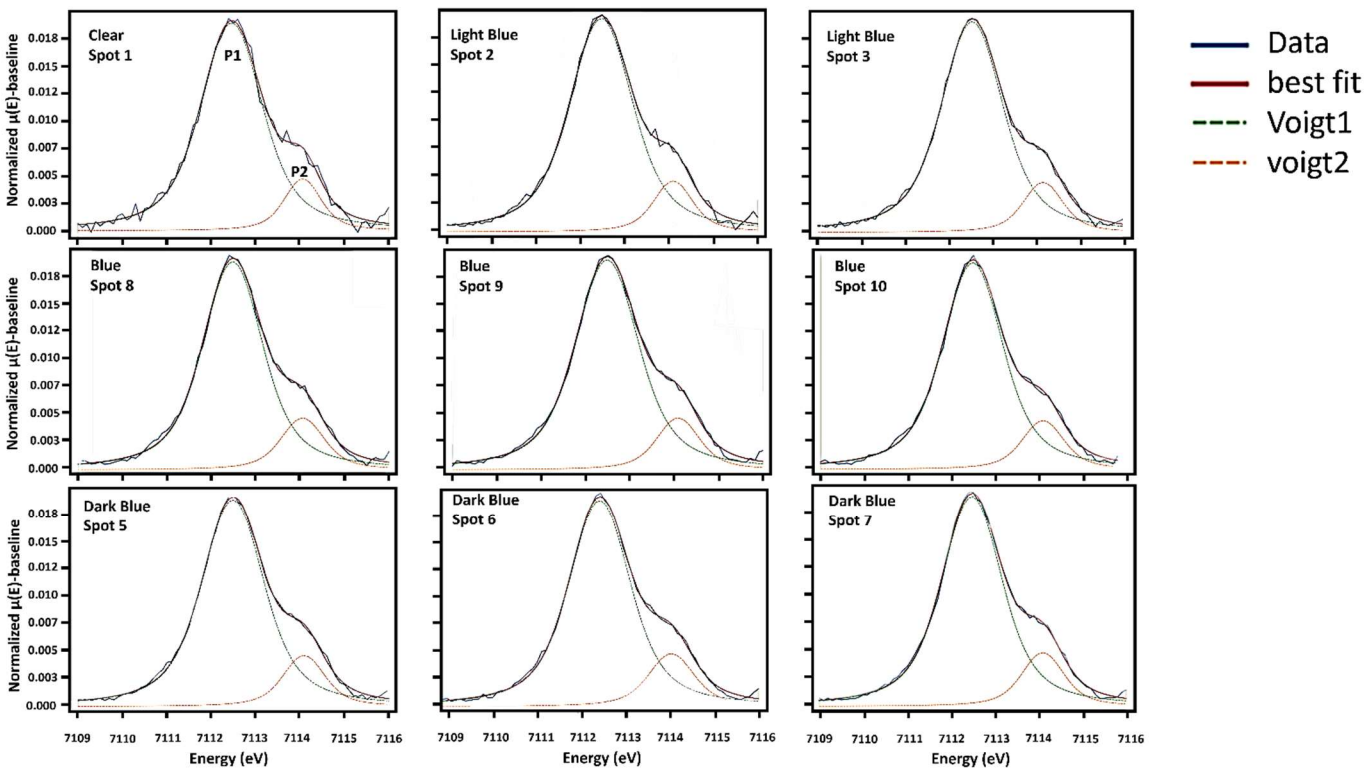

Figure 6. Graphs of normalized μ(E) with baseline subtracted *vs.* Energy (eV) for Fe K-edge XAS pre-edge analyses of the zoned aquamarine crystal deconvoluted by two Voigt components. Numbers shown correspond to spot analyses. P1 (Voigt1) and P2 (Voigt2) are the two pre-edge peaks observed in the spectrum.

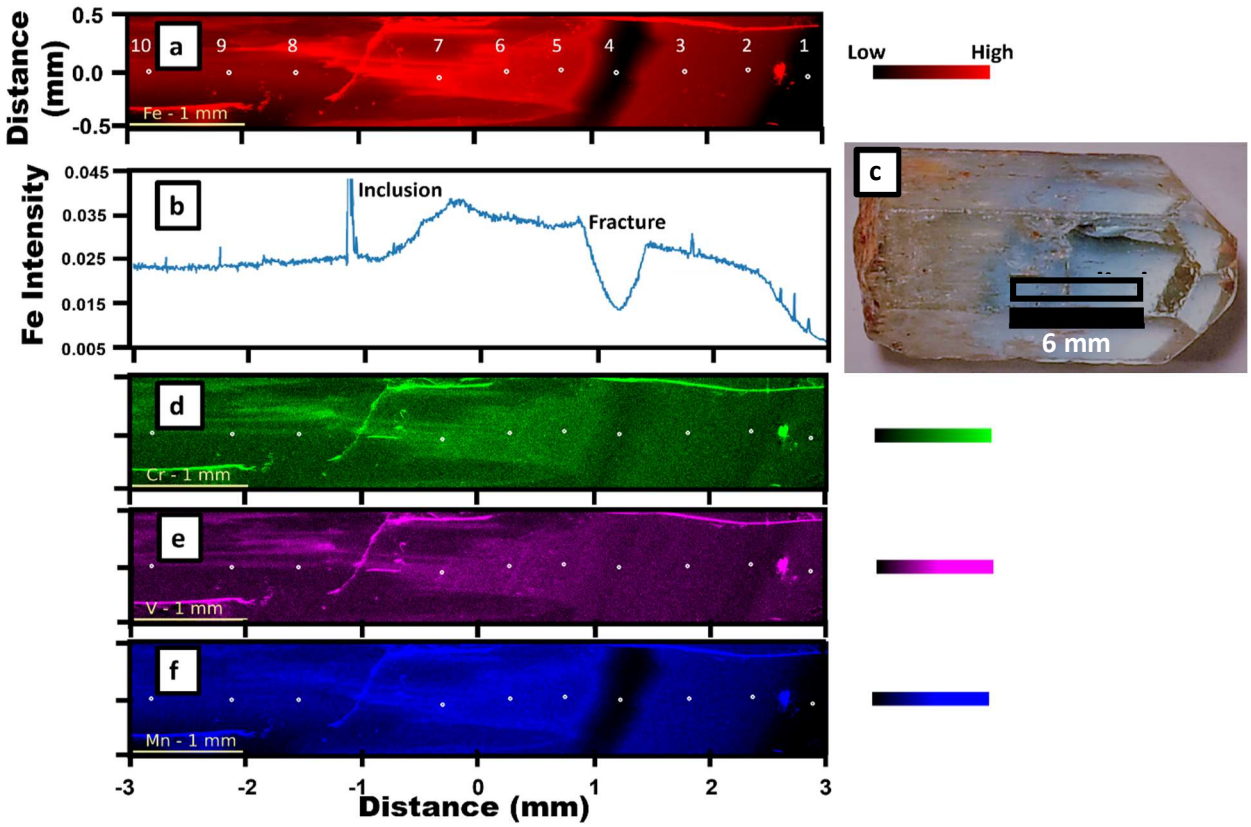

Figure 7. Results of synchrotron micro-XRF spectroscopy of the zoned aquamarine crystal showing: **a.** Fe chemical map of studied area. **b.** X-slice of Fe intensity (counts) ***vs.*** distance (mm). **c.** Zoned Aquamarine crystal with 6 x 1 mm rectangle of studied area. **d.** Cr chemical map. **e.** V chemical map. **f.** Mn chemical map. The bars to the right represent the intensity scale from low (black, dark) to high (bright, light). Numbered spots within the crystal correspond to XAS analyses.

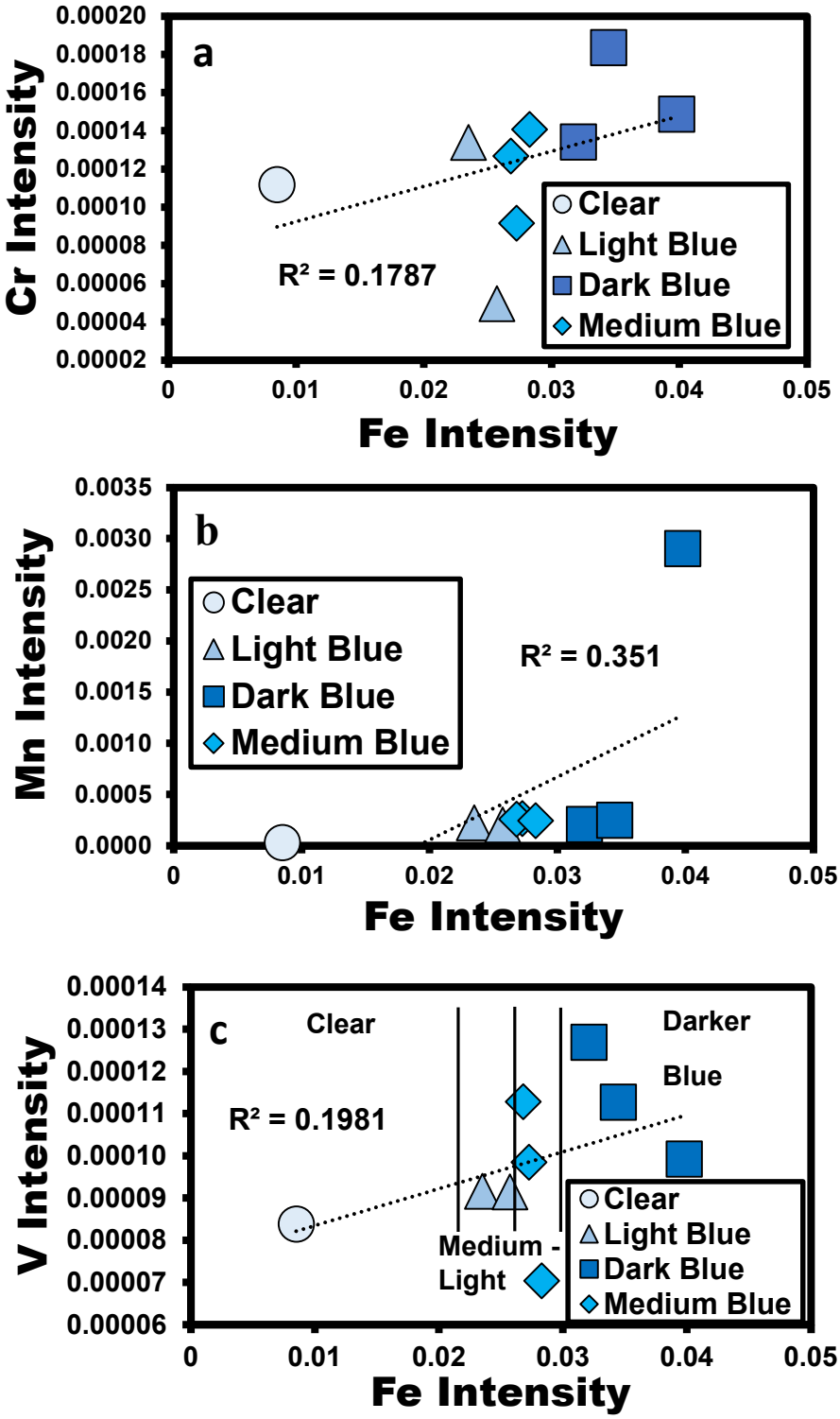

Figure 8. Binary plots showing the relationship between elemental intensities (counts) derived from micro-XRF chemical maps in the zoned aquamarine crystal. **a.** Fe *vs.* Cr intensity. **b.** Fe *vs.* Mn intensity. **c.** Fe *vs.* V intensity. The vertical lines separate the crystal's different blue color zones, which are defined by Fe intensity variations.

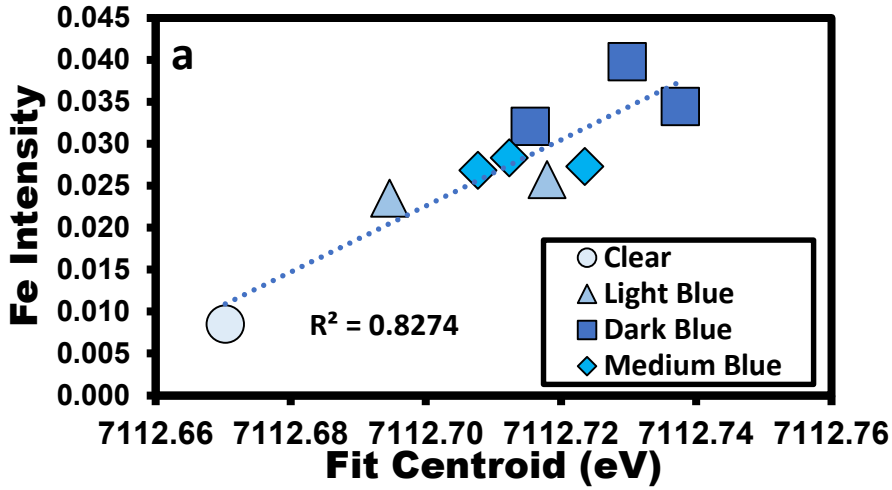

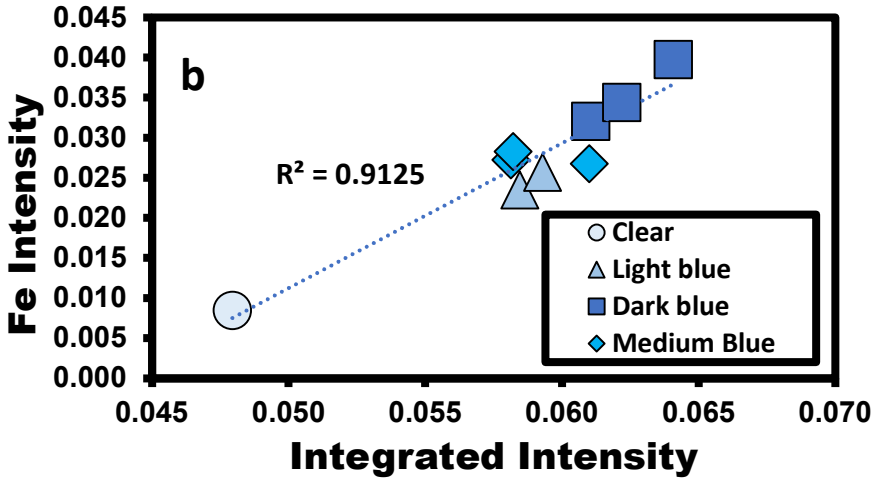

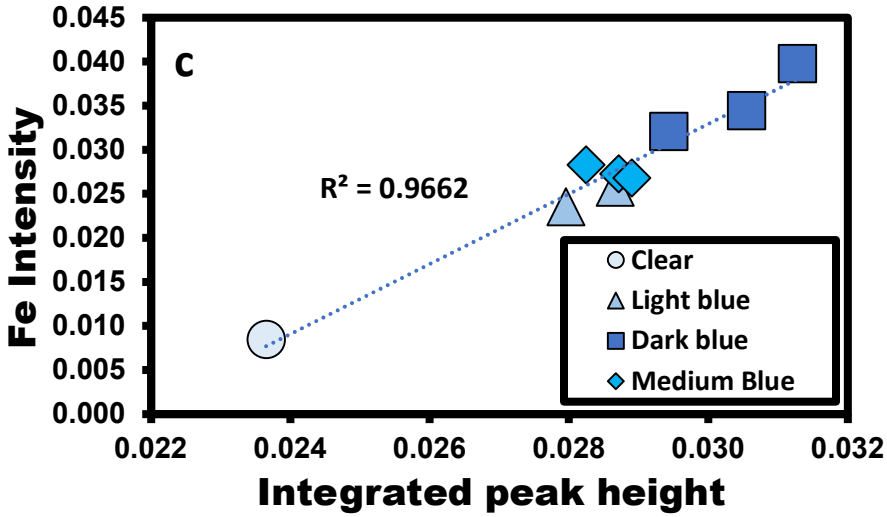

Figure 9. Binary plots of pre-edge fit parameters *vs.* Fe intensity. **a.** Fit Centroid *vs.* Fe Intensity. **b.** Pre-edge integrated intensity *vs.* Fe intensity. **c.** Integrated peak height *vs.* Fe intensity. Pre-edge peak parameters obtained by fitting all spots together. Energy unshifted to that of Wilke et al. (2001).

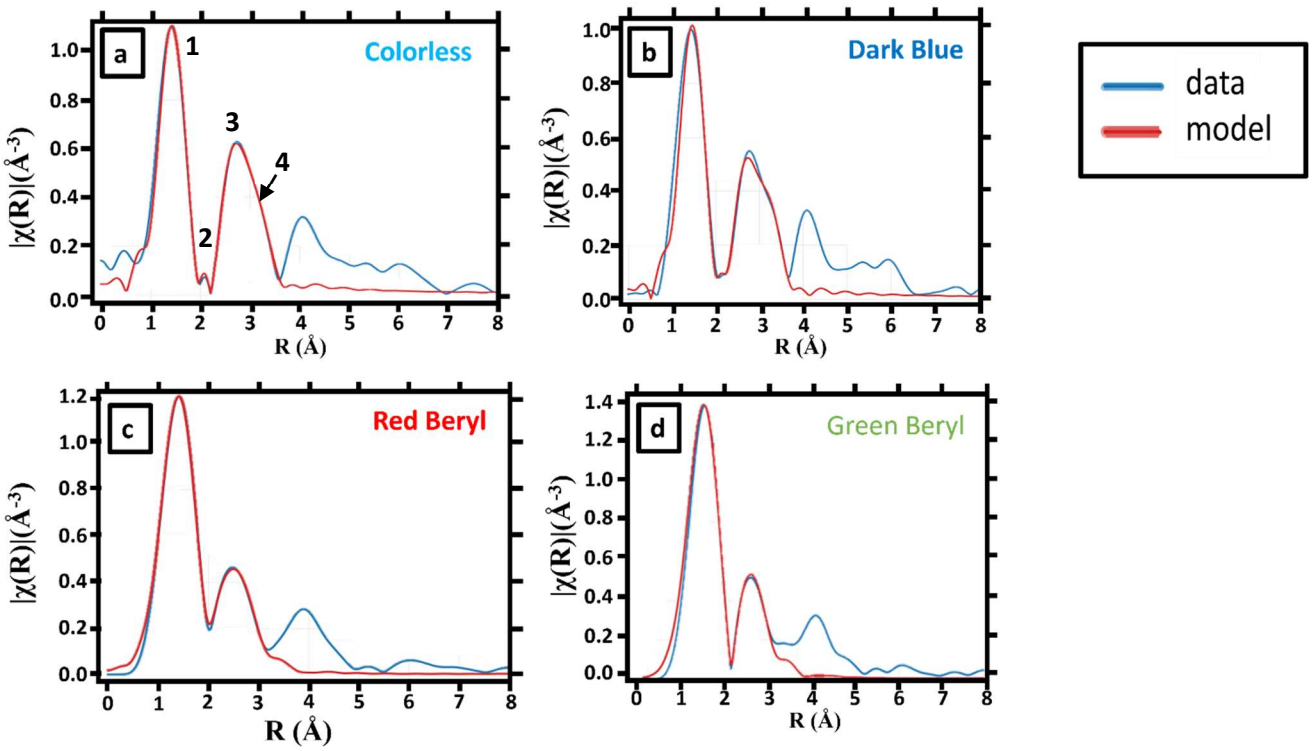

Figure 10. Representative FEFF fitting for Fe K-edge in R-space (Å) *vs.* the Fourier transform of the XAFS equation, $|\chi(R)|\left(\text{Å}^{-3}\right)$ for: **a.** Light blue/colorless zone in the zoned aquamarine crystal. **b.** Dark blue zone in the zoned aquamarine crystal. **c.** Red beryl crystal from the Wah Wah Mountains, Utah, sample 131716. **d.** Green zone of a zoned emerald crystal from Colombia, sample 97019.2. Numbers on the graph refer to peak numbers discussed in the text and reported in Table 2. Crystals from the Geological and Mineralogical Museum, Harvard University.

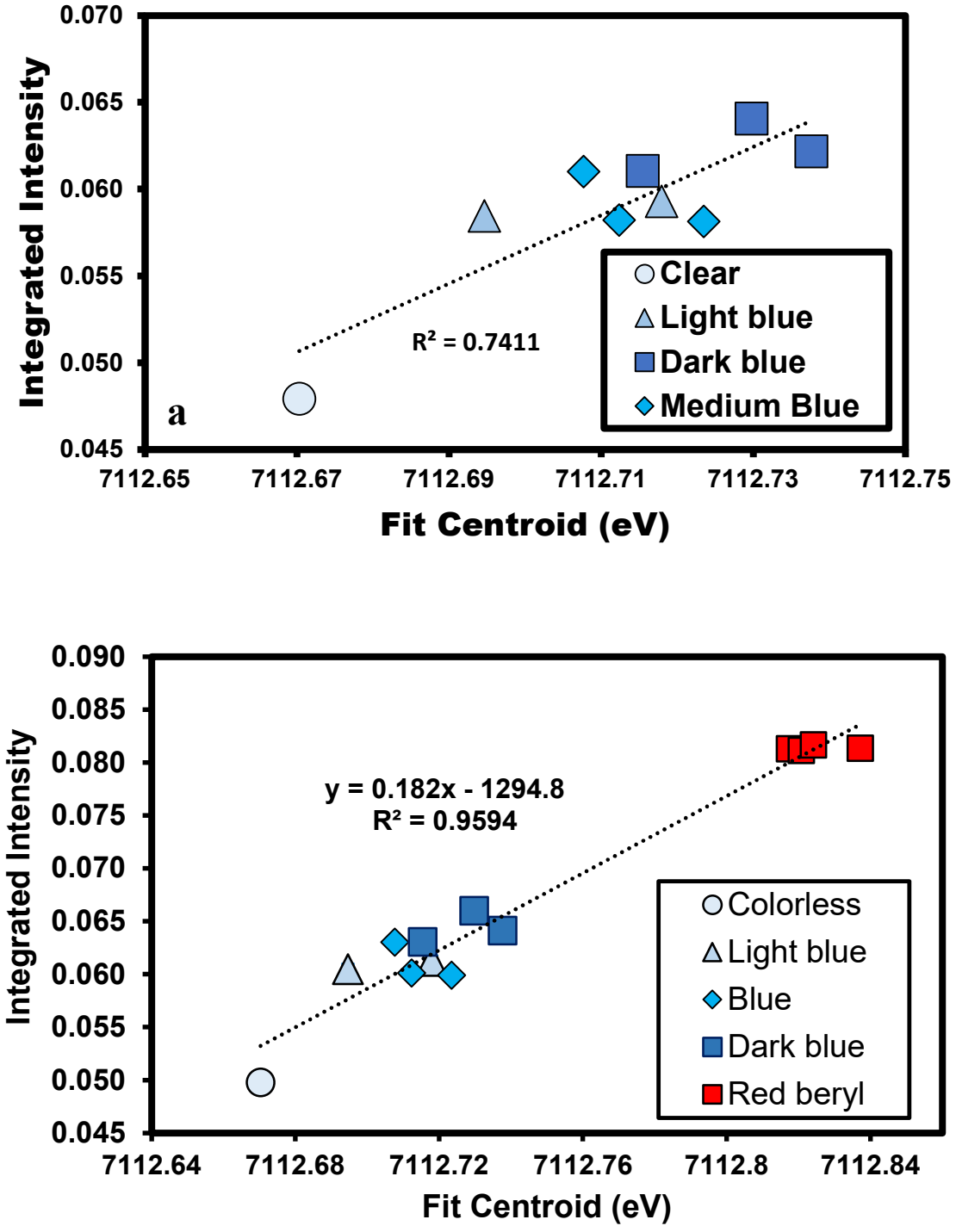

Figure 11. Pre-edge fit centroid (eV) position *vs.* integrated intensity for: a. Different color zones of the zoned aquamarine crystal from Minas Gerais, Brazil. b. Different color zones of the zoned aquamarine crystal and the red beryl crystal from Wah Wah Mountains, Utah. After Wilke et al. (2001). Inset shows the same graph with the end members of Wilke et al. (2001; not re-calibrated based on $E_{0;}$ energies not directly comparable).

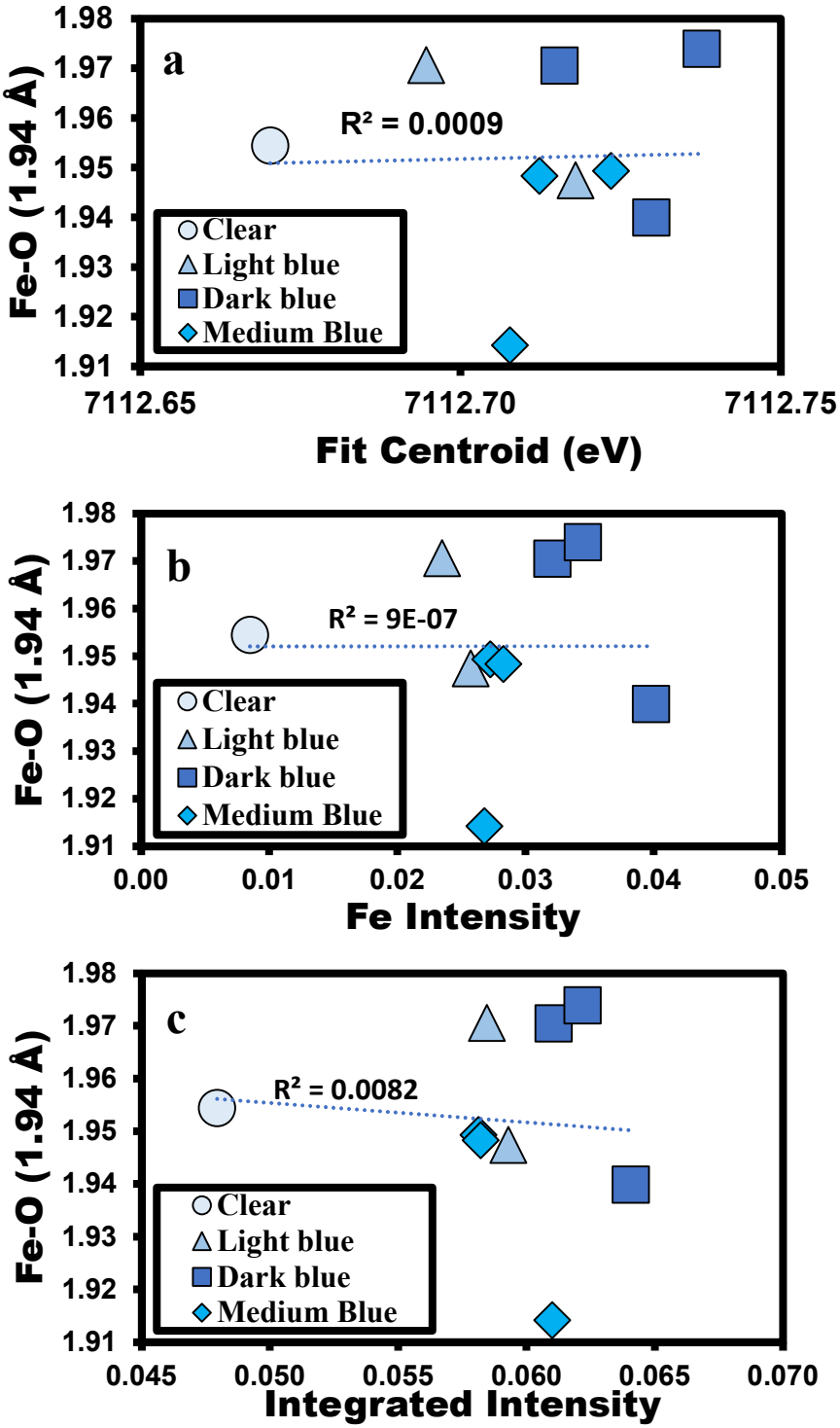

Figure 12. Graphs of modeled Fe-O bond distance (1.94 Å) obtained by FEFF EXAFS fitting for the zoned aquamarine crystal *vs.*: **a.** Fit centroid (eV). **b.** Fe intensity. **c.** Integrated intensity.

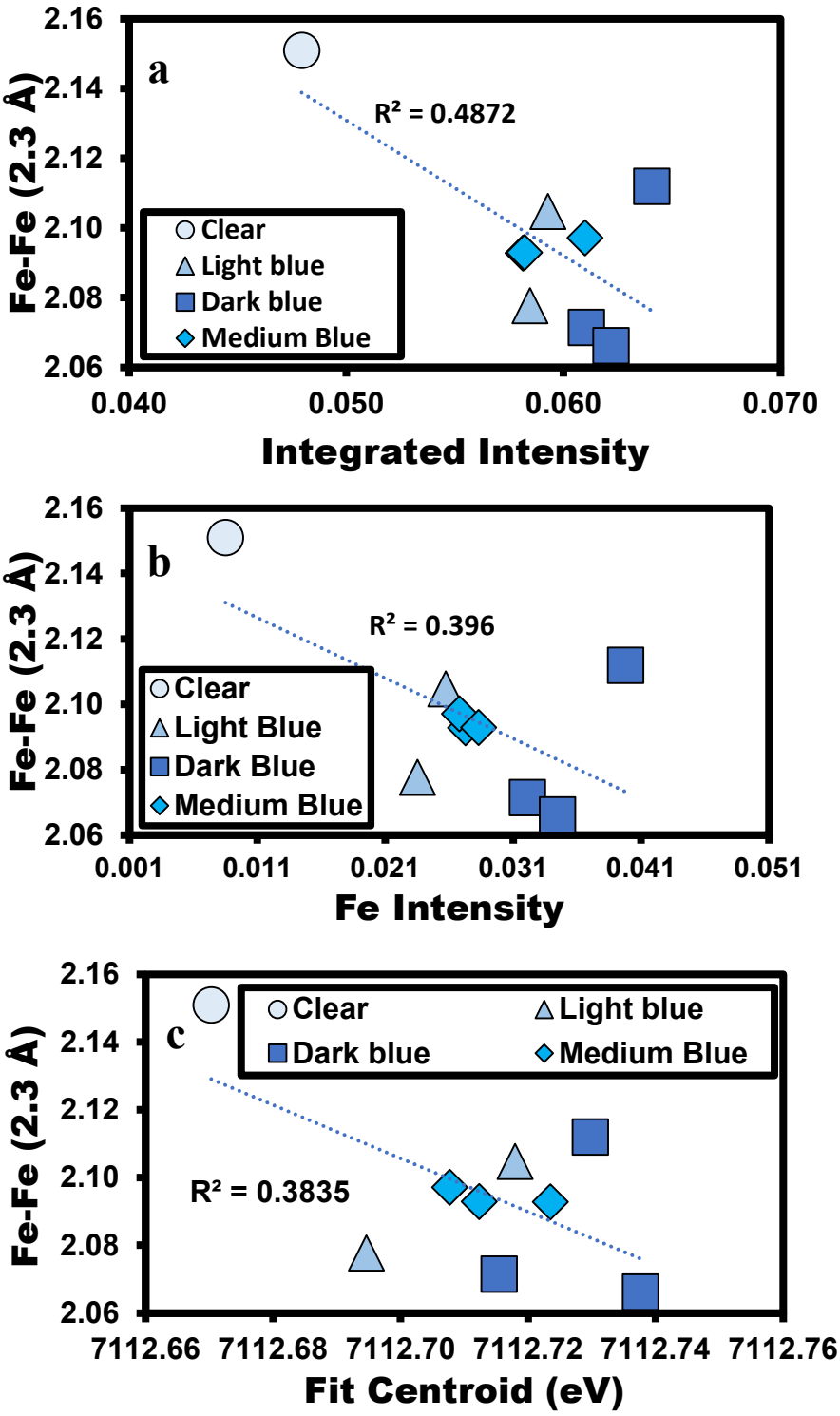

Figure 13. Graphs of modeled Fe-Fe bond distance (Å) obtained by EXAFS fitting for the zoned aquamarine crystal *vs.*: **a.** Integrated intensity. **b.** Fe intensity. **c.** Fit centroid (eV).

TABLES

Table 1. Pre-edge parameters for the Fe K-edge XAS fitting of different colors in the zoned aquamarine.*

Analysis I.D.	**Pre-Edge Parameter**							
Color	**P2 Center (eV)**	**P2 Amplitude**	**P2 Height**	**P1 Center (eV)**	**P1 Amplitude**	**P1 Height**	**Centroid (eV)**	**Integrated Intensity**
Spot 1 Colorless	7114.062	0.006212	0.00472	7112.463	0.041725	0.01892	7112.670	0.047937
Spot 2 Light blue	7114.101	0.007525	0.00538	7112.486	0.050931	0.02257	7112.695	0.058456
Spot 3	7114.114	0.007893	0.00550	7112.503	0.051398	0.02316	7112.718	0.059291
Spot 5 Dark blue	7114.088	0.008735	0.00582	7112.486	0.052316	0.02361	7112.715	0.061052
Spot 6	7114.071	0.009953	0.00622	7112.483	0.052230	0.02431	7112.738	0.062184
Spot 7	7114.100	0.009723	0.00636	7112.484	0.054339	0.02490	7112.730	0.064063
Spot 8 Medium blue	7114.057	0.008839	0.00571	7112.484	0.049295	0.02299	7112.724	0.058134
Spot 9	7114.078	0.008714	0.00571	7112.479	0.052287	0.02318	7112.708	0.061002
Spot 10	7114.097	0.008179	0.00539	7112.485	0.050032	0.02285	7112.712	0.058212

***** P1 and P2 denote the pre-edge peaks located at lower and higher energy, respectively. Data fitted by itself, unsmoothed, and unshifted.

Table 2. Parameters obtained from EXAFS FEFF fitting for the zoned aquamarine crystal.*

Peak	**Path #**	**Bond**	**R (Å) model**	**R (Å) fitting**	**Average (Å)**	**Residual**	**σ^2**
Peak 1	1	Fe-O	1.9416	1.9142-1.9740	1.9521	3.4119-4.4273	0.0045-0.0127
Peak 2	2	Fe-Fe	2.3000	2.0663-2.1510	2.0962	1.1373-1.4758	0.0072-0.0242
Peak 3	3	Fe-Si	3.2979	3.2938-3.3529	3.3316	3.4119-4.4273	$2.2\text{x}10^{-9}$-0.0032
Peak 4	4	Fe-O	3.7865	3.0206-4.5160	4.0379	N/A	0.0069-0.9899

***** Model Fe-Fe (Å) values used are Groat et al. (2010) values for Al-6g bond length. C.N. = Coordination number. σ^2 is the mean-square disorder.

Table 3. Summary of bond distances (Å) involving Fe^{2+} and Fe^{3+} in beryl in various crystallographic sites and coordination geometries taken from the literature.*

Tetrahedral coordination				Octahedral coordination					
Fe^{2+}-O	**Fe^{3+}-O**	**Be^{2+}-O**	**Al-6g**	**Fe^{2+}-O**	**Fe^{3+}-O**	**$^{Al}Fe^{2+}$-$^{6g}Fe^{3+}$**	**Al-Al**	**Al-O**	**References**
1.968	^{Be}**1.870**	1.635		^{Al}2.154	^{Al}2.016	N/A		1.904	Bačík & Fridrichová 2019
	^{Be}**1.891**				^{6g}2.16	2.49-2.51			Lin et al. 2013
				^{Al}2.154				1.955	Groat et al. 2006
					2.005		4.6		Edgar & Hutton 1982
	^{Be}**1.891**	1.6514	2.3		^{6g}2.16 ^{Al}1.94		4.6	1.955	Groat et al. 2010
		1.653				**2.55-2.76**		1.904	Andersson 2006
		1.73						1.94	Bragg & West 1926
					1.91		4.6		Loeffler & Burns 1976
								1.90	Gibbs et al. 1968

* **Bold** font numbers are distances discussed in the text relevant to the aquamarine crystal.

APPENDIX FIGURES

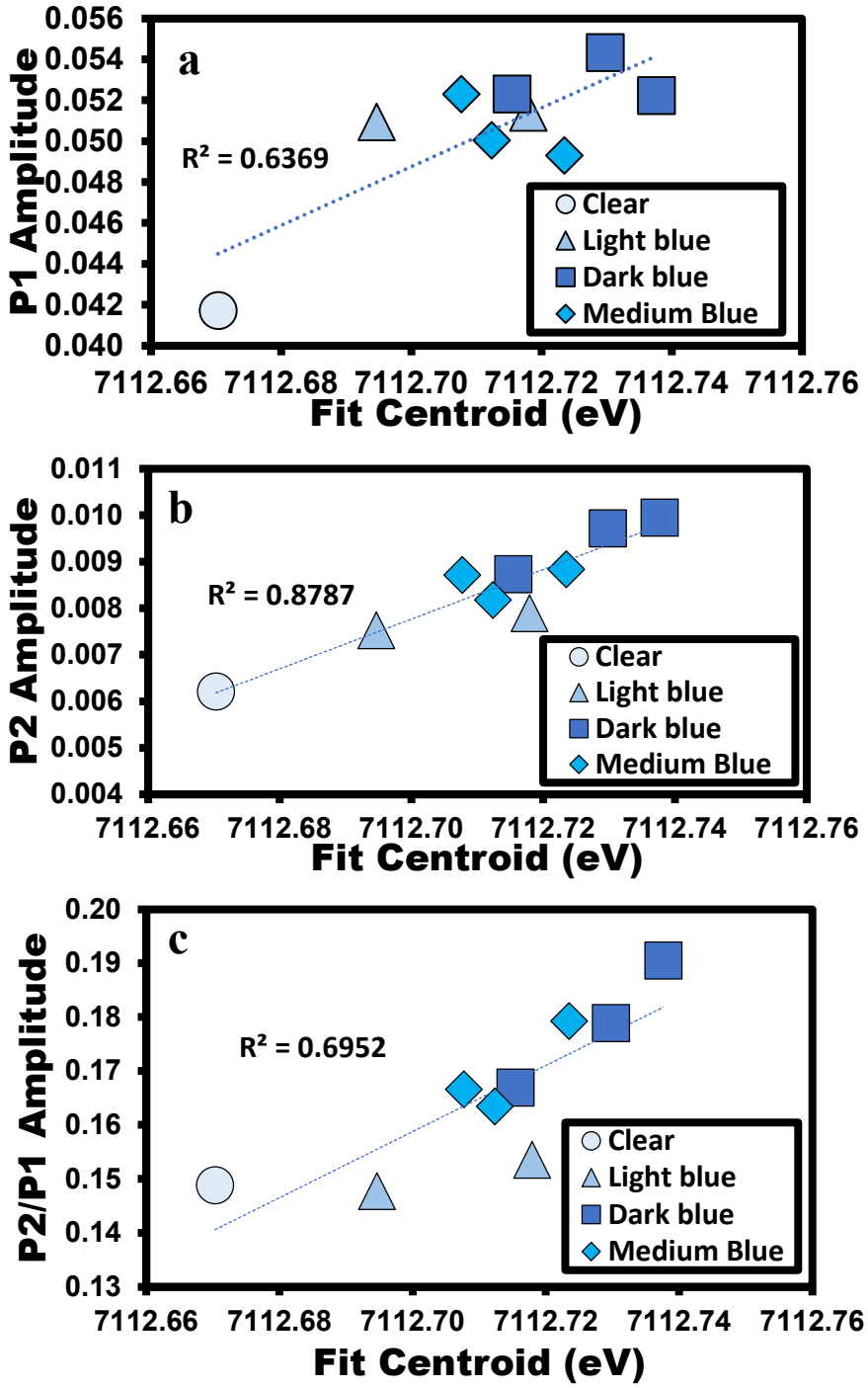

Figure A1. Binary plots of unsmoothed pre-edge fit centroid (eV) *vs.* pre-edge parameters for the zoned aquamarine crystal, sample 86394, Minas Gerais, Brazil. **a.** Fit Centroid *vs.* P1 Amplitude. **b.** Fit Centroid *vs.* P2 Amplitude. **c.** Fit Centroid *vs.* P2/P1 Amplitude. Pre-edge peak parameters were obtained by fitting all spots together.

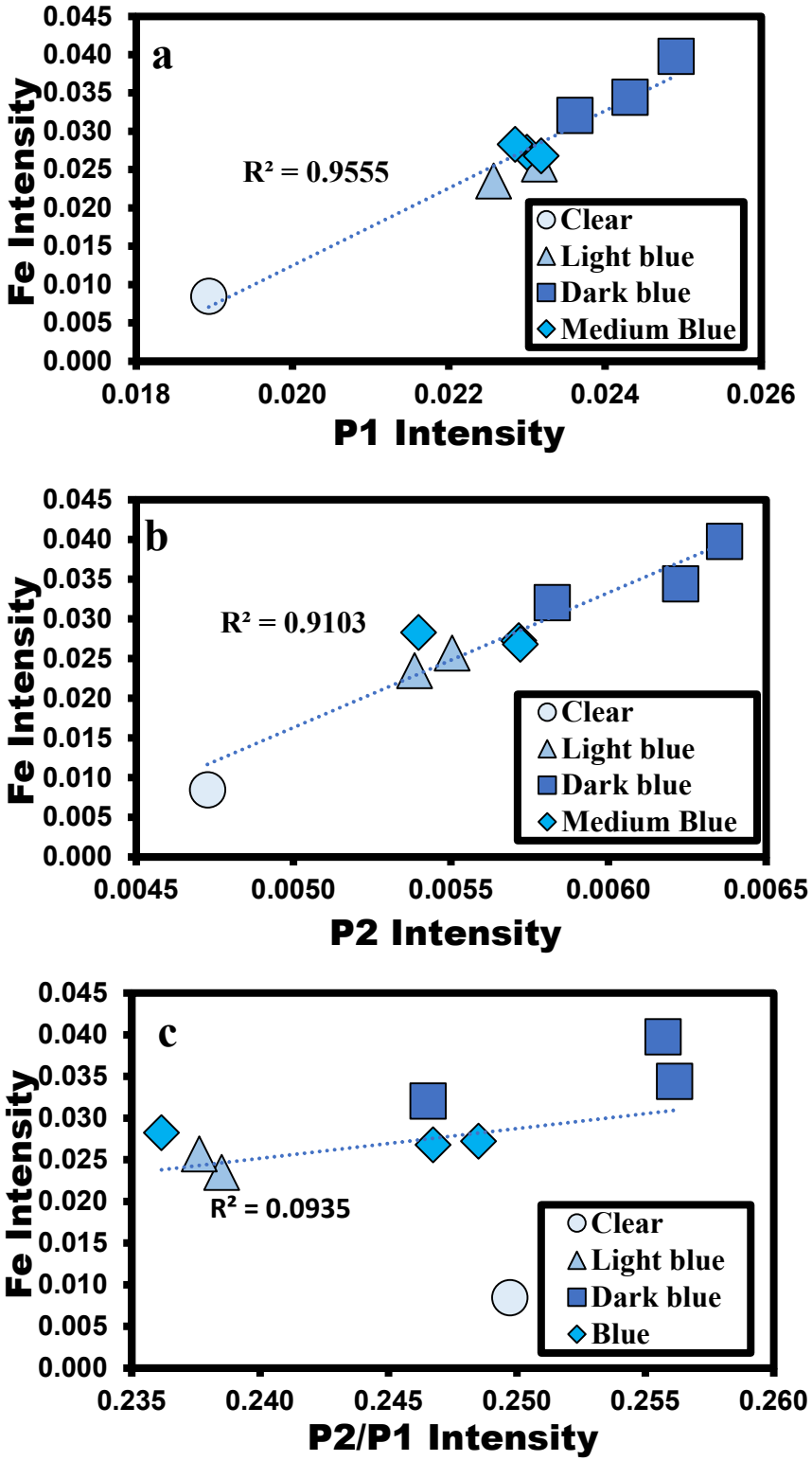

Figure A2. Binary plots of XRF Fe intensity *vs.* pre-edge parameters for the zoned aquamarine crystal. **a.** P1 intensity *vs.* Fe intensity. **b.** P2 intensity *vs.* Fe intensity. **c.** P2/P1 intensity ratio *vs.* Fe intensity. Pre-edge peak parameters were obtained by fitting all spots together.

APPENDIX TABLES

Table A1. Results of FEFF EXAFS modeling for the zoned aquamarine crystal.

Analysis ID	Color	Fe-O (1.94 Å)	Fe-Fe (2.30 Å)	Fe-Si (3.30 Å)	Fe-O (3.77 Å)
Spot 1	Colorless	1.9545	2.1510	3.3436	4.0072
Spot 2	Light Blue	1.9706	2.0777	3.3511	3.9877
Spot 3		1.9474	2.1047	3.3269	4.5158
Spot 5	Darker Blue	1.9706	2.0715	3.3480	3.9794
Spot 6		1.9740	2.0663	3.3526	3.9807
Spot 7		1.9400	2.1120	3.3217	3.9973
Spot 8	Medium Blue	1.9493	2.0928	3.3218	3.9996
Spot 9		1.9142	2.0971	3.2933	3.9186
Spot 10		1.9483	2.0929	3.3253	3.9544
Average (Å)		1.952	2.096	3.332	4.038
Minimum (Å)		1.914	2.066	3.293	3.919
Maximum (Å)		1.974	2.151	3.353	4.516

Table A2. Results of Fe K-edge pre-edge fitting for the red beryl crystal.

Analysis ID	Centroid (eV)	Integrated intensity
131716 spot 1	7112.81749	0.08129
131716 spot 2	7112.82075	0.08115
131716 spot 3	7112.83723	0.08134
131716 spot 4	7112.82417	0.08167
Minimum	7112.81749	
Maximum	7112.83723	
Average	7112.82491	

Table A3. Mechanisms attributed to variations in the blue color of beryl taken from the literature.

Finding	**Reference**
Pale blue aquamarine - $^{VI}Fe^{2+}$, $^{CH}Fe^{2+}$ More intense blue beryl - $^{VI}Fe^{2+}/^{6g}Fe^{3+}$ IVCT	Goldman et al. 1978
Blue beryl color - $^{Al}Fe^{2+}$, enhanced by $^{Al}Fe^{2+}/^{6g}Fe^{3+}$ IVCT Light blue beryl - $^{Al}Fe^{2+}$, darker blue - $^{Al}Fe^{2+}/^{6g}Fe^{3+}$ IVCT	Taran et al. 2017, Taran & Vyshnevskyi 2019 (summarize prior studies)
Less intense, common blue – spin-allowed d-d $^{VI}Fe^{2+}$ transition Dark blue – Fe^{2+}-Fe^{3+} IVCT and d-d $^{VI}Fe^{2+}$	Taran et al. 2018
$^{VI}Fe^{2+}$, $^{IV}Fe^{2+}$	Price et al. 1976
Light blue beryl - $^{VI}Fe^{2+}$ - $^{VI}Fe^{3+}$ (3 to 5 ratio), O^{2-} —> Fe^{3+} CT	Spinolo et al. 2007
Deep blue beryl - $^{Al}Fe^{2+}/^{VI}Fe^{3+}$ IVCT	Parkin et al. 1977
Colorless to medium to dark blue - higher absorption of $^{Al}Fe^{2+}$ or $^{Al}Fe^{2+}/^{6g}Fe^{3+}$ Fe pairs and higher Fe contents	Hu & Lu 2020
Light blue beryl – Fe^{3+}/Fe^{2+} IVCT Al-6g	Lin et al. 2013
Light blue beryl – mention Fe pairs, no discussion	Loeffler & Burns 1976

FIGURE CAPTIONS

Figure 1. Atomic structure of beryl: (a) looking down the c axis of the basal plane and showing the 6-membered silicate rings forming channels. (b) looking down the b axis illustrating the 6g interstitial position between two octahedral Al sites along the c axis. Be (green) and Si (light tan) are shown in their tetrahedral site, and Al in its octahedral (brown) coordination. Water (W) molecules (blue) and Na (purple) are shown in the channels.

Figure 2. Zoned aquamarine crystal used for the synchrotron-based Fe K-edge XAS and XRF study showing color zoning from right to left from clear to light blue, darker blue, and medium blue. Sample 86394, Minas Gerais, Brazil, Geological and Mineralogical Museum, Harvard University.

Figure 3. Sample stage setup with crystals oriented horizontally with their c axis at 45° to the direction of the incident X-ray beam. Advanced Photon Source synchrotron facility, Argonne National Lab, IL, where micro-XAS and XRF experiments were conducted.

Figure 4. Graph of normalized μ(E) *vs.* Energy (eV) with background subtracted for the nine XAS analyses of the zoned aquamarine crystal showing: a. The full energy range of the raw data spectra with analyses offset for visualization. b. Zoomed in view of the pre-edge area of the normalized spectrum.

Figure 5. Graph of normalized dμ(E)/dE *vs.* Energy (eV) for the Fe XAS analyses of the zoned aquamarine crystal showing the derivative spectrum of the XANES area at an energy range of 30 eV below the edge (E_0) and 30 eV above the edge.

Figure 6. Graphs of normalized μ(E) with baseline subtracted *vs.* Energy (eV) for Fe K-edge XAS pre-edge analyses of the zoned aquamarine crystal deconvoluted by two Voigt components.

Figure 7. Results of synchrotron micro-XRF spectroscopy of the zoned aquamarine crystal showing: a. Fe chemical map. b. X-slice of the Fe intensity (counts). c. Zoned Aquamarine crystal d. Cr chemical map. e. V chemical map. f. Mn chemical map.

Figure 8. Binary plots showing the relationship between elemental intensities (counts) derived from micro-XRF chemical maps in the zoned aquamarine crystal. a. Fe *vs.* Cr intensity. b. Fe *vs.* Mn intensity. c. Fe *vs.* V intensity. The vertical lines separate the crystal's different blue color zones, which are defined by Fe intensity variations.

Figure 9. Binary plots of pre-edge fit parameters *vs.* Fe intensity. a. Fit Centroid *vs.* Fe Intensity. b. Pre-edge integrated intensity *vs.* Fe intensity. c. Integrated peak height *vs.* Fe intensity. Pre-edge peak parameters obtained by fitting all spots together. Energy unshifted to that of Wilke et al. (2001).

Figure 10. Representative FEFF fitting for Fe K-edge in R-space (Å) *vs.* $|\chi(R)|\left(\text{Å}^{-3}\right)$ for: a. Light blue/colorless zone in the zoned aquamarine crystal. b. Dark blue zone in the zoned aquamarine crystal. c. Red beryl crystal from Utah, sample 131716. d. Green zone of a zoned emerald crystal from Colombia, sample 97019.2.

Figure 11. Pre-edge fit centroid (eV) position *vs.* integrated intensity for: a. Different color zones of the zoned aquamarine crystal from Minas Gerais, Brazil. b. Different color zones of the zoned aquamarine crystal and the red beryl crystal from Wah Wah Mountains, Utah. After Wilke et al. (2001). Inset shows the same graph with the end members of Wilke et al. (2001).

Figure 12. Graphs of modeled Fe-O bond distance (Å) obtained by EXAFS fitting for the zoned crystal, Brazil. *vs.* **a**. Centroid. **b**. Fe intensity. **c**. Integrated intensity.

Figure 13. Graphs of modeled Fe-Fe bond distance (Å) obtained by EXAFS fitting for the zoned crystal, Brazil. **a**. Integrated intensity *vs.* Fe-Fe distance (Å). **b**. Fe intensity *vs.* Fe-Fe distance (Å). **c**. Fit centroid (eV) *vs.* Fe-Fe bond distance (Å).

TABLE HEADINGS

Table 1. Pre-edge parameters for the Fe K-edge XAS fitting of different colors in the zoned aquamarine.

Table 2. Parameters obtained from EXAFS FEFF fitting for the zoned aquamarine crystal.

Table 3. Summary of bond distances (Å) involving Fe^{2+} and Fe^{3+} in beryl in various crystallographic sites and coordination geometries taken from the literature.

APPENDIX FIGURE CAPTIONS

Figure A1. Binary plots of unsmoothed pre-edge fit centroid (eV) *vs.* pre-edge parameters for the zoned aquamarine crystal, sample 86394, Minas Gerais, Brazil. a. Fit Centroid *vs.* P1 Amplitude. b. Fit Centroid *vs.* P2 Amplitude. c. Fit Centroid *vs.* P2/P1 Amplitude. Pre-edge peak parameters were obtained by fitting all spots together.

Figure A2. Binary plots of XRF Fe intensity *vs.* pre-edge parameters for the zoned aquamarine crystal. a. P1 intensity *vs.* Fe intensity. b. P2 intensity *vs.* Fe intensity. c. P2/P1 intensity ratio *vs.* Fe intensity. Pre-edge peak parameters were obtained by fitting all spots together.

APPENDIX TABLE HEADINGS

Table A1. Results of FEFF EXAFS modeling for the zoned aquamarine crystal.

Table A2. Results of Fe K-edge pre-edge for the red beryl crystal.

Table A3. Mechanisms attributed to variations in the blue color of beryl taken from the literature.